universität wien

MAGISTERARBEIT

Titel der Magisterarbeit

„Integralfield Spectroscopy of Galaxies: A Study of Interacting Seyferts“

Verfasserin

Mag. art. Ulrike Kuchner, Bakk.

angestrebter akademischer Grad

Magister der Naturwissenschaften (Mag.rer.nat.)

Wien, 2011

Studienkennzahl lt. Studienblatt:	A 066 861
Studienrichtung lt. Studienblatt:	Magisterstudium Astronomie
Betreuerin / Betreuer:	Ao. Univ.-Prof. Dr. Werner Zeilinger

Contents

Kurzbeschreibung

Diese Arbeit beschäftigt sich mit den Aktivitäten der Seyfert Galaxien UGC 1935, welche mit LEDA 212995 in Wechselwirkung steht, sowie Mrk 607, welche Teil eines Galaxienpaares ist. Kinematische Studien von Absorptionslinien (z.B. Rupke et al., 2005) zeigen großräumige Gasflüsse in wechselwirkenden Galaxien. Das metallarme Gas der Außenbereiche wird in das Zentrum getrieben, wo das akkretierte Material letztendlich das schwarze Loch des aktiven Kerns füttert. Zusätzlich wird Material der Zentralregion in Strömen nach außen getrieben. Die Kombination dieser Prozesse bewirkt einen Abfall der Metallizitäten im Zentrum und ein negativer radialer Metallizitätsgradient kann gemessen werden. Modelle zeigen Metallizitätsgradienten in engen Galaxienpaaren die flacher verlaufen oder abfallen, verglichen mit isolierten Galaxien. Rupke et al. (2010b) demonstrierte in N-body/SPH numerischen Simulationen von Mergern gleicher Masse, dass eine geringere Häufigkeit an Metallen in Gas auftritt, gemessen im Zeitraum zwischen ersten und zweiten Perizentrum der Bewegung. Der radiale Metallizitätsgradient flacht nach dem ersten Vorbeiflug aufgrund der Vermischung des Gases, ab.
Die vorliegende Arbeit portraitiert die Seyfert Galaxie UGC 1935 und untersucht erstmalig Metallizietätsgradienten einer aktiven Galaxie. Die Ergebnisse wurden mit der Sy 2 Galaxie Mrk 607 verglichen, welche, obwohl Teil einer Gruppe, scheinbar noch nicht in Wechselwirkung steht.$[OIII]/H\beta$ Linienverhältnisse wurden als Metallizitätsindikatoren über einen zentralen Bereich von $27'' \times 27''$ der Galaxien gemessen um nach Akkretionshinweisen zu suchen. Dafür wurden hochaufgelöste Daten des VLT Integral Field Units VIMOS, durch ein blaues Grism aufgenommen, verwendet und mit VIPGI, dem VIMOS Interactive Pipeline Graphical Interface (Scodeggio et al., 2005), reduziert. Signaturen der Flüsse als mögliche Auswirkungen der Wechselwirkung sowie zentrale Ausflüsse wurden in UGC 1935 gefunden, waren allerdings mit vorliegendem Material nicht zu sehen in Mrk 607. Nach einer Einleitung zu aktiven Galaxien im Allgemeinen und Seyfert Galaxien im Speziellen, folgt ein Überblick über die Vorteile der Integralfeld Spektroskopie. Zuletzt wird ein detailliertes Portrait der Galaxie UGC 1935 gezeichnet, welches Signaturen der Akkretion aufzeigt, und mit Mrk 607 verglichen.

Abstract

This work aims to give a closer look into the properties of the Seyfert galaxy UGC 1935 which is in interaction with LEDA 212995, as well as Mrk 607 which is part of a galaxy group.

Kinematic studies using absorption lines (e.g. Rupke et al., 2005) show large scale gas flows in interacting galaxies. The metal-poor gas is carried from the outskirts of the galaxy towards the center where the accreted material ultimately fuels the black hole of the active galactic nucleus (AGN). Additionally, material from the central region is torqued out of the system in outflows. The combination of these processes cause the central metallicity to drop and a negative metallicity gradient towards the central regions can be measured. Models show metallicity gradients of close pairs that are significantly shallower or even drop compared to gradients of isolated galaxies. Rupke et al. (2010b) demonstrated in N-body/SPH numerical simulations of equal-mass mergers that an underabundance of metals in gas occurs between first and second pericenter of the merging process. The radial metallicity gradient flattens after first passage due to mixing of the gas.

This work portrays the Seyfert galaxy UGC 1935 and introduces the investigation of decreasing metallicity gradients towards the center of an active galaxy, as well as compares the results with the Sy 2 galaxy Mrk 607 which, though part of a group, does not yet seem to be in interaction. $[OIII]/H\beta$ line ratios were measured as metallicity indicators throughout the central $27'' \times 27''$ of the sample galaxies to look for accretion signatures. Here, VLT's VIMOS Integralfield Unit in high resolution blue grism was used to search for such features. The data was reduced using VIPGI, the Vimos Interactive Pipeline Graphical Interface (Scodeggio et al., 2005). Signatures for inflows as a possible result of the interaction as well as outflows that would enhance the negative slope in the gradient, were found in UGC 1935, however were not detected in Mrk 607 with the present data.

After an introduction to active galaxies and Seyfert galaxies in particular, an overview of the advantages of integralfield spectroscopy is given. Finally, a detailed portrait of the galaxy UGC 1935 is given with signatures for accretion listed, and compared to Mrk 607.

1 Introduction

1.1 Interacting Galaxies

It has long been known that galaxies undergo morphological and chemical changes within their lifetime due to interactions and mergers with other galaxies. For a number of years now it has been acknowledged that the internal evolution of a galaxy influences the surrounding material on a kiloparsec scale. Gas from one galaxy can be found in another, visible distructions and filaments, jets and rings are obvious evidences of an interaction, but morphological analysis alone is not enough. Spectroscopy and its possibilities to investigate the evolution and kinematics of a system in detail opened a wide horizon to the world of the astrophysicist. The term of interacting galaxies was only introduced in the 1980s; before that, galaxies that didn't fit the Hubble sequence were classified as peculiar. The first theoretical paper on the matter was published in 1941 by Erik Holmberg (Holmberg, 1941). Because dark matter had not been known yet, many substructures couldn't be explained. The beginning of systematically cataloging the sky with the Palomar Sky Survey and the likes, and a gradual improvement of photographic scanning of the sky made an analysis of the so called peculiar galaxies possible. Theoretical and numerical simulations improved the understanding of colliding and interacting "stellar systems".

The Russian astronomer Vorontsov-Velyaminov published a catalog of 355 interacting galaxies in 1959 (Vorontsov-Velyaminov, 1959) and found a connection to galaxy groups. Meanwhile, Halton Arp, a young astronomer working at the Mt. Palomar observatory on an atlas of peculiar galaxies (Arp, 1966), showed that groups of galaxies were linked physically, and their close proximity wasn't a mere projection effect. This was done by spectroscopy, a means to find pairs that is still the most reliable to this day, as well as number statistics and photometric redshifts. Nowadays the criteria for physical pairs is that they are close in radial velocity (<400km/s), measured through line emission. This way it is possible to eliminate pairs that are not gravitationally bound but just happen to be in the

same line of sight.
The Arp Atlas of Peculiar Galaxies of 1966 depicts a number of interacting galaxies that are morphologically linked or obviously undergoing kinematical changes like outflows, filaments and rings. Later that century the atlas was expanded to fulfill the same criteria for the southern hemisphere (Arp & Madore, 1975). Jörg Pfleiderer, assuming a three-body-problem in the beginning of the 1960s, introduced the mathematical know-how. For his calculations he used first computers on the market (Pfleiderer, 1963) to show the evolution of a point mass, with surrounding masses illustrating stars, and a disrupting mass. Soon after, the development of spiral arms is visible.
Paul Hickson is responsible for a catalogue of compact groups (Hickson et al., 1989); while the brothers Toomre published their paper on galactic bridges and tails (Toomre & Toomre, 1972), which is widely regarded as the standard paper on the matter. Nevertheless, the physical understanding was only realized later with the introduction of spectroscopy and the measurement of radial velocities.
Today, state of the art simulations with means of supercomputing can give detailed insight in past, present and future.
In a nutshell, material is interchanged, transported and modified during passages, mergers and collisions. Merging is the phenomenon where two or more galaxies pass one another, lose energy and therefore merge. This could also happen through a direct, though rare, collision. When a galaxy enters the gravitational field of another, tidal forces form tails and bridge that are visible in observations. A noticeably smaller galaxy can be swallowed completely by the dominating galaxy. Galaxies of equal mass on the other hand, are first deformed to finally melt into one big galaxy – similar to an elliptical one.
In our own Local Group the Milky Way and Andromeda Galaxy M31 are separated by 700 kpc; they will probably merge within the next 12 billion years. In this scenario they will lose thermal energy, orbital energy and therefore their trajectories will become tighter. Momentum will be lost due to outflows of gas and the objects will come closer.
Minor mergers show a mass ratio of $0.1 < m/M < 0.5$, whereas a major merger takes place between galaxies of the same mass. An accretion of a dwarf companion or less massive galaxies result in M51 type objects. To model these interactions, masses, kinematics and geometry as initial conditions need to be known.
Merging phenomena are responsible for sudden bursts of star formation in irregular and elliptical galaxies as well as in tidal tails and other structures. The amount

of neutral hydrogen is crucial for this process of local and globular star formation, as well as non-thermal nuclear activities in AGN. In reality, usually more than one process happens simultaneously: *in-* and *outflows* of material, *stripping*, where the environment interacts with the galaxy and strips some material away, *passages*, *collisions* and *fly-bys*, where material is exchanged, and – finally – *merging*. The surroundings and velocities influence the evolution extensively, where the rule of thumb says that mergers are more likely to take place in low density environments with lower velocities. Depending on the velocity dispersion, structures vary from narrow to broad, shells and ripples may form and HI gas is redistributed, as well as star formation observed. It is believed that in the local universe at least half of the galaxies have been subject to interactions or mergers with the result of kinematically separated components, nuclei of different rotation or velocity, starbursts, material flowing towards the center, or the evolution of bars. The Milky Way is accreting material through the Magellanic stream and infall of satellite galaxies. Bridges are fueled with dust and already processed gas from these galaxies.

Also in galaxies with an active nucleus, where the nucleus emits non-thermal radiation, one can see accretion processes which can be traced back to a black hole in the galaxys center that is responsible for the ionization mechanisms (e.g. Krolik, 1999). While material is transported towards the central supermassive black hole, its potential energy is transformed into kinetic energy. This is believed to fuel the activity of the nucleus.

The accretion of gas has two significant characteristics: star formation is being enhanced or a second star formation era is being initiated in elliptical galaxies. The emission of Hα is the best indicator for star formation with the hydrogen lines in general being used as star formation indicators. The star formation history of a galaxy can be inferred through equivalent widths of emission lines Hα, Hβ and the ratio [OIII]/Hβ (e.g. Lequeux et al., 1981; Copetti et al., 1986).

Often interactions are not apparent in optical observations, but can be studied in the radio range. Through dynamical analysis of neutral hydrogen in radio wavelengths, one can retrace the material. In other systems, like M 51, signatures of interactions are clearly visible in optical observations thanks to dust filaments. These parameters are substance of constant decrease through time and are therefore good star formation age indicators. Other equivalent widths and their ratios, like Hα and [NII] are used to measure starburst activities (Kennicutt & Kent, 1983) and other classifications (see later in the text).

Numerous questions still wait to be answered: What type of galaxy shows evidence for ongoing star formation (SF)? Is there a correlation between EW (Hα + [NII]) and luminosity $M_{\rm B}$? Does SF depend on the luminosity or the form of interaction (e.g. the separation of the pair)? Are AGN more frequent in interacting galaxies than in isolated ones? Is an AGN the mere consequence of an interaction where gas loses its angular momentum and is forced to fall into the inner, nuclear, regions where the black hole resides? High density gas in these regions are identified and strong star formation is detected in some active galaxies. Strong star formation regions could be the reason for a possible incorrect estimation of the number of AGNs like Seyfert galaxies in some studies, although one needs to bear in mind that when low spatial resolution is used for observations, the HII region spectra would dilute the AGN spectra (Sánchez et al., 2004).

1.2 Active Galactic Nuclei

1.2.1 Introduction

Generally speaking, the term Active Galactic Nucleus or AGN refers to the fact that some galaxies host a nucleus where in addition to the thermonuclear sources of the stars there is yet another energy source. These objects show – besides having HII regions and planetary nebulae – nebular emission lines in the spectra of their nuclei (Osterbrock & Ferland, 2006). When looking at a mere image of a number of galaxies, it is difficult to distinguish normal galaxies from "active"galaxies. Their difference can be seen in their spectral energy distribution (SED) though. Since the content of a regular galaxy is similar to our own Milky Way, the stars - and in spiral galaxies the gas and dust content (with the latter visible in the optical wavelength range only) also - will be similar. Active galaxies show additional emission lines in their spectra. In contrast to these AGN host galaxies the majority of galaxies emits light that stems from the galaxy's stars as well as - to a much lower degree - it's gas and dust. The SEDs of these normal galaxies show a summation of the spectra of all the associated stars - each with different absorption features, described as a Planck distribution. To a first approximation, the spectrum of a star can be compared to a blackbody, the idealized case of an opaque hot material (i.e. the thermally emitting matter needs to be optically thick to emit the blackbody spectrum). The only free parameter is the effective surface temperature of the body, meaning the wavelength of the peak intensity will vary with temperature. Depending on the temperature of the star the peak will be measured in different wavelength ranges. The sun peaks around 5800 Å in the optical whereas the hottest stars at 30000 K − 40000 K will peak in the deep UV and stars with only half the temperature of the sun can be best studied at ~ 1 micrometer. Since galaxies are comprised of stars of all temperatures, the galaxy's spectrum will be a superposition of them all. In addition to the continuous thermal spectrum, a star's spectrum normally shows absorption lines. The strength and width of the lines contains the information about the star's chemical composition, surface temperature and luminosity. Furthermore, radial velocities and possible binary conditions can be measured using Doppler shifts. In addition to the red-shift of the galaxy which affects all spectral lines, motions within the galaxy give rise to their own Doppler shifts resulting in broadening of both absorption as well as emission lines (due to the movement of the HII regions for example). Light that reaches the observer from the object is the sum of many photons emitted by a vast number of atoms, all of them moving and therefore each blue- or redshifted according to the motions and different speeds (Δv or σ, the velocity dispersion) of the atom as well as the observer. This results in the spreading of wavelengths or Doppler broadening of the spectral line:

$$\frac{\Delta\lambda}{\lambda} \approx \frac{\Delta v}{c}, \tag{1.2.1}$$

where c is the speed of light and λ is the central wavelength of the spectral line. The velocity dispersion, the movement of the atoms of mass m and temperature T is given as

$$\Delta v \approx \left(\frac{2kT}{m}\right)^{1/2}, \tag{1.2.2}$$

where k is the Boltzmann constant $1.38 \times 10^{-23}\,\mathrm{J\,K^{-1}}$. Doppler broadening can also arise due to bulk motion like rotation of a galaxy, inflow or outflow of gas like in an accretion disk, or turbulence in a cloud. The surface temperature of the stars also confines the Spectral Energy Distribution (SED) to certain wavelength ranges. The SED is used to describe the energy that is emitted at each point of the (broadband) spectrum as a function of wavelength. The broadband spectrum reveals the spectrum over all the observed wavelength ranges. AGNs show SEDs

with higher fluxes than usual galaxies which therefore cannot be explained by stellar radiation alone.
Emission lines can be found when hot stars ionize gas and the free electrons rejoin atoms in cascading recombination processes. They radiate at distinct wavelengths associated with jumps between possible energy levels. Emission lines can also be formed from collisions of loose electrons with heavy-element atoms as well as hard radiation fields like in AGN. Additionally, both permitted and forbidden lines can be found in active galaxies. Forbidden lines stem from regions of extremely low densities. Only in these environments atoms and ions are long enough in their excited states to spontaneously emit a photon whereas at higher densities they are more likely to de-excite due to collision with other particles. They are denoted by square brackets and are prominent in spectra of active galaxies. Indeed this work will focus on the forbidden line of [OIII]$\lambda 5007\,\text{Å}$. Active galaxies generally show broad, strong emission lines whereas the forbidden lines remain narrow. This tells us that the galaxy contains hot low-density gas and the broad lines imply rapid motions.
The emission line ratios help distinguish the various processes. The flux density, F, is measured in $\mathrm{W\,m^{-2}}$ and can be described as the power received per square meter of telescope collecting area. Hence the spectral flux density (the flux density measured in a small wavelength range) is expressed in $\mathrm{W\,m^{-2}\,\mu m^{-1}}$ or $\mathrm{W\,m^{-2}\,Hz^{-1}}$. When comparing widely separated parts of the spectrum, the quantity F_λ (or F_ν with $F_\lambda = \frac{c}{\lambda^2} F_\nu$) is usually normalized to λF_λ to adjust for the misleading fact that the flux density is defined as the flux received over a $1\,\mu m$ bandwidth and therefore one easily underestimates the energy in the far-IR while exaggerating the emitted energy in the X-ray (Jones & Lambourne, 2004). The strength of the emission lines is also related to star formation. In regions where there is ongoing star formation bright, hot HII regions can be seen. In his sense, the gas in the galaxy - usually spiral or irregular - is made visible. AGN exhibit additional emission lines not seen in star forming galaxies that can be ascribed to the high energy radiation and dense gas. The dust component of a galaxy absorbs some starlight, but is only emitted prominently in the spectrum at wavelengths of about 100μm and is therefore not relevant for work in the optical. For AGN it is necessary to consider the spectrum at all wavelengths and look at broadband spectra to understand the ongoings of the AGN fully. Very often the AGN outshines the host galaxy so that these galaxies were therefore originally classified as pointlike sources. These Quasi-Stellar Objects mark the most luminous objects

in our universe and can therefore be found at the highest redshifts of z=5, 6 or even 7.
Exactly what fuels the engine of these powerful active galaxies is still a mystery. In the end a source as small as the solar system has to produce 10^{11} times the power of the sun, if not more. The main proposition is, that the engine is indeed an accreting supermassive Black Hole where gravitational energy is transferred to electromagnetic radiation. When talking about sizes and luminosities of the AGN, one has to be careful. The variability of AGNs can be used to infer their size, and since the variability usually depends on the wavelength of observation, we could assume that the size of an AGN depends on the wavelength.This is true to the fact that different radiation stems from different parts of the object. X-rays, that usually show much faster radiation, come from smaller regions of the AGN than infrared emission with much slower variations. An object that fluctuates in brightness on a timescale Δt can have a radius no greater than $R \sim c\Delta t$ (Jones & Lambourne, 2004).
There is a number of subclasses of AGN or related objects like Radio Galaxies, BL Lac Objects, Seyfert Galaxies (Type I and II), Low Ionization Nuclear Emission-Line Regions (LINERs), Star Burst Galaxies, Quasistellar Objects (QSOs) and Quasi-stellar radio sources (quasars), the most luminous objects in the sky, and some more. All these objects together are called Active Galactic Nuclei. In general one can distinguish between type-I AGN which show broad, strong optical-UV emission lines, and type-II AGN that show prominent narrow emission lines and only faint broad lines or none at all as well as a large X-ray obscuring column(Netzer, 2006). The two largest subclasses seem to be Seyfert galaxies and quasars. It appears that most of the ionized gas in the nucleus is photoionized, not through O and B stars, but by the emission of the accretion disk around a Black Hole in the galaxy's center instead. Other options are that the gas is photoionized by relativistic particles and perhaps a magnetic field of the environment of the Supermassive Black Hole (SmBH). The much higher energies of the radiation of these objects can be easily seen in an AGN's spectrum in comparison to spectra of hot stars in ionized HII regions and planetary nebulae as well as particle and energy densities being much larger (Osterbrock & Ferland, 2006). The number of extragalactic emission line objects is large and the classification somewhat confusing and depending on schemes and selection criteria which are often morphology based rather than on their emission line ratios. Active galaxies come in different flavors and varieties. They were discovered independently and

all show some peculiarity in their spectra. The names of subclasses often point to their discoveries and in the following a historical overview will discuss this briefly.

1.2.2 Historical overview

Edward A. Fath at Lick Observatory was the first to notice six emission lines in the spectrum of the central region of NGC 1068 in 1908. They were measured to be of well known wavelengths Hβ λ4861 Å, [OII] λ3727 Å, [NIII] λ3869 Å, and [OIII] λ λ4363, 4959, 5007 Å. Five years later V. M. Slipher photographed the spectrum of NGC 1068 with "an exposure of 6 and one-half hours. Because of the interesting nature of this plate a second one was made [...] with about double the exposure [...]"(Slipher, 1917). The observational techniques improved over the decades until finally Carl Seyfert published his important paper of galaxies with nuclei with broad emission lines arising from a small nuclear region, describing the now known classification of Seyfert galaxies in 1943. He and other before him found that this phenomenon is not limited to a few special cases but instead he found a whole subclass of mainly spiral galaxies exhibiting broad lines like Hydrogen-Balmer lines due to recombinding hydrogen. In his paper Seyfert discusses the high central surface brightness of the point-like sources outshining the host galaxies observing that "the nuclei have high luminosity which on direct photographs are scarcely distinguishable from stars"(Seyfert, 1943). The fast development of radio astronomy led to identifications of strong radio sources that are similar to spectra of Seyfert galaxies. The study of the Third Cambridge Radio Catalogue 3C (Edge et al., 1959) and it's revision, the 3 CR (Bennett, 1962) allowed a cross-reference to another wavelength and the term *Radio Galaxy* was formed. With the advance of large surveys in different wavelengths like the Sloan Digital Sky Survey (SDSS) (York et al., 2000) , the 2dF Galaxy Redshift Survey (Colless et al., 2001) or later the VIMOS VLT Deep Survey (VVDS) (Le Fèvre et al., 2005), new objects and subclasses were found.

Most *Quasi Stellar Radio Sources* or *quasars* (a new category labeled shortly after (Matthews & Sandage, 1963)) - if not all - are now understood to be AGNs, luminous and so distant that the host galaxy could not be detected by photographic means. But upon discovery they were misunderstood as being stellar, which gives them their misleading name. Now quasars and QSOs (*Quasi-Stellar Objects*) are detected to distances of z$\geq$6 which makes them the most distant objects in the universe know today. Some of these Quasi-Stellar Objects could be observed in the optical and UV, but then didn't show radio emissions, therefore also named *radio quiet quasars* (RQQs) in comparison to the now called *radio loud quasars* (RLQ). Even within these groupings there are subgroupings depending on features like jets or lobes, their extension or compactness. Even though the names have been kept the same, it is now known that these QSOs are not stellar but rather very luminous AGN outshining their host galaxies just like Seyfert Galaxies. A quasar, though, can be 100 times brighter than the host galaxy whereas a Seyfert galaxy is usually said to be less luminous, holding the same optical luminosity as its host. A number of other object classes were denominated, sometimes after the first object found with the specific properties, sometimes just summarizing their distinct features. Only some of them shall be named here and summarized in the next section.

1.2.3 Classification of AGN

Seyfert Galaxies

After Fath's discovery of emission lines in NGC 1068, V.M. Slipher at Lowell Observatory found these to be similar to planetary nebulae lines and measured their widths of hundreds of kilometers per second. Seyfert later published his findings that there is a number of galaxies dominated by high-excitation nuclear emission lines. The main characteristics can be summarized to be:

1. The lines are broad (up to $8500\,\mathrm{km\,s^{-1}}$, full width at zero intensity),

2. The hydrogen lines sometimes are broader than the other lines

(Peterson, 1997). B. E. Markarian and his collaborators at Byurakan Observatory found more and more of these objects during surveys using Schmidt cameras and obtaining slit spectra (Osterbrock & Ferland, 2006). First attempts to understanding the physics of Seyfert galaxies were carried out by Woltjer in 1959 (here taken from Peterson (1997)) where he stated:

1. The nuclei are unresolved, with the size of the central object not exceeding 100 pc.

2. The nuclear emission must last more than 10^8 years, because Seyfert galaxies constitute about 1 in 100 spiral galaxies with the assumption that either all galaxies pass through a Seyfert phase with one in 100 galaxies currently

being in the phase, or the other scenario being that galaxies which are Seyferts are always Seyferts in which case their lifetime is the age of the universe.

3. If the material in the nucleus is gravitationally bound, the mass of the nucleus must be very high. With the assumption of the virial argument $M \approx v^2 r/G$ and measurements of line widths of the order of 10^3 km s^{-1} as well as the upper limit of the nucleus of r $\leq$ 100 pc in a low-density gas, the mass of the nucleus can be inferred to be in the range $M \approx \pm 10^{9\pm1} M_\odot$.

This also means that about 10 % of the mass of the galaxy is contained in the comparatively small centeral region of the Seyfert galaxy, an area of about only 100 pc across. The total energy emitted by the active nucleus of the Seyfert galaxy measures about $10^{11} L_\odot$, approximately the same as the host galaxy. Seyfert galaxies often show an excess in the far infrared as well as other wavelengths. At some wavelengths though, also in the optical, this radiation is variable, another reason to believe that the emitting region is tiny compared to the galaxy itself.

It is believed that a typical Seyfert galaxy comprises a broad line region (BLR) in the galaxy's very center surrounded by a dusty torus, with the BLR only measuring a volume of about 10 pc across; then a narrow line region (NLR) of about 100 pc with the extended narrow line region (ENLR) following out to about 1 kpc. Jets and radiation may be seen coming from the broad line region (see figure 1.1). The line spectra of Seyfert galaxies can further be divided into two subsections depending on the width of their strong emission lines. This schematic was first proposed by E. Khachikian and D. W. Weedman in 1974 (Khachikian & Weedman, 1974). The spectra can be interpreted in terms of density - depending on whether forbidden lines can be detected - and motion of gas clouds - inferred from line widths. In this way, the BLR is comprised of dense fast-moving clouds and the NLR of low-density, more slowly moving clouds (Jones & Lambourne, 2004) which is consistent with the speeds assumed for matter in spherical orbits around the gravitational center.
As seen in figure 1.1, the clouds of the broad line region can be found in the central opening of the dusty torus with a radius of about 10^{14}m. The radiation of the central engine heats the gas to high temperatures of about 10^4 K which also vaporizes the dust grains of the clouds, only making up about 10 $M_\odot$. The narrow line region is believed to lie much further out with lower orbital speeds of about $200 - 900$ km s^{-1}. An extended narrow line region (ENLR) can be found to up to several kiloparsecs from the AGN and is comprised of interstellar gas ionized by

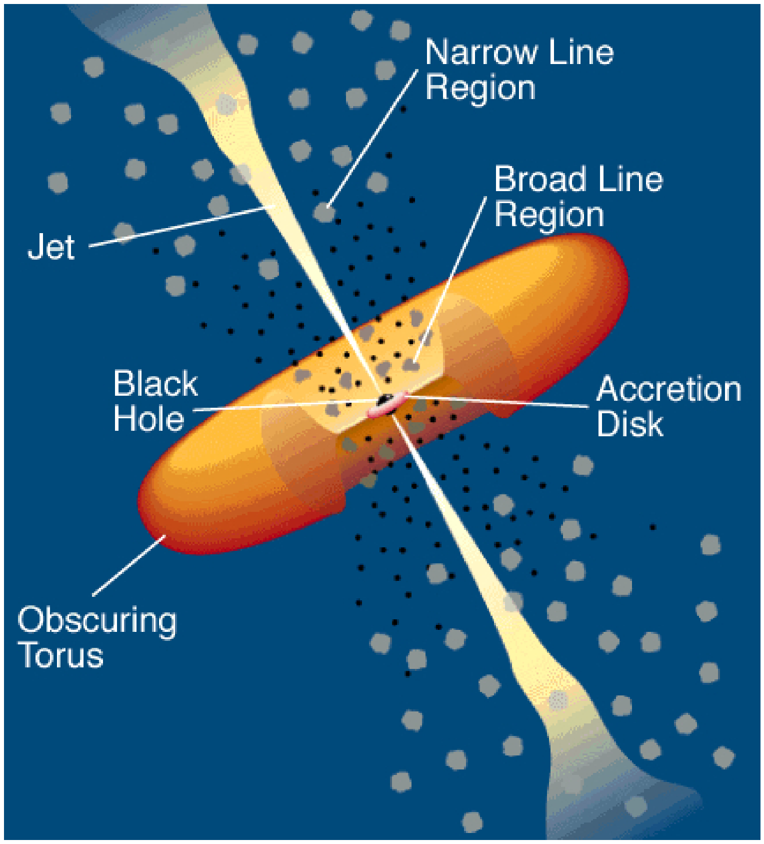

Figure 1.1: Schematic view of an AGN as seen today. Credit: C.M Urry and P. Padovani

the radiation from the engine. Because this area is situated outside the obscuring torus, the NLR can be observed at all times with the BLR sometimes hidden. This is believed to be responsible for the difference in type 1 and type 2 AGNs. Seyfert 1 galaxies have two sets of emission lines superimposed on one another, one being characteristic of a low-density environment (with electron density $n_e \approx 10^3 - 10^6\,\mathrm{cm}^{-3}$) of ionized gas with (somewhat narrow) widths corresponding to velocities of several hundred kilometers per second (Peterson, 1997) of mainly the forbidden lines. In addition, the spectra show very broad HI, HeI and HeII emission lines, with full-widths at half-maximum (FWHM) of the order of $1-5\times 10^3\,\mathrm{km\,s}^{-1}$ and more, while the forbidden lines [OIII] $\lambda\lambda$ 4959, 5007 Å, [NII] $\lambda\lambda$ 6548, 6583 Å, [SII]$\lambda\lambda$ 6716,6731 Å typically have FWHMs of $5\times 10^2\,\mathrm{km\,s}^{-1}$, thus being much narrower, even though still broader than in most starburst galaxies which host many HII regions illuminated by hot, young stars and therefore prominent emission lines can be observed as well as a peak in the IR of their spectral energy distribution coming from the heated dust. The forbidden lines are sensitive to the gas density in the emitted region(Jones & Lambourne, 2004). It seems the reason for the lack of observed broad forbidden lines means that they originate from a denser region ($n_e \approx 10^9\,\mathrm{cm}^{-3}$ or higher). A good example of a Seyfert I spectrum is the well-studied galaxy NGC 5548 (see figure 1.2).

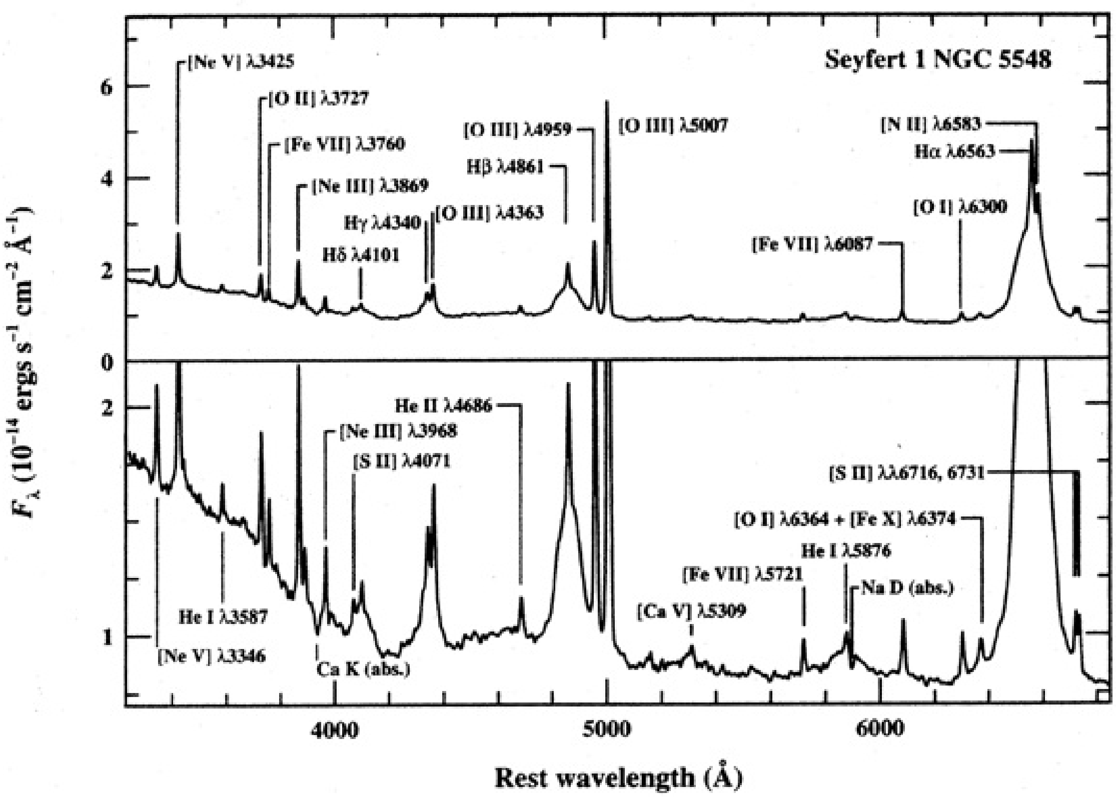

Figure 1.2: Spectrum of NGC 5548, z=0.017. The prominent narrow and broad lines are labeled. The spectrum is the mean of several observations with the Faint Object Spectrograph on the Hubble Space Telescope in 1993. Data courtesy of K. T. Korista.

Seyfert 2 galaxies solely show narrow lines which means, they have permitted and forbidden lines with approximately the same FWHM of $500\,\mathrm{km\,s^{-1}}$. The difference can be seen comparing the spectrum of NGC 5548 with that of the Seyfert 2 galaxy NGC 1667 (see figure 1.3).

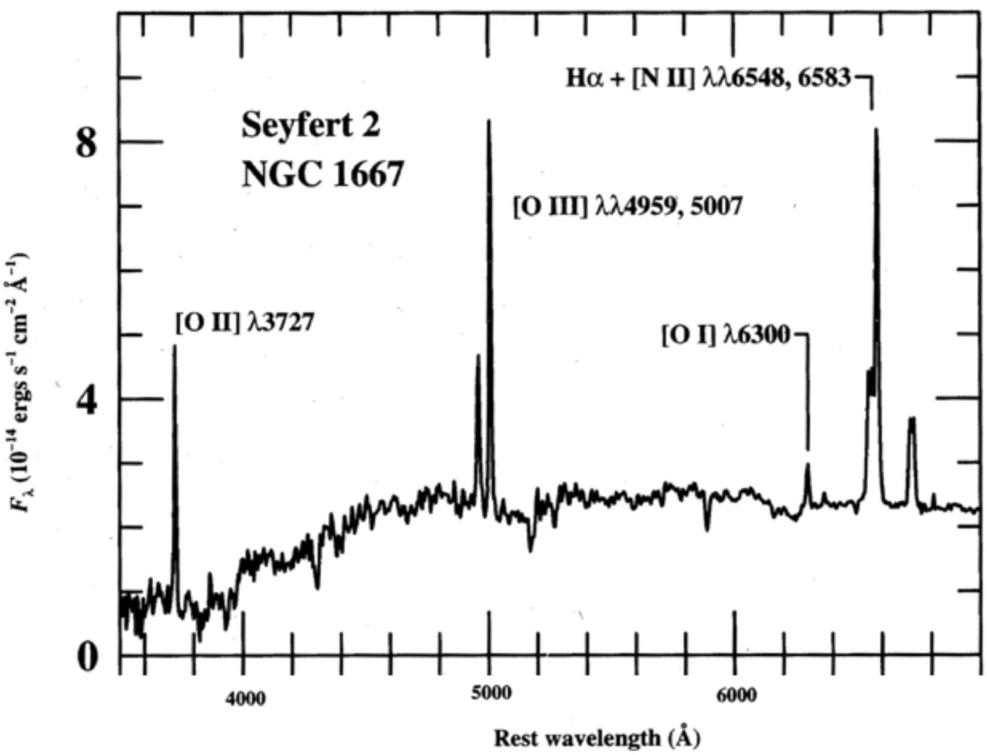

Figure 1.3: Optical spectrum of NGC 1667 with important emission lines identified (Ho et al., 1993). The absorption lines arise in the host galaxy rather than the AGN. Data courtesy of A. V. Filippenko.

Some galaxies show characteristics of both subclasses and are therefore classified as Sy 1.5 galaxies, like Mrk 926. These intermediate objects show strong narrow components but have HI emission line profiles in which both components are visible, which makes them composites. Further subdivisions apply accord-

ingly: Sy 1.8 with strong narrow components and weak Hα and Hβ lines and Sy 1.9 in which a weak broad Hα line, but no Hβ line is visible. (See also Osterbrock & Ferland (2006) for further investigations).
The currently most popular theory attributes the differences to different viewing angles. Antonucci & Miller (1985) suggested that the continuum and the emission regions are located inside an optically and geometrically thick dusty torus as already mentioned above, and that this thick obscuring material is the reason for galaxies being observed at large inclination angles to block the BLR and continuum source as seen in Sy 2s. Following this assumption, they are observed directly in Sy 1s (see also fig 1.6 further below). It is not yet known to what extend the narrow line region is obscured or how it depends on the orientation. Since the narrow line luminosity is sometimes substituted for the bolometric luminosity of Sy 2 nuclei the understanding of this matter is an important issue (Zhang et al., 2008).
Since the physics of AGN are not fully understood, the taxonomy of Active Galactic Nuclei are rather challenging. In comparison to other types of AGN, Seyfert galaxies tend to be of lower-luminosity with $M_{\mathrm{B}} > -21.5 + 5\,log\,h_0$ for the nucleus as the criterion to discriminate Seyferts from quasars (Schmidt & Green, 1983), where in Seyferts the host galaxy is still detectible. This is not the case for quasars, where the nucleus outshines the galaxy. On an adding note one has to consider, that the AGN of a Seyfert galaxy also emits brightly in the ultraviolet and the infrared, radiating at least three times its optical luminosity (Jones & Lambourne, 2004).

Quasars

Quasars are the most luminous of all AGN. Usually in comparison to Seyfert galaxies, quasars are spatially unresolved on the Palomar Sky Survey which was first consulted for this distinction. This means that quasars have an angular size of less than $\sim 7''$, some being surrounded by a halo comprised of starlight of the host galaxy (Peterson, 1997). A quasar's spectrum is similar to that of a Seyfert galaxy, although the absorption features and narrow lines are weaker. The main difference really is the high luminosity with nuclear magnitudes of $M_{\mathrm{B}} < -21.5 + log\,h_0$. Quasars can be reasonably well described by a power-law continuum with a typical index of $\alpha_\nu \sim 0.3 - 0.5$ (Vanden Berk et al., 2001). Accretion disk models can be obtained from raw data provided by surveys such as the Sloan Digital Sky

Survey, for which a comparison in optical/UV color distributions with respect to the soft and hard X-ray spectral index distributions is possible (Richards et al., 2004). In the composite spectrum of 700 quasars (see figure 1.4) the prominent and broad $Ly\alpha$ line which arises from the electronic transition in atomic hydrogen from the state n= 2 to n=1, is clearly visible.

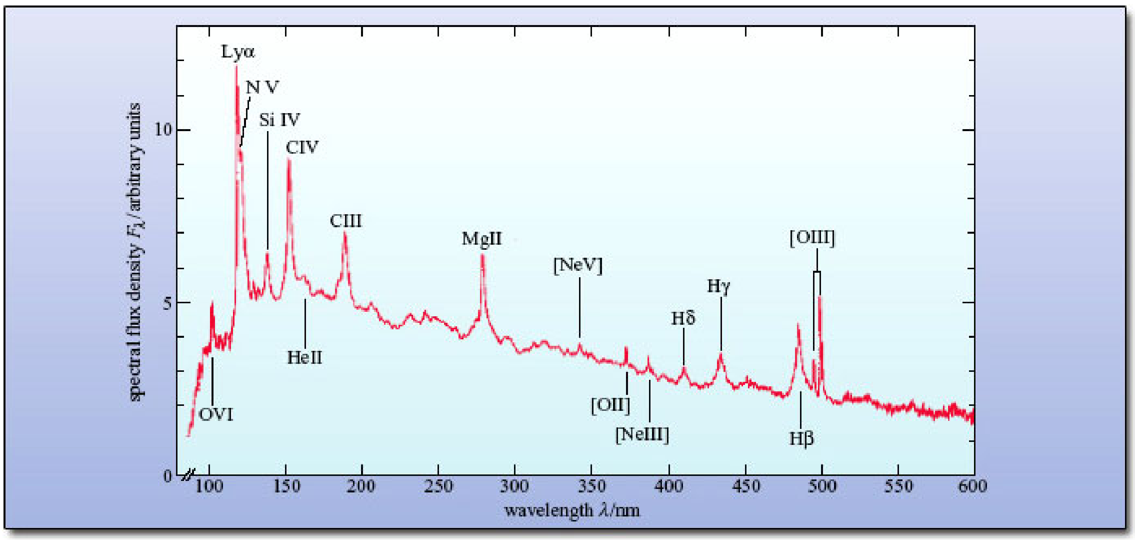

Figure 1.4: Optical spectrum of 700 quasars, corrected for redshift. Data courtesy of Jones & Lambourne (2004).

A small fraction of about 10 % of quasars are strong radio sources and sometimes called *radio loud* in comparison to *radio quiet* quasars for the old term QSOs. Often prominent jets ejecting material from the star-like nucleus can be observed in different wavelengths. The study of the galaxy itself turns out to be a challenge due to the great distances. Morphologically they seem to appear in all types of host galaxies, from ellipticals to spirals with many undergoing merging processes, usually of normal luminosities, outshined by the strong AGN.

LINERs

The main means to distinguish a Seyfert galaxy from a **L**ow-**I**onization **N**uclear **E**mission-**L**ine **R**region (LINER) is by their [OIII] luminosities. LINERs are older,

more massive, less dusty and more concentrated and they have higher velocity dispersions and lower [OIII] luminosities than Seyferts (Kewley et al., 2006b). LINERs are the least luminous of AGNs with narrow low excitation emission lines. They were first identified by Heckman in 1980 with the most prominent distinction to Seyferts being their strong low-ionization lines, e.g. [OI]λ6300 and [NII] $\lambda\lambda$6548, 6583. The distinction between LINERs and normal HII regions and other AGNs can be done by using the BPT diagram (Baldwin et al., 1981)), which will be discussed later in the text. Because of their low luminosities, LINERs are also referred to as low-luminosity AGN (LLAGN). It seems that up to about 1/3 of all galaxies have nuclear spectra typical of LINERs (Heckman, 1980). How these galaxies are powered is still under debate: fast shocks, photoionization by hot stars or photoionization by an old, metal rich stellar population, as well as compact radio cores and X-ray spectra, or UV variability that are observed in some LINERs are discussed as possible powering mechanisms. LINER emission has also been observed in extranuclear regions like outflows and jets, starburst driven winds and shock-heated material (Kewley et al., 2006b). It seems that massive stars do not contribute strongly to LINER spectra, but about half of all LINERs show high order Balmer absorption lines.
The distinction between Seyfert galaxies and LINERs is still unclear and some claim that they are closely related, only differing in their luminosity.

Radio Galaxies

Discovered by accident by radar engineers during second world war, they exhibit fast regions of radio emission (*radio lobes*) outside the host galaxy. Jets build a bridge between the galaxy and the much greater lobes to feed energy by ejecting material (see figure 1.5). The lobes of this very strong radio galaxy show bright regions where the material that's been driven out from the galaxy hits the intergalactic medium. Weaker radio galaxies look similar, but their jets always come in pairs whereas this is not necessarily true for strong radio galaxies. They also show bright nuclei and fainter lobes with sharp edges. When analyzing the lobes and the mechanics which make them shine, it is possible to explain their high luminosity, which exceeds that of a normal galaxy by a large factor and is powered by the AGN. The point like nucleus of any radio galaxy shows features typical for AGN, including emission lines, a broadband spectrum which is wider than that of a normal galaxy and variability (Jones & Lambourne, 2004). Centaurus A is

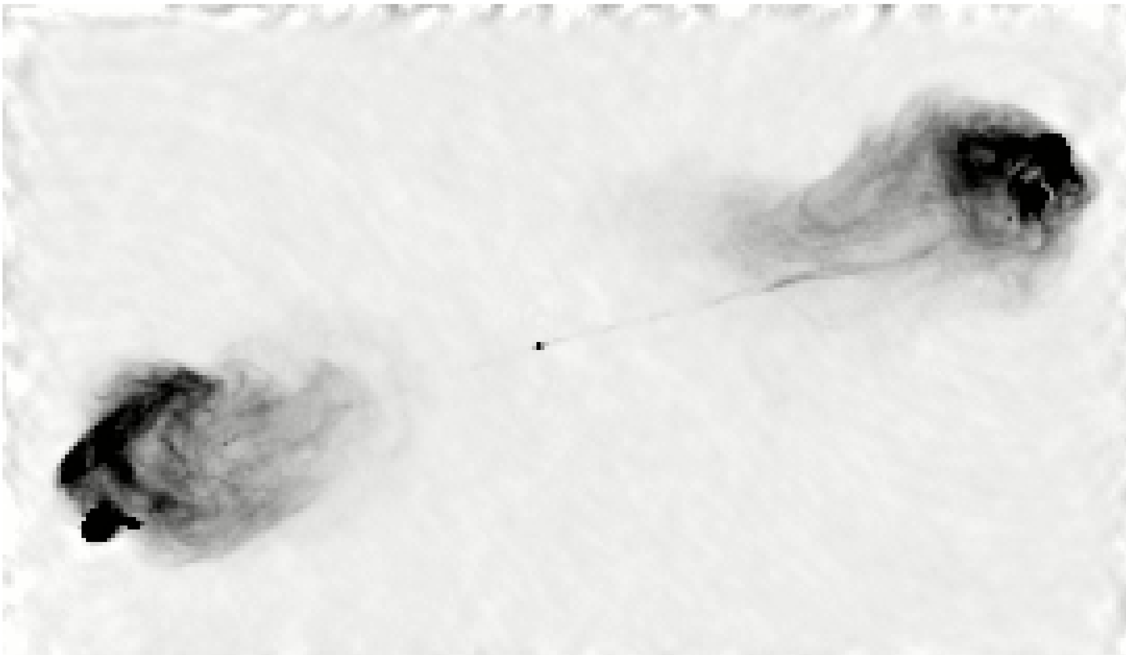

Figure 1.5: 6 cm radio image from the Very Large Array of the radio galaxy Cygnus A displaying both jets and Mpc scale lobes as well as the compact nucleus. Data courtesy: NASA/IPAC Extragalactic Database.

the nearest radio galaxy to the Milky Way and depicts an elliptical galaxy with a prominent dust lane bisecting it in the optical as well as largely expanding radio and X-ray features. The outer radio lobes expand over nine degrees of the sky. In X-ray observations done by Chandra for instance, a jet and the point like source can clearly be seen. So why do some galaxies show signs of radio-loud galaxies while others don't? While this is still under debate, the current theory predicts jets to be intervened with angular momentum of the Black Hole, with only the faster spinning ones being able to produce jets. It is now believed that high spin rates could be achieved not by accretion but by the merger of two massive BHs. The merging of two spiral galaxies (believed to be radio quiet) and the subsequent merging of their BHs results in an elliptical galaxy with a fast spinning BH which could produce such a jet (Jones & Lambourne, 2004).

Blazars: BL Lac Objects and Optically Violent Variables

A small subset of radio loud AGNs show short time-scale variations in flux that are abnormally large, e.g. $\Delta m \geq 0.1\,\mathrm{mag}$ in optical wavelengths. Furthermore, they seem to have higher polarization than most AGNs which also varies in magnitude and position angle. They are known as OVVs, **O**ptically **V**iolent **V**ariables (Peterson, 1997) showing stronger, broader emission lines than their counterparts, BL Lac Objects, and can be found at higher redshifts.
These BL Lac Objects, named after their prototype, on the other hand, lack in strong emission or absorption features. They merely show weak stellar absorption lines or weak nebular emission lines. They lie at relatively low redshifts and their host galaxies appear to be ellipticals. First this subclass of AGN was mistaken for variable stars until their spectra was studied (BL Lacertae is the variable-star designation given to the first object of this kind). Only about 100 BL Lacs have been found so far. Both OVVs and BL Lac Objects are sometimes referred to as "Blazars". It is believed that these objects have strong relativistically beamed components close to the line of sight (Peterson, 1997).

Related Objects

Starburst Galaxies show large scale star formation activity. This is the reason why they show blue colors and strong HII-region-type emission line spectra and strong radio emission due to recent SN remnants (Peterson, 1997). In general though, they do not show unusual activity in their nuclei. Even though treated together with AGNs in the past, more modern practice categorizes them as an individual class. Still there are active galaxies showing starburst activities. How exactly nuclear starbursts and AGNs relate is still unclear, they might be triggered by the same phenomenon - namely mergers and collisions.

1.2.4 AGN Surveys

There has been a number of major AGN surveys over the whole electromagnetic spectrum which strove to understand AGN evolution, their contribution to the cosmic background, AGN luminosity functions in different wavebands and co-evolution of AGN and galaxies among others (Mújica & Maiolino, 2004). The Chandra Deep Fields North and South (Brandt et al., 2002; Rosati & Chandra

Deep Field South Team, 2001) have certainly been cornerstones in observational X-ray number counts for both AGNs and galaxies. They have resolved the majority of the X-ray background (with it's energy density peaking at 30-40 keV) below $\approx$ 8 keV as well as measure the resolved sources quantitatively. Hard X-ray surveys claim to show most directly accretion unto the super-massive black hole which can be observed in the cosmic X-ray background spectral intensity (Fiore, 2004). Chandra and XMM Newton spectra (Cappelluti et al., 2009) provide a large sample of galaxies hosting active nuclei in the X-ray wavelength regime. The sensitivity of the instruments has allowed to show that the extragalactic X-ray background is largely comprised of the evolving populations of AGN, with normal galaxies being detected as well (Griffiths et al., 2004).
In the optical and infrared bands the SDSS (Sloan Digital Sky Survey) (York et al., 2000) can certainly claim the first price. The sheer number of imaging data in this redshift survey makes this survey the ideal environment to probe the physics of AGN. The investigation of emision line properties through analysis of continuum colors, line profile, and microlensing can be used to trace the inner structure of AGN. With some 10,000 square degrees of sky mapped in 5 photometric bandpasses (ugriz) the SDSS obtained spectra for the brightest million galaxies and brightest 100,000s of quasars (Richards et al., 2004). The large number of catalogued galaxies with more being added continuously, makes this database is the ideal playground for optical/UV continuum and emission lines.
Radio surveys sensitive to mJy levels like FIRST (Becker et al., 1995) or the GB6 (Gregory et al., 1996) open new possibilities of investigating the radio emission from extragalactic sources. These surveys contain millions of objects with high completeness and low contamination (Ivezić et al., 2004). Since the first high quality survey, the 3C survey, where 500 sources to a flux level of 9 Jy were discovered at a frequency of 178 MHz, several follow-ups have been published with both increasing sensitivities and sky coverage.
The 2dF quasar Survey of the AAT (Croom et al., 2004) provides redshifts of thousands of quasars up to z=3. The analysis of the given parameters provide insights into cosmological constraints.
In order to answer the questions relevant to star formation in the bulge and their connection to the growth of the central black hole, far infrared (FIR) data have been collected to look for dust emission. At redshifts z>1 the peak is redshifted into the submillimeter atmospheric windows. Earth-bound telescopes use the atmospheric windows to study starburst activity at high redshifts with the sensi-

tivity being almost independent of galaxy luminosity for a fixed spectral energy distribution (Omont et al., 2004). The IRAS (InfraRed Astronomical Satellite) all-sky survey in four wavelength bands centering at 12, 25, 60 and 100 μm has detected 10^5 sources (although a substantial fraction are stars) (Blandford et al., 1990). Results of the IRAS Survey show that estimates of the local space density of quasars may have been too low in previous surveys since nearby quasars, that had been missed before, were now found with IRAS. The majority of the IR emission seems to originate from a small area few kpc across holding a large amount of molecular gas ($10^{10} - 10^{11} M_{\odot}$). Higher luminosities seem to stem from interacting systems which take up the majority of the IRAS Bright Galaxy Survey. These findings gave rise to speculations stating that the merging molecular clouds lead to higher star formation rates which are subsequently followed by the merging of the nucleii with gas streaming inwards to feed the AGN. The surrounding dust is then driven out by the radiation pressure and thus exposes the inner parts. Relatively more energy is radiated at shorter wavelengths and the quasar emerges (Blandford et al., 1990).

Nearby AGN have been catalogued fairly early. The NGC as well as the Revised Shapley Ames Catalogue (Sandage & Tammann, 1981) have been used for statistical studies (see Table 1.1) like Véron-Cetty's and Véron's (Veron-Cetty, 1984) study of 320 nearby bright galaxies from the RSA.

Table 1.1: Numbers and percentages of Seyfert galaxies in the Revised Shapley Ames Catalogue

Class	Sy1	Sy2	Total RSA	%Sy
E - S0/a	6	0	361	2
Sa - Sab	11	11	165	13
Sb - Sbc	9	11	283	7
Sc	2	3	370	1

The fraction of Sa - Sbc galaxies which are Seyferts has since increased as new instrumentation made better observations and thus studies possible. LINERs seem to be even more possible (Blandford et al., 1990) now. In conclusion it can be said, that the collective work of previous surveys and follow-up surveys, which are undoubtedly going to be presented in the future, have been and will be the most valuable tool for statistical studies of all objects connected to AGNs.

1.2.5 Basic Physics

In general, an AGN produces luminosities of $2 \times 10^{10} L_{\odot}$ which represents a value of 10^{38} W as the characteristic luminosity. It therefore produces an enormous amount of power in a very small volume. This source is know as the central engine.
The idea that most phenomena observed in the centers of active galaxies are due to a central supermassive Black Hole (SmBH) is widely accepted today. Observations show that massive Black Holes (BH) have been present as early as z$\simeq$ 6 accreting matter at a high rate. In fact it has been shown that a smaller Black Hole of mass $2.6 \times 10^6 M_{\odot}$ lies within our own Milky Way. When describing BHs, and their basic properties, the gravitational (r_g) and Schwarzschild (r_s) (the radius of the event horizon where the escape speed is just equal to the speed of light) radii have to be defined.

$$r_{\rm g} = \frac{GM}{c^2},\, r_{\rm s} = 2r_{\rm g}. \tag{1.2.3}$$

The Schwarzschild radius can be assumed to be 3×10^{11}m. The angular momentum s of a BH can be defined as

$$s \backsim I\Omega \simeq M r_{\rm g}^2 \frac{v}{r} \simeq M r_{\rm g} c, \tag{1.2.4}$$

with Ω being the angular velocity. Considering equation (1.2.3), one can see that SmBHs hold masses of $\backsim 10^6 - 10^{10} M_{\odot}$ and specific angular momenta (angular momentum per unit mass) of

$$s/M \equiv a\, c \backsim r_{\rm g} c \backsim 5 \times 10^{23} M_8\, {\rm cm}^2\, {\rm s}^{-1}, \tag{1.2.5}$$

where M_8 is the mass in units of $10^8 M_{\odot}$. Assuming an efficient grow of the BH through accretion of material towards the central region in timescales typical of galactic evolution, there must exist an efficient mechanism to overcome the angular momentum barrier of the accreted gas (Netzer, 2006). Possible mechanisms are merging events and bar instabilities where an initially small perturbation enables the formation of a temporary bar which subsequently transfers material. (Márquez & Masegosa, 2008). Several other mechanisms have been proposed to

describe the loss of angular momentum that is seemingly necessary to fuel the BH (e.g. Maciejewski & Binney, 2001; Jogee et al., 2004). A general understanding of how gas particles close to the center are accreted is given in the following overview of the basic physics and main components of AGNs. Most of the following information is taken from Netzer (2006) and Jones & Lambourne (2004).
The Eddington Luminosity can be described assuming a central source of mass M emitting monochromatic luminosity L_ν. The gravity and radiation pressure force need to balance out; the radiation pressure force acting on gas particles at a distance r is given by

$$f_{\rm rad} = \frac{N_{\rm e}\sigma_{\rm T}}{4\pi r^2 c}\int_0^\infty L_\nu d\nu = \frac{N_{\rm e} L \sigma_{\rm T}}{4\pi r^2 c} L, \tag{1.2.6}$$

where L is the total luminosity, $N_{\rm e}$ is the electron density and $\sigma_{\rm T}$ the Thomson cross section. The gravitational force then is given as

$$f_{\rm g} = \frac{GM\mu\, m_p N_e}{r^2}, \tag{1.2.7}$$

where μ is the mean molecular weight (mean number of protons and neutrons per electron; typically 1.17 for a fully ionized solar composition gas as given by (Netzer, 2006). Only if $f_{\rm g} > f_{\rm rad}$, spherical accretion (or Bondi accretion) of fully ionized gas is possible.The requirement $f_{\rm rad} = f_{\rm g}$ leads to the Eddington luminosity, the maximum luminosity allowed for objects that are powered by steady state accretion of fully ionized plasma (Netzer, 2006):

$$L_{\rm Edd} = \frac{4\pi GM\mu\, m_{\rm p}}{\sigma_{\rm T}} \simeq 1.5\times 10^{38}(M/M_\odot){\rm erg\,s^{-1}}. \tag{1.2.8}$$

Since in reality gas is partly neutral and partly ionized, the effective $L_{\rm Edd}$ will be significantly smaller than the value given here.

The Eddington accretion rate, $\dot{M}_{\rm Edd}$ which is required to produce$L_{\rm Edd}$ is given as

$$\dot{M}_{\rm Edd} = \frac{L_{\rm Edd}}{\eta\, c^2} \simeq 3\, M_8 \left[\frac{\eta}{0.1}\right]^{-1} M_\odot\,{\rm y}^{-1}, \tag{1.2.9}$$

with η as the efficiency of converting gravitational potential energy to electromagnetic radiation. Finally the Eddington time, $t_{\rm Edd}$ can be defined as the typical time associated with this accretion rate:

$$t_{\rm Edd} = \frac{M}{\dot{M}_{\rm Edd}} \simeq 4 \times 10^8 \, \eta \, yr. \tag{1.2.10}$$

Assuming spherical accretion, accretion starts form a large radius with the gas being at rest towards the central region in radial motions under the forces of gravity and radial pressure, stopping at the event horizon. The optical depth of this particular gas is large while the radiation conversion efficiency η is very small. This is due to the fact that most of the radiation emission is caused by two body collisional processes in the ionized gas. The released gravitational energy prevails and is advected into the central object. The infalling gas sinks into the central plane while retaining most of the angular momentum and forms an accretion disk. The disk, if thick enough, transfers angular momentum out and allows gas falling into the vicinity of the BH.
We can picture this process in an easily understood way, by imagining the following: Gas clouds moving around the BH will be accelerated by the hole's gravity. The clouds reach their maximum speed when closest to the BH and collide with each other, thus losing some of their just gained kinetic energy. Therefore some of the gas clouds will slow down sufficiently enough to be drawn into circular, keplerian orbits while the collisions heat up the gas. (The kinetic energy is thus transferred to thermal energy within the clouds.) Due to their different speeds, the orbits will be exposed to friction, again resulting in heat. The inner parts of the orbits will therefore fall into even smaller orbits spiraling inwards until a complete accretion disc is formed. Angular momentum is redistributed so that most gas is moving inwards. The thermal energy of these viscous gas disks around the BH is so high that they become luminous sources of electromagnetic radiation. At the event horizon, situated at a few Schwarzschild radii, the heat can be radiated away as electromagnetic radiation and infalling material is quickly drawn into the Black Hole. The energy that's been radiated away is believed to be the responsible drive for the large power of an AGN. The basic principles of accretion disks are shown below as given in Netzer (2006): For optically thick and geometrically thin accretion disks one has to consider the physical parameters angular momentum of the material in the disk at radius $r, s(r)$, the net torque associated with this angular momentum, $N(r)$, and the radial drift velocity of the gas, $v(r)$.

The angular momentum of a ring of radius r with total (time independent) mass m can be described as

$$s = m\, v_\phi\, r, \tag{1.2.11}$$

where v_ϕ is the azimuthal velocity. The radial mass flow rate of a stationary disk, $\dot{M}$, is constant and is given by

$$\dot{M} = -2\pi\, r\, \Sigma\, v_r. \tag{1.2.12}$$

Σ is the surface mass density of the disk (cm^2) which is also time independent. When angular momentum conservation is taken into account, i.e. the angular momentum going inwards outbalances the angular momentum carried outwards by the torque, one finds

$$N(r) = \dot{M}[GMr]^{1/2} + const. \tag{1.2.13}$$

The smallest, innermost radius of the accretion disk can be found where the Kaplerian motion breaks down. This "last stable orbit" is a function of the angular momentum of the BH.

The energy released at various radii is determined by the luminosities associated with the loss of gravitational energy of material being accreted inwards, L_g and the work done by the torque that results in outward loss of angular momentum L_N:

$$\frac{dL}{dr} = \frac{3GM\dot{M}}{2r^2}\left[1 - \left(\frac{r_\mathrm{in}}{r}\right)^{1/2}\right]. \tag{1.2.14}$$

Here the innermost radius, r_in is taken into account. Integrating over the entire disk yields the total radiated power,

$$L = \frac{1}{2}\frac{GM\dot{M}}{r_\mathrm{in}}. \tag{1.2.15}$$

This lies in the non-relativistic limits and stands for half of the total available power. This means that the matter at $r_{\rm in}$ retains a kinetic energy half of the potential energy it has lost. A substantial amount is released close to $r_{\rm in}$ which denotes that relativistic corrections are indeed important. Most of the ionizing radiation is released in the central regions of AGN at radii of the order of $\sim 10\,r_{\rm g}$ (Netzer, 2006). Calculations show that infalling mass m can radiate energy of about $0.1\,mc^2$, or about $10\,\%$ of its rest energy before it disappears, thus creating (together with matter-antimatter annihilation) the most efficient process for converting mass into energy ever conceived (Jones & Lambourne, 2004). The luminosity depends on the infalling rate of the matter, the mass accretion rate, which can be calculated to about $0.2\,M_\odot$ per year (considering a luminosity of $L = 10^{38}$W and therefore a mass accretion rate $Q \sim 10^{22}\,\rm kg\,s^{-1}$). The power that can be produced is limited through the Eddington limit. Accretion will cease when the gravitational force outbalances the radiation pressure on the gas.
When one assumes local emission as a blackbody with temperature T and an emissivity $D = \sigma T^4$, the disk temperature at all radii can be expressed as the following:

$$T(r) = \left(\frac{3GM\dot{M}}{8\sigma\,\pi\,r^3} \left[1 - \left(\frac{r_{\rm in}}{r} \right)^{1/2} \right] \right)^{1/4} . \tag{1.2.16}$$

In a thin accretion disk around a BH with M_8=1, the temperature is $T(6r_{\rm g}) \sim 10^5$ K with most of the energy being emitted in the UV. In comparison, the maximum blackbody temperature around stellar-size BHs is bout 10^7 K, with most of the energy being emitted in the X-ray. Therefore one can conclude that massive black holes are much cooler and $T(r) \propto r^{-3/4}$.
To investigate the radial velocity v_r, which is determined by the viscosity of the disk, one has to take microphysical processes of the disk material into account as well as the turbulence, the magnetic fields strength and structure, etc. (e.g. Blandford et al., 1990). Because of a variety of models, it is fair to speak of a “family of disk models”where the simplest form combines the accretion rate (1.2.12) and the torque (1.2.13) with the definition of $\nu = \alpha v_s H$ (and α includes all unknown disk microphysics):

$$v_r = \frac{3\nu}{2r} \ll v_s. \tag{1.2.17}$$

This shows that the radial inflow is subsonic. All of the above considerations are for geometrically thin accretion disks, although disks can be thin, slim or thick, depending on the mass accretion rate. Some AGN (e.g. narrow line Seyfert 1 galaxies and very high luminosity quasars) accrete at rates close to or exceeding the Eddington accretion rate. These galaxies are candidates for hosting a slim or thick accretion disk (Netzer, 2006). Assuming a thin disk can be problematic since they do not represent the entire emitted spectral energy distribution (SED) properly because a substantial fraction of AGN energy is emitted in the X-ray whereas the maximum disk temperature cannot exceed few 10^5 K. An additional hot dilute gas medium which is transformed to X-ray energies via Compton scattering is often assumed. Narayan (2005) suggests accretion through the outer layers of the disk which results in large temperature differences assuming a steep rise. The outer skin can expand and the disk develops a hot corona which would modify the emitted spectrum. This is only one of many theories which are difficult to calculate when all effects are taken into account. Real disks are complicated with many substructures and simplified configurations can only begin to grasp their structure and physics with magnetic fields influencing the disk viscosity and winds adding to the complicated scenario.

An AGNs SED is relatively flat compared to that of a normal galaxy due to the higher emission at X-ray and radio wavelengths. Many active galaxies are bright in these regions, and this feature is called “big blue bump”and said to be lying between X-ray and near UV-parts of the spectrum. In others, a spectral excess in IR emission is detected. Whatever the case, the total energy output of an active galaxy is several times that of a normal galaxy.

A key question that still needs to be addressed when talking about the central engine of AGNs is the formation of Jets. Both quasars and radio galaxies often show narrow features projecting far from the nuclei (up to several hundred kiloparsecs). Even though jets are far from being fully understood, some key aspects should be revised at this point: jets are probably aligned with the axis of rotation of the disc with material ejecting at relativistic speeds. One idea revised by Jones & Lambourne (2004) involves the possibility that the accretion disc becomes thicker closer to the central Black Hole and forms a pair of opposed funnels aligned with the rotation axis. The emission of radiation produces intense radiation pressure which acts to channel the material. Through this, material is believed to be ejected out along the rotation axis. Nevertheless, the main drawback of this idea is the fact that this process cannot produce beams of energetic particles enough to

explain the real jets. Magnetic fields may play a significant role in creating these jets. In many quasars and radio galaxies though, only one jet can be observed. This could be explained by the effect called *relativistic beaming* through which the radiation is concentrated in the forward direction. The beam pointing towards us, the observer, appears much brighter.
Figure 1.1 shows a basic model of an AGN. The central engine, composed of the SmBH and its accretion disc, is surrounded by a thick dusty torus. Inside this doughnut-shaped torus, one can see clouds form the broad-line region, with the narrow line region believed to lie further out. The idea of a surrounding torus of gas and dust stems from strong infrared emission of $1.5\,\mu$m or longer, of many AGNs which can be observed in addition to the X-rays and UV radiation from the hot accretion disc. The dust radiates at the same temperature rate at which they are heated from the engine, but must be lower than 2000 K, which is the temperature at which graphite would vaporise (Jones & Lambourne, 2004). Most of the radiation emitted from AGNs is therefore observed in the infrared with variations much slower than from X-rays or optical wavelengths. This is understandable, considering that the torus extends much further than the central part where shorter wavelengths are formed (with the exception of BL Lacs where it is probable that most of the infrared radiation also stems from the engine). The radius of the inner edge of the dust torus can be expected at a distance of $\sim 0.2\,$pc for an AGN of luminosity 10^{38}W, having three or four orders of magnitudes higher luminosities than the accretion disc. The idea that this extended torus provides material to be funneled into the central engine has been suggested but not yet proven.
Summarizing the ideas that have been put forward, one can say that essentially all AGNs are the same, but differ in luminosity of the central engine depending on the mass of the BH and the mass accretion rate. Secondly, the inclination angle of observation is a crucial factor in classifying the AGN. The dust torus - if it really exists - can obscure the radiation from the inner part and will therefore play a major role in the classification scheme. Figure 1.6 shows the unified model of AGNs (Jackson & Wall, 1999), both radio-loud and radio-quiet AGNs; a revision of what has been stated in the section about Seyfert galaxies.

When looking at radio-quiet AGNs from an angle close to the rotation axis of the torus (pictured above in Fig. 1.6), one will observe X-ray, UV and other radiation from the engine as well as the BLR, and narrow lines from the NLR and infrared from the dust torus (just like in a Seyfert 1 galaxy). Looking at the same

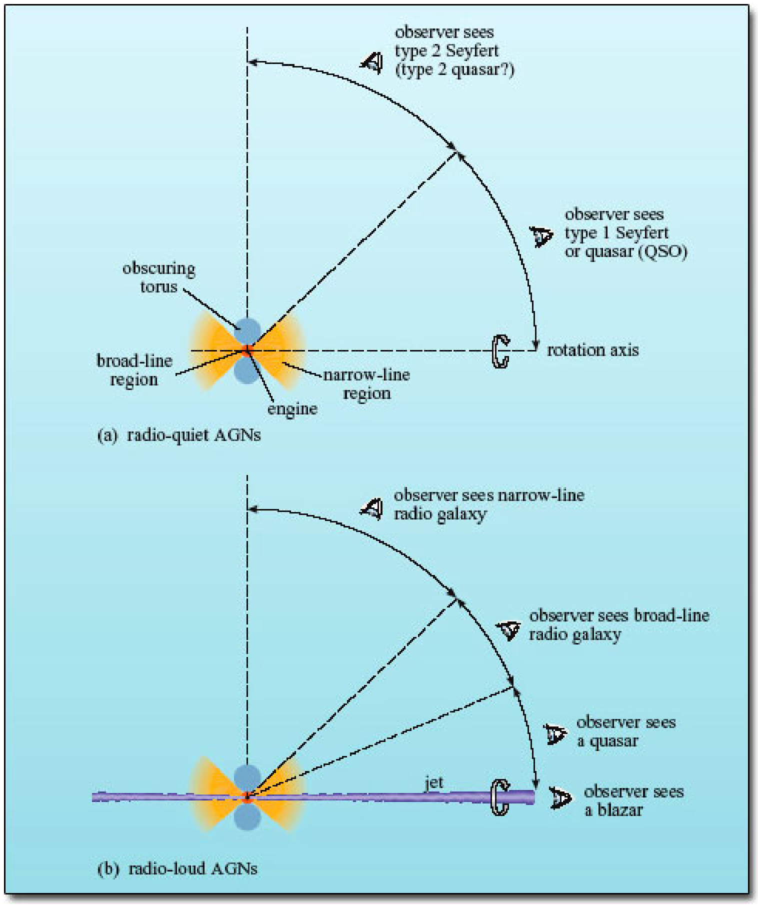

Figure 1.6: Two unified models of AGNs. Recent studies have shown that a type 2 class for quasars is very likely to exist and intensive studies are performed that further investigate on the matter. Data courtesy: The Open University.

model from a different angle near the plane of the torus, only features associated with type 2 Seyferts are visible. X-ray and broad line emission is absorbed by the torus. This fact significantly changes analyzations of Sy 2 galaxies, which will be relevant for later discussions and should be kept in mind. The same applies to quasars, but they show higher luminosities. Type 2 quasars are a matter of more recent debate and new observations of highly luminous galaxies emitting strongly in the IR may be just that (e.g. Villar-Martín et al., 2008).

Radio loud AGNs (lower picture in Fig. 1.6) show an additional jet. So when looking at the galaxy from an angle closer to the rotation axis, which is also the jet axis, the broad line region is visible and a broad line radio galaxy can be observed. (Compared to that, when looking at the galaxy from a wider angle, one expects to see narrow lines and two jets with lobes only.) Because of relativistic beaming, the approaching jet can be seen brighter than the other one, and with decreasing angle, one jet will fade completely. When decreasing the angle further, the intense radiation around the BH comes into view and a luminous quasar is observed. When looking straight onto the jet with the torus face-on, a blazar is seen. The blazar's spectrum is dominated by the smooth continuous spectrum of the radiation of the jet, varying rapidly over all wavelengths (Jones & Lambourne, 2004). In this sense, the different types of AGNs are simply created by different viewing angles.
Some questions still remain unanswered: Does a supermassive Black Hole (smBH) really exist? And is this activity just a phase that every galaxy has to go through or are AGNs a class on their own? The first question can be investigated by looking at the galaxy's rotation curve and the variations that are shown in the lines and the continuous spectrum, from which the enclosed mass can be calculated. Indeed, astronomers have calculated the masses of the central BH to be of $10^6 M_\odot$ and higher, implying that SmBH reside in the centers of AGNs. The only other hypothesis trying to explain the amount of power for an AGN in the small volume given, is the idea of a nuclear starburst model, where a cluster of young, massive stars with frequent supernova explosions accounts for the the observed parameters, but this model does not fit the observations well.
The possibility that SmBH were formed in mergers is an attractive one. These disturbances could provide the material needed to fuel the growing BH and to stimulate AGN activity. Some studies found out that active galaxies are more likely to be gravitationally linked to a companion galaxy (15 % of Seyferts have companions compared to 3 % of normal galaxies) and many active galaxies are the result of recent mergers. (e.g. Smirnova et al., 2006; Sánchez et al., 2004; Canalizo & Stockton, 2001; Sánchez & González-Serrano, 2003), although just as many are found that there is no obvious AGN/merger connection.
How long do AGNs live? Considering that the density of quasars seems to have reached a peek around $z \sim 2 - 3$, or 10 billion years ago, declining afterwards, they must have been 10^3 times more common at that time (Jones & Lambourne, 2004). A compelling idea therefore is, that AGNs are shortlived and leave behind

a normal galaxy with a SmBH in the center of the host galaxy. And indeed, *relic* smBHs are found in many galaxies, with a $2 \times 10^6 M_\odot$ BH residing at the center of our own galaxy. Though this might be true - i.e. that normal galaxies observed today have gone through an active stage some time ago - there is no proof for this theory. But what has happend to stop the active phase, if indeed that is true? After all, only one solar mass or less is needed to fuel the AGN. It is thought that the AGN *sweeps clean* of the gas immediately surrounding the BH and that this gas is not replenished from clouds further away. Therefore the mass accretion rate will drop and - unable to fuel the AGN - the active galaxy will fade. Of course it would be possible to temporarily restore this by some disturbance like a merger or collision - this is what might be happening right now to Centaurus A and may well happen to the Milky Way in the future.

1.2.6 Statistical analysis of AGN, the BPT diagram

Emission lines of AGNs show different kinds of ionization in all elements. Investigations of the lines, their shape and their ratios, give information about the kind of emission in this region. The general idea that is believed to be true is that of a number of small, dense optically think moving clouds photonized by a central nonthermal continuum source (Basu, 1994). It is still unclear whether the clouds are falling into the center, flying outwards or rotating about the center. These questions will be looked at in more detail below while investigating the galaxy UGC 1935.

In order to understand the excitation mechanisms in galaxies, emission lines of different excitation levels are used. If spectra are used, various line ratios can help distinguish between AGNs, LINERs or H II emission line (regions) with the help of diagnostic diagrams. This was first done by using longslit spectra which give information in one-dimensional space. Emission line imaging using narrow band filters centralized on the line in question, provide two-dimensional coverage. Integralfield spectroscopy now has the same advantage, but gives additional information of all lines within the wavelength range of the used grism. Therefore the result is an excitation map as a function of the position within the galaxy. The $[OIII]/H\beta$ ionization maps created here and discussed in 5.2, are part of the well known BPT diagrams (see Fig. 1.7).

This diagram is used to distinguish different types of AGN. It is based on the flux ratios of $[OIII]\lambda 5007/H\beta$ on the vertical axis and $[NII]\lambda 6583/H\alpha$, or $[SII]\lambda 6716, 6731/H\alpha$ on the horizontal axis. These lines are chosen to be close in wavelength to lower the reddening effect to a minimum. They also have to be strong lines, so measurements are easily done and should stand out as single lines without blending into others. Ratios of one element to an H I Balmer line are the best to use because they are less abundance-sensitive (Veilleux & Osterbrock, 1987). Therefore the uncertainties here, also when comparing with other data sets, are always depending on the instrument used, the strength of the lines, and whether the lines are blended with others. In these schematics, Seyfert galaxies have higher values of these ratios than H II regions.

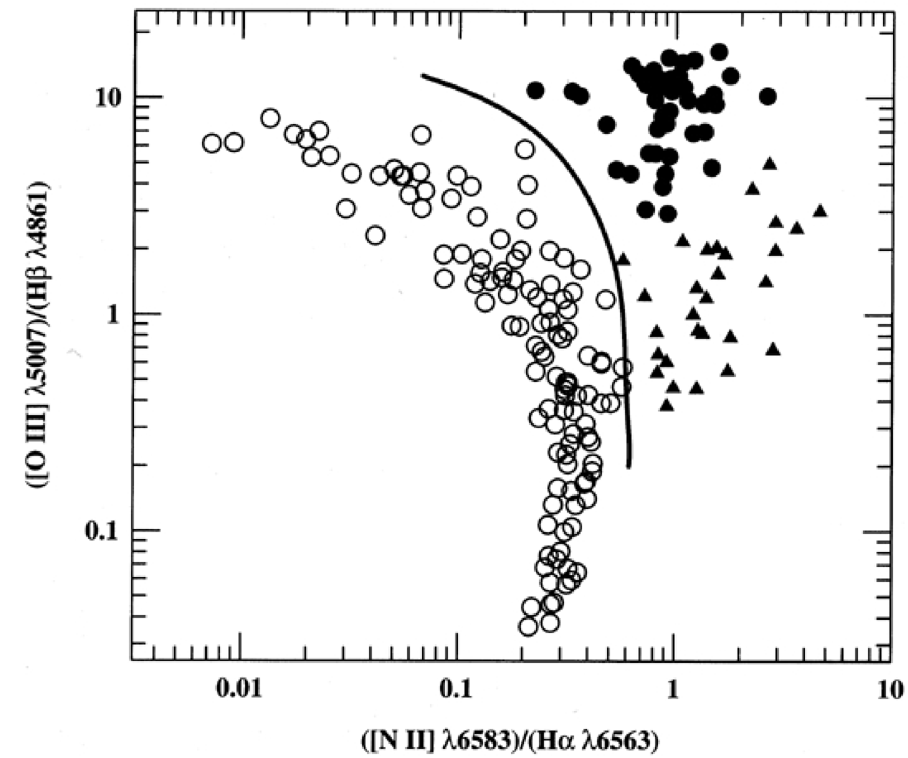

Figure 1.7: BPT diagram for emission-line galaxy diagnostics. Open circles indicate H II regions, ionized by hot stars, closed circles are narrow-line AGNS which are ionized by harder continua, e.g. power law spectrum high energy photons. Triangles represent LINERS. Figure courtesy of R.W. Pogge based on data from Veilleux & Osterbrock (1987), taken from Peterson (1997).

It seems both Seyfert 1 and Seyfert 2 galaxies are ionized by power-law continua

$\nu^{-\alpha}$ with spectral index $\alpha \sim 1.0-1.5$, down to $\alpha \sim 0.5$ at higher energies (Ferland & Osterbrock, 1986). The definition using emission line ratios to distinguish the two is the following: Any galaxy with $[OIII]\lambda5007/H\beta \gtrsim 3$ is considered to be a Seyfert 2 galaxy.

An alternative for power-law heating is shock heating which can be considered as a possible ionization mechanism in narrow line AGNs. Different ionization mechanisms and discriminations have been implemented to newer versions of the BPT diagram as lines (e.g. Kewley et al., 2006b; Shull & McKee, 1979). The physical difference between narrow-line AGN and H II region like galaxies is the photoionizing continuum. In addition, narrow-line AGNs show a lot of their radiation in the X-ray wavelength range, penetrating deeply into the neutral region and thereby ionizing the hydrogen. This is true especially for Seyfert 2 galaxies, narrow-line radio galaxies, and LINERs (Veilleux & Osterbrock, 1987).

Most LINERs show $[OIII]\lambda5007/H\beta < 3$ while additionally showing much weaker emission lines arising from an area of partly ionized hydrogen. This zone is extended in galaxies ionized by a spectrum with lots of high-energy photons (Veilleux & Osterbrock, 1987).

O^{++} is mainly produced by a large number of UV photons with ionization energies greater than 35 eV. The process of ionizing hydrogen takes place close to the source, in the innermost regions of the galaxy. Here, X-ray photons do not contribute to the ionization as much as outside of the inner ionized zone. Therefore, generally speaking, the ratio of $[OIII]\lambda5007/H\beta$ is larger in AGNs than in H II region-like objetcts.

2 Key ideas and starting point

No mechanisms have been agreed on to be responsible for initiating an active galaxy. The fueling of material towards the center of the host galaxy is one possibility that shall here be investigated further. When observing AGNs in the visible light, only a small number is visibly disturbed. Kuo et al. (2008) have found in their research, that while only 28 % of their analyzed set of galaxies is visibly disturbed in the optical DSS2 images, ∼94 % show disturbances in HI, on spatial and kinematical scales. They also suggest as a result, that most Seyfert galaxies with high nuclear luminosities have experienced tidal interactions in the recent past and that in most cases these tidal interactions are responsible for initiating events that lead to their nuclear activity. AGNs themselves are the best possible evidence for accretion of gas towards the SmBH and it makes sense to investigate this type of galaxy further to shed light onto this question. A mass accretion of a minimum of $\sim 0.1\ M_\odot\,\mathrm{yr}^{-1}$ is required to account for the common magnitudes, assuming a 10 % efficiency for the conversion of infalling matter into radiation (Norman & Silk, 1983). Considering a lifetime of $\sim 10^8\,\mathrm{yr}$, the total amount of matter that is required to feed the SmBH in order to ignite an AGN, is therefore $\sim 10^5 - 10^7\,M_\odot$ (Kuo et al., 2008).

2.1 Chemical evolution of galaxies

Chemical abundances are a key to understanding the evolution of galaxies. H II regions – ionized regions around very hot stars – in extragalactic objects are the main source for chemical abundance measurements. These measurements enable statements of metallicities as well as metallicity gradients of galaxies. As stars in galaxies continuously produce elements and enrich the interstellar medium through stellar winds and supernovae, these elements, from helium to heavy elements or metals are constantly build up. This is the meaning of galactic chemical evolution. As this evolves through time, the abundances of helium and heavy

elements increase relative to hydrogen. Second generation stars formed from the enriched material are already in possession of more heavy elements. The end of this enrichment cycle is only reached when enough material is locked up in stellar remnants rather than being freely available in the ISG to stop the production of new stars. Measurements of these element abundances in the ISM as well as stars are possible even in other wavelength ranges than the optical, accessible through space telescopes. The study of ionization regions have opened new horizons to understanding the evolution of galaxies and their environment from the big bang to present time. Much information is found in Henry & Worthey (1999) from which parts of the following are taken.
In fact the study of gaseous nebula was also the bridge to studying AGN (Osterbrock & Ferland, 2006), with early nebular studies focusing on planetary nebulae and H II regions in our own galaxy. Even though the abundances are comparable to those in the sun, the differences depend on the element, location and stellar population (Shields, 2000). These abundance informations can be identified through analysis of emission lines – or absorption lines, if the situation calls for it. More precisely, as stated in Henry & Worthey (1999), the examination of N/O lines vs. O/H lines of spiral disk galaxies denotes how the production of N is dominated by primary processes at low metallicity with secondary processes being dominated at high metallicity. Oxygen, neon and sulfur, amongst others, result from primary production of stellar nucleosynthesis. Nitrogen, on the other hand, is a secondary product. Therefore, the yield is proportional to the abundance of C and O in the progenitor (Shields, 2000). Furthermore, the O/Fe ratio is an indicator for the timescales of the life and death of stars, due to the fact that Fe needs some time ($\sim 10^9$ yr) to build up and to be distributed through type Ia supernovae.
Only a short reference to the "G dwarf problem"should be given here. It refers to the fact that there are too few main sequence stars that are metal poor as a function of abundance in the solar neighborhood. The simple models from van den Bergh (1962) and Audouze & Tinsley (1976) suggest otherwise. This is a constraint on chemical evolution models of galaxies. Larson (1972) suggests that the abundances obtain an asymptotic value due to the infall of metal poor gas. At this value most stars are then formed.
It is now known that chemical abundances measured throughout the disk galaxy, including heavy element abundances (metallicities), decrease outwards as well increase with larger luminosities. The global metallicities increase with galaxy

mass. This is true even for high redshift galaxies where emission line studies of QSOs underline the given theory. The chemical evolution of galaxies seem to be effected by the cluster environment. In spiral galaxies, like the Seyfert galaxies that are looked at here, the local metallicity seems to be correlated with total surface density. In Henry & Worthey (1999) it is furthermore explained that carbon production increases with increasing metallicity, whereas the abundance ratios Ne/O, S/O, and Ar/O are *not* dependent on metallicity, but rather, they seem to be universally constant. He further argues that this would mean that either the initial mass function (IMF) is universally constant or these ratios are not sensitive to IMF variations.

In order to study the chemical evolution of galaxies, a number of processes need to be understood. It is curial for example, to know the details of star formation processes and evolutions as well as stellar nucleosynthesis and how many heavy elements are produced. Similarly the knowledge of how the stars lose their outer layers in stellar winds and ejections and how the mixing of gas ultimately distributes the elements is important. One can see how complicated the interactions are if one wants a comprehensive and full picture of the evolution of a specific galaxy. Obviously, models are only able to show a basic picture of these processes depending on the input parameters. Observations give information of abundances in terms of abundance ratios of heavy elements relative to hydrogen (O/H or Fe/H). Since heavier elements are produced only later in time, this is a good indicator as to how far the galaxy has progressed. These ratios therefore give information about the star formation rate and the evolution thereafter. Additionally, ratios of two heavy elements, such as N/O or O/Fe provide information about differential element production (how the elements are produced relative to one another) by stars. This points towards production rates as a function of stellar mass weighted by the relative number of stars at each mass as well as the history of star formation, and stellar yields (see Henry & Worthey (1999) again for details).

The analysis of emission line spectra provides the most direct way of determining interstellar abundances. For H II areas, gas is ionized around an association of hot ($T \geq 25000\,\mathrm{K}$), young stars (e.g. OB stars) and ionized with an ionization energy of 13.6 eV for hydrogen which corresponds to a wavelength of 912 Å. The temperature and pressure around the star rises and the ionization front expands supersonically into the ambient medium. The front compresses the interstellar medium and expansion velocity is reduced. The size of this H II region in which the heating of the interstellar gas by the shockwave produces emission lines, is given by the Strömgren radius and serves as the ideal test area for emission line probes. Planetary nebula and supernova remnants hold the same criteria where emission lines can be analyzed. Ionized gases of this kind are in temperature equilibrium due to the radiation of photons at discrete wavelengths. These photons ionize the hydrogen atoms but recombine immediately in cascade motion or trigger excitation processes due to collisions of ions with electrons. The spectra therefore show emission lines which can be analyzed, yielding information about abundances, temperature and density (Henry & Worthey, 1999). While emission lines of oxygen are prominent in these vicinities, only old stars can show absorption features of iron. Iron therefore is usually a metallicity indicator for old stars. In summary there are three methods to estimate element abundances of H II regions:

1. The *direct* or T_e*-method* that uses electron temperature deduced from sensitive emission lines like [OII] λ3727 (e.g. Pilyugin et al., 2009)

2. The *empirical* or *strong-line method* uses the R_{23} (e.g. Pagel et al., 1979; Pilyugin & Thuan, 2005) index, N2 index (e.g. Storchi-Bergmann et al., 1994) or O3N2 index (e.g. Alloin et al., 1979) and measurements of various strong emission line ratios

3. The *theoretical methods* uses photoionisation models and emission-line fluxes (e.g. McGaugh, 1991).

2.2 Metallicity gradients in galaxies

Radial gradients in chemical composition can be studied to find out about the characteristics of both spiral and elliptical galaxies of different types. In general, the variations of emission line intensities as a function of galactocentric distances show radial increases or decreases of various abundance ratios.The observational analysis (e.g. Aller, 1942; Searle, 1971) were followed by computer models of nebular ionization and thermal structure (e.g. Shields & Searle, 1978). With the increase of the number of galaxies available for investigation, statistics were done to find out general trends. Through this, it has been possible to acknowledge certain commonnesses in different types of galaxies: gradients of galaxies with a bar

are substantially shallower than galaxies without such a bar but have similar overall abundances (Martin & Roy, 1994); galaxies exhibiting low surface brightnesses have low abundances compared for their mass (McGaugh, 1994); local abundances increase with local surface brightness or surface mass density (McCall, 1982; Vila-Costas & Edmunds, 1992).
Metallicity "is the fraction by mass of all elements heavier than He in a system and is the primary indicator of chemical evolution as stars convert H into heavier elements and seed their environments with the products "(Henry & Worthey, 1999). For this, it is most goal-oriented to analyze Oxygen abundances as the tracer of metallicity in the interstellar medium. Oxygen is the most common element after H and He and it's low depletion leads to O being present almost entirely in the gas phase. In our Milky Way Galaxy (MWG), a monotonic decrease in oxygen abundance with galactocentric distance is visible throughout several observational studies of H II regions, planetary nebulae and supernova remnants. It seems possible that the gradient flattens beyond 10–12 kpc (Vilchez & Esteban, 1996), also see Fig. 2.1). The MWG is not the only galaxy with a gradient decreasing with higher distances from the center; in fact most spiral disks for which studies based on optical spectra were carried out, show this characteristic. Fig. 2.1 shows gradients for NGC 628 and M 33 together with the MWG metallicity gradient. The galactocentric distance has been normalized to the respective galaxy's isophotal radius R_0, which is the radial distance from the galactic nucleus at which the declining disk surface brightness reaches 25 mag/arcsec^2; taken from Henry & Worthey (1999).

They summarize some important points: Firstly, characteristic abundances increase with galaxy mass, while gradient slopes are uncorrelated with this parameter; and secondly, characteristic abundances in normal and barred spirals are indistinguishable, but barred spirals appear to have flatter (i.e. less negative) gradients. Additionally, it seems that more luminous galaxies have flatter slopes (Garnett, 1998) when the gradient slope in dex/kpc is plotted versus M_{B}. The mass and characteristic abundance correlation can be seen in Fig. 2.2 with masses taken from rotation curves. The fit is shown as a solid line with $12 + log(O/H) = 3.79 + 0.47 \times log\, M_{\odot}$.

The effects of cluster environment were studied by Skillman et al. (1996). They found that global metal abundances in disks tend to be higher in stripped galaxies. This resulted from the study of several Virgo spirals with H I deficiencies indicating cluster environmental interactions. Their suggestion is, that the reduced

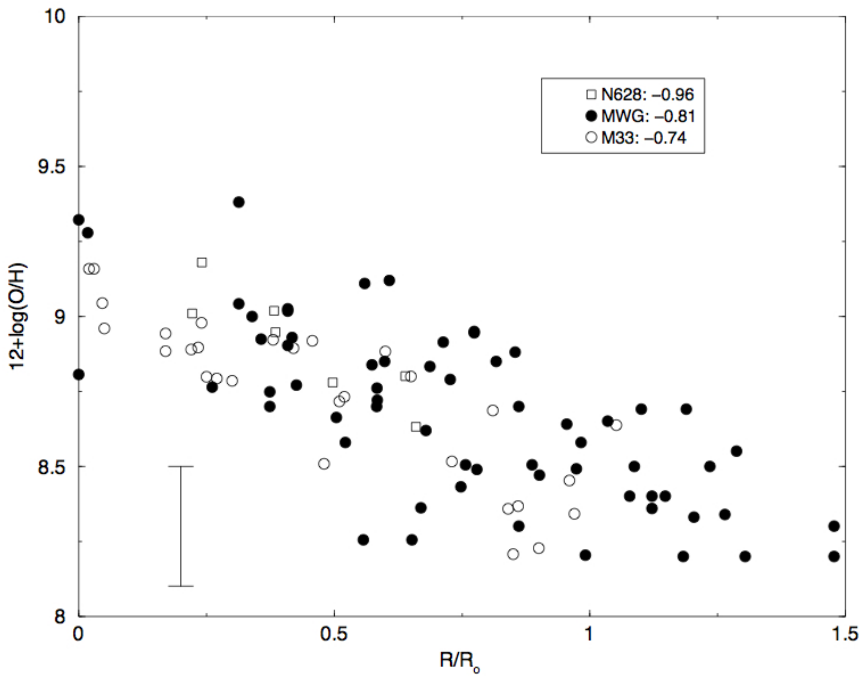

Figure 2.1: 12+log(O/H) versus galactrocentric distance in isophotal radius for the Milky Way (filled circles), M 33 (open circles), and NGC 628 (open squares). Results for NGC 628 and M33 taken from Zaritsky et al. (1994), with Milky Way data from Shaver et al. (1983); Afflerbach et al. (1997); Vilchez & Esteban (1996).

infall of metal-poor H I gas yields less dilution of disk material. This assumption was opposed by Henry et al. (1996) who found no environmental effects while investigating metallicities and heavy element abundance ratios ($N/O, S/O$) in three cluster spiral disks with normal H I, concluding that cluster environment alone is less likely to alter the chemical evolution.

Measurements for abundance profile patterns for spheroidal systems, especially elliptical galaxies, involve the use of photometric indices of integrated starlight. Henry & Worthey (1999) summarize this as taking the colors and absorption feature strengths as a function of galactocentric radius, which are interpreted through population models.

Local abundances in all kinds of galaxies can fluctuate quite a lot due to cloud

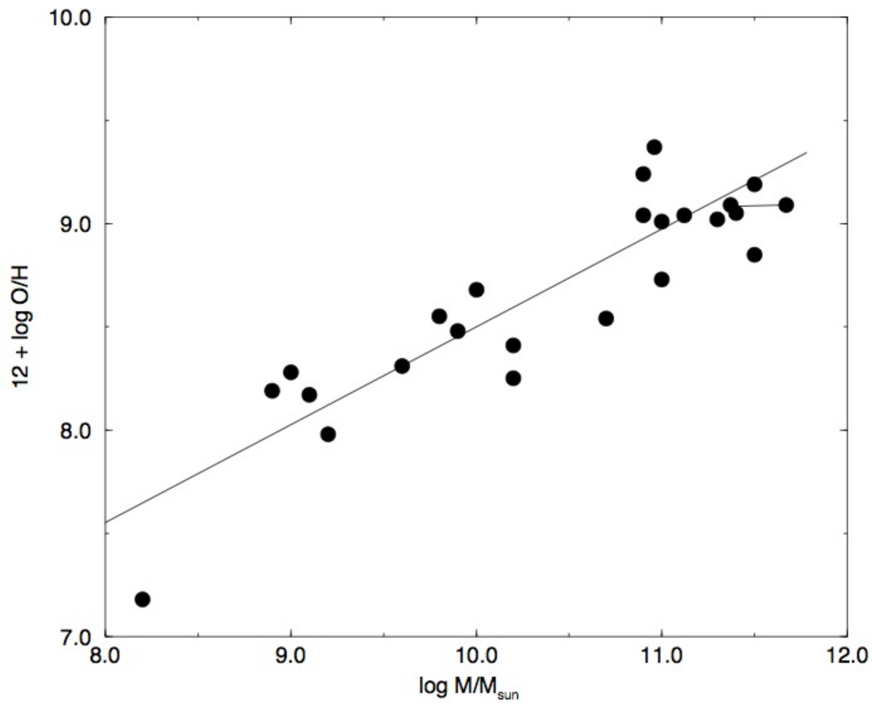

Figure 2.2: Oxygen abundance at one effective radius expressed as 12+log(O/H) versus log galaxy mass in solar units for a small sample of spirals. Abundance data are from Garnett & Shields (1987); Skillman et al. (1996); Henry et al. (1996). The two points connected are from NGC 753 whose mass was determined for H_0 = values of 50 and 100 km/s.Taken from Henry & Worthey (1999)

collisions, star formation driven flows, and differential rotation that mixes the gas, as well as turbulence in the ionized regions at the smallest scales. Mergers and interactions, as well as accretion, without doubt influence the evolution of galaxies. How exactly this influences the chemical evolution of galaxies is still unanswered. Nevertheless, it is now widely accepted to assume the presence of radial abundance gradients with O/H in H II regions decreasing outwards in a galaxy. From studies of $H\beta$ equivalent widths and models of H II regions, it is also clear that this inward increase is linked to a softening of the ionizing stellar spectrum, implying either a decreasing mean effective temperateure or increasing dustiness (Pagel et al., 1979).

The main issues in AGN research persevere: explaining the origin of the gas that fuels the nuclear black hole, as well as the mechanisms responsible for the angular momentum loss that is needed for the movement of the gas. Additionally, it is unknown how this accretion of gas and constant internal change influences the interior chemical evolution of the AGN and host galaxy. Assuming that galaxy-galaxy interactions are responsible for triggering AGNs and furthermore assuming that lower metallicities are found towards the outskirts of galaxies, one can follow that an inflow of gas due to mergers could result in decreasing or flattening metallicity gradients, in comparison to increasing gradients in field galaxies without such interactions. This has been investigated theoretically in D. Rupke, L. Kewley and J. Barnes' recent work (Rupke et al., 2010b,a), which shall be introduced in the following.
Comparisons of interacting galaxies to the mass-metallicity relation result in lower nuclear oxygen abundances compared to abundances observed in field galaxies. Rupke et al. (2010b) present N-body/SPH numerical simulations confirming the hypothesis that these underabundances are generated through inflows of low-metallicity gas from the outskirts of the two merging galaxies. This flattening of the metallicity gradients arises shortly after first passage due to radial mixing of the gas. The chemical evolution of interacting galaxies is far more complex and puzzling than in isolated systems due to this mixing of the gas. The mass-metallicity relation of galaxies (Lequeux et al., 1979) predicts that low-mass galaxies contain fewer heavy elements than high-mass galaxies. The reason for that is a combination of different star formation histories and gas inflows and outflows. In general, star formation, also induced by interactions of two or more galaxies, and stellar evolution – through stellar winds and supernovae – always enrich the interstellar medium, while the gas in- and outflows redistribute the heavy elements internally. The lower metallicities in the inside of the interacting galaxy (Kewley et al., 2006a) can therefore be accounted for by

1. inflows of relatively metal-poor gas from the outskirts of the galaxy into the high-metallicity center (Mihos & Hernquist, 1996; Barnes & Hernquist, 1996),

2. outflows of recently produced metals that prevent further enrichment (Edmunds, 1990; Dalcanton, 2007).

The proposed model for spiral galaxies (one or both) can therefore be summarized as follows: radial abundance gradients in the merging galaxies show lower

abundances at larger galactocentric radii. This results in lower average abundances produced by the redistribution of the gas which can be seen in the gas metallicity profile across the entire disk. Similar flatter gradients can be seen in barred spirals with an internal redistribution of gas due to the bar-induced gas motions (Vila-Costas & Edmunds, 1992), with even lower central metallicities than interacting galaxies (Dutil & Roy, 1999).
Rupke et al. (2010b) present eight N-body/SPH simulations of close-passage, equal-mass disk galaxy mergers. Their galaxies were modeled with 87040 particles each and gas mass fractions of 12.5 %. The gas- and star distribution was modeled to be an exponential disk with constant scale height equal to 6 % of the disk scale length and a cuspy stellar bulge with a mass 1/3 of the stellar disk. Metallicities were assigned to the gas particles at the beginning using the average gradient measured by Zaritsky et al. (1994),$-0.2\,\mathrm{dex/R_d}$ with $R_\mathrm{d} \sim 3\,\mathrm{kpc}$, and then fixed and followed with time. The results of strong interactions between two present-day spirals of roughly equal mass can be seen in Fig. 2.3.

The metallicity does not change before first pericenter, but can be seen dropping drastically after first passage. Rupke et al. (2010b) describe the change in nuclear metallicity in Fig. 2.4.

Finally, Fig. 2.5 shows the radial metallicity profile versus time. The initial distribution shows a steep slope while the metallicities after first pericenter exhibit a much shallower slope indicating the evolution towards a flatter distribution. The profile even tends towards a steeper negative slope in the innermost regions (Rupke et al., 2010b). It can also be seen that at late times and large radii when tidal structures form, the more dramatic change in dispersion of the metallicity particles results in a more serrated line. The increase in metallically beyond $R \sim 3\,R_\mathrm{d}$ is explained by Rupke et al. (2010b) through tidal tails spinning out from the interiors of the progenitor disks carrying metal-rich gas into the outskirts. In spite of everything, this effect is explained to be much smaller compared to the effect of radial inflow, considering the gas mass involved.

On a final note one needs to add that a study of weakly interacting spirals did not find this trend in metallicity gradients (Márquez et al., 2003).
This work was done in the light of finding more observational evidence that interactions redistribute metals internally from which changing metallicity gradients result. These effects could cause changes in interpretation of mass-metallicity relations. While Rupke et al. (2010b)'s theoretical simulations first showed how interactions influence the galaxies' metallicity gradients in such a way, large sur-

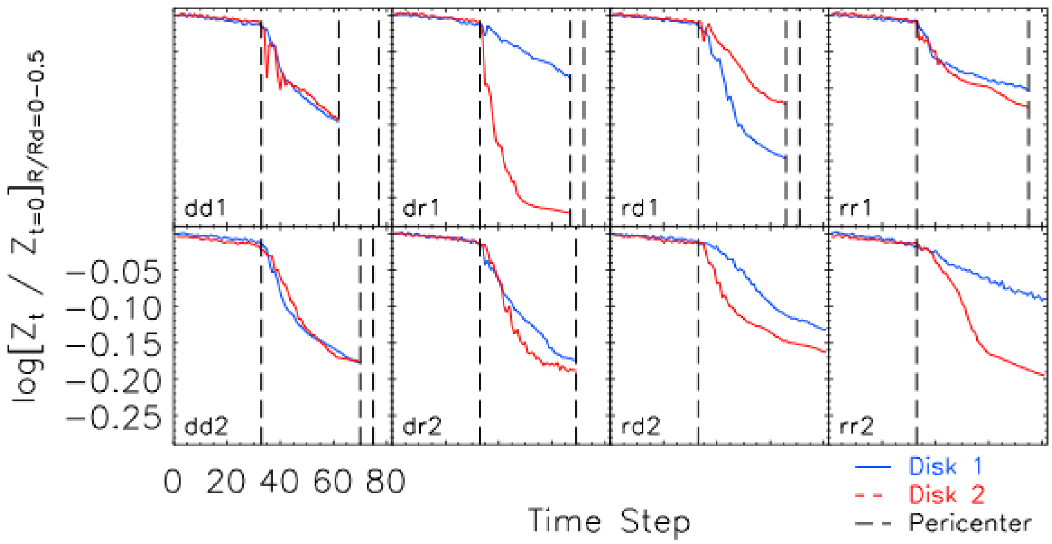

Figure 2.3: Change in nuclear ($R/Rd < 0.5$) metallicity as a function of time. The metallicity is expressed in terms of Z, the mass ratio of an element to that of hydrogen. Strong evolution is observed between first and second pericenter, of typical magnitude 0.2 dex. Vertical dashed lines locate the time of each pericenter. Data courtesy: Rupke et al. (2010b).

veys now enable access to detailed line diagnostics which yield to information of fundamental physical properties, such as SFR, metallicities and nuclear activity. Combining these with stellar evolution and photoionization models, the community will be able to present wide ranging statistics for a large number of galaxies. The following presents a somewhat closer look at an individual, close by galaxy and a comparison with another. Though the effect would be more significant in galaxies at higher z where interactions and mergers were more likely to have happened, it is more practical for a first closer look to choose a galaxy that is close by.

The following work involves the analysis of the nearby Seyfert 1.5 galaxy at z<0.01 observed with VIMOS in 2004 with the integralfield unit. Key aims of this work include an investigation of the galaxies' kinematics and to look for accretion signatures. The visual galaxy pair UGC 1935 (Mrk 1040) and LEDA 212995 will

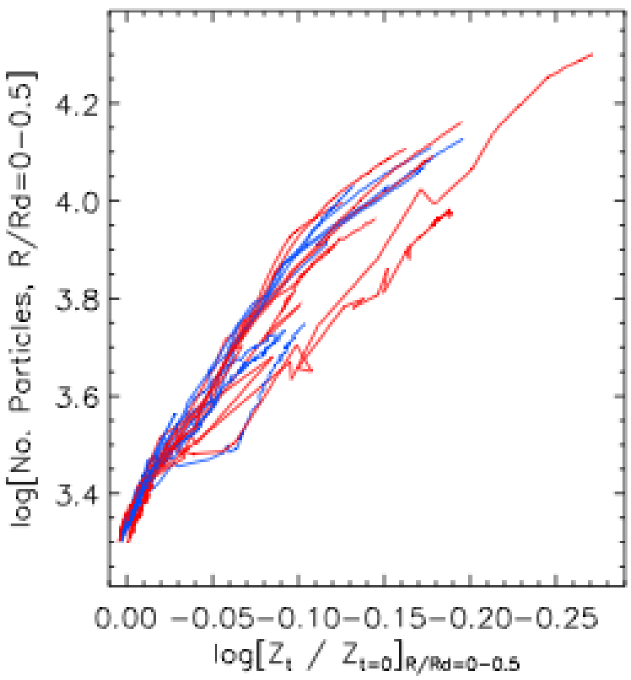

Figure 2.4: Change in nuclear metallicity vs. number of gas particles within the same radius. Blue track represent the time evolution of disk 1, red tracks of disk 2 for each simulation, from lower left to upper right. The strong correlation demonstrates that the underabundance is caused by gas inflow. Data courtesy: Rupke et al. (2010b).

here be investigated in more detail. By using three dimensional information given with the extensive number of spectra provided by the instrument, a kinematic map of the galaxies can show the internal dynamics and show in- or outflows. A rotation curve can yield further information about the internal structure of the galaxies and emission line ratios give insights into the ionization processes of the active galaxies. The galaxy was chosen to be an active galaxy in interaction with another galaxy. UGC 1935 was confirmed to be tidally interrupted in HI while interacting with LEDA 212995, the galaxy's satellite, by Kuo et al. (2008). The comparing Seyfert 2 galaxy, Mrk 607 is part of a group but their interactions with each other are either too minor to show changes in gradients or non existent.

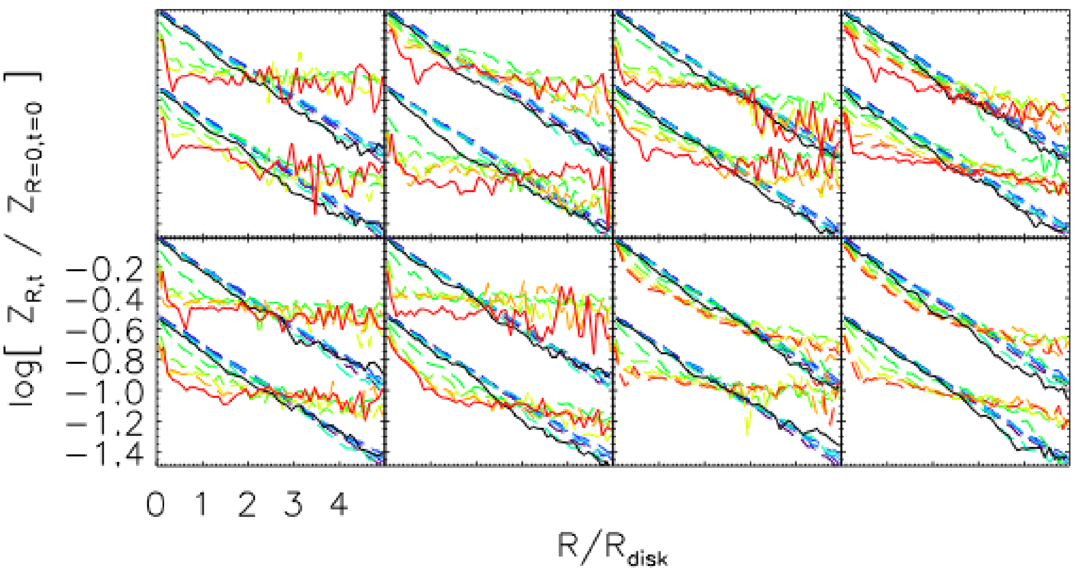

Figure 2.5: Radial metallicity profile at up to 10 time steps prior to second pericenter or the end of the simulation, whichever comes first. Blue dashed lines indicate early times. Orange dashed lines late times. The profile at first pericenter is shown as black solid line, the profile at second pericenter as a red solid line with the profile for disk 2 being offset by $-0.5dex$. Data courtesy: Rupke et al. (2010b).

3 Observations

3.1 Integralfield Spectroscopy

With the introduction of integralfield spectroscopy to the world of science, a giant leap was made towards optimizing observational astronomy. Before IFS, long-slit spectrographs were able to produce merely a few tens of spectra per observation night; now integralfield-units (IFUs) such as VIMOS at the VLT, allow working with several thousands of spectra per frame. The number of spectra detected by the instrument depends on the amount of spatial resolution elements scanning the - usually large - field of view. The result of this particular kind of 3D spectroscopy is a data cube containing information about (α, δ) and λ. The term 3D spectroscopy more generally speaking refers to the technique of producing spatially-resolved spectra over a two dimensional field, whereas IFUs in particular produce all the data for an exposure of one pointing simultaneously resulting in a 3D data cube of a scalar related to flux density as a function of the spatial coordinates in the field and wavelength (Allington-Smith, 2006). IFUs are micro-lenses coupled to fibers, which are roped up in bundles. Just like in a regular spectrograph, the light passes through a set of long slits at the entrance of the spectrograph (here produced by the micro-lenses) through a dispersing element (a grism) before the spatial sampling and spectra produce the end result. This way the two-dimensional field of view at the entrance of the telescope is transformed into a three dimensional data cube (Zanichelli et al., 2005). IFS is without doubt the future of spectroscopy and has many advantages compared to (long-)slit spectroscopy. It is more reliable for studies of complex shapes or closely packed regions such as AGNs, star forming regions in galaxies, mergers, central regions, galaxy clusters amongst many others, which makes it a powerful tool in modern extragalactics. It collects all information of the emitted light of extended regions in one observation and slit losses are no longer a problem to be considered. Also the pointings are made easier as accurate target acquisitions are no longer needed. Positioning and mosaicing can be done with the data after the

observations. Errors occurring due to frailties in slit technology, like inaccurate radial velocities or atmospheric dispersion effects can be eliminated or corrected. IFS has also advantages in poor seeing conditions: IFS is optimally matched to the object PSF (Allington-Smith, 2007). The micro-lens array at the telescopes focal plane consists of thousands of lenses allowing continuous space coverage; but since the fibers are bundled up closely at the slit, a small spectrograph faces problems of contamination. The reduction of the data has to deal with disentangling the signals of the neighboring fibers. This is one reason why the calibration and reduction processes are more complicated than with regular spectroscopy. Despite these complications, IFUs are the best tools to extract sources in crowded regions or overlapping geometries. Maps of physical quantities like velocity, stellar population, age and molecular gas distribution can be obtained and regions with different physical states can be unraveled (Emsellem, 2007).
The idea of combining imaging and spectroscopy which would provide 3D information is not new, but since detectors have two dimension a solution for storing three dimensional information had to be found. The logical solution of scanning the object by taking a series of exposures with the slit is time-consuming and foundation for unavoidable errors because with every successive exposure, different instrumental and atmospheric conditions due to the elapsed time are used. Modern IFSs precursors are Fabry-Perot Interferometry, FPI, and imaging Fourier transform spectroscopy, IFTS, (basically a Michelson interferometer with a moveable mirror) that use time-domain measurements of the radiation. An IFTS takes a long time to scan through the spectrum, but produces a large number of spatial samples (spaxels) where one would have to mosaic different pointings in IFS. (Allington-Smith, 2006). Fabry-Perot interferometry uses narrow band images. The spectral coordinates are scanned in many exposures using a filter adjustable in the wavelength. Even though these older techniques were too time-consuming with having to scan the object spatially or spectrally, they introduced the concept of data cubes. As early as 1974 the Fabry-Perot technique was combined with direct imaging detectors. But all these first attempts are more sensitive to changes in the instrumental or sky background, which are natural observing conditions and therefore have to be considered. Radio astronomers were making 3D spectral imaging observations long before it was thought of in optical wavelengths, but the technique of obtaining full two-dimensional coverage in a single exposure even if the field of view is aligned to the size of the instrument and therefore limited, has proven itself to be of high importance. The advantage of being able to record

many spectra from extended objects at the same time without assembling them afterwards and thus risking gaps has become obvious in the early 90s. The development of a way of storing the 3D information, the (x, y, λ) function or data-cube, on a 2D detector overcame many of the problems older techniques had. All 3D spectrographs have in common that the image is split into elements in the focal plane using a fiber matrix and subsequently redistributed in a new arrangement at the entrance of the focal plane. This general alignment forms a pseudo-slit at the entrance of the spectrograph (see next part for more details). Another advantage besides the obvious efficiency and homogeneity due to the single exposure is, that it becomes obsolete to center the slit onto the object. Seeing doesn't play a major role in observations with IFS any more since the spectral resolution is defined by the size of the fibers on the detector. The spectra can also be corrected for the differential atmospheric refraction. Testing for IFS started in the 1980s on the CFHT (Canada France Hawaii Telescope) by Vanderriest with the outcome of new techniques for the fiber-optics instrument SILFID associated to the CFHT (Vanderriest, 1998) or HEXAFLEX at the William Herschel Telescope (Arribas et al., 1991). First conferences were held in 1994 and first studies with IFS like TIGER (e.g. Bacon, 1995), INTEGRAL (Arribas et al., 1998), which opened IFS to the scientific community and SAURON (e.g. Bacon et al., 2001) were conducted. These early devices, built by groups in France and Germany, showed first extraordinary results on faint galaxies and other distant extended objects. Many instruments have been successfully completed and observatories not only in Europe (first and foremost ESOs VIMOS and SINFONI integralfield spectrographs), but also in the Americas, Australia (Two Degree Field at the Anglo-Australian Telescope) and Japan. It is beyond question that integralfield spectroscopy is the future of spectroscopy and that most observatories want to be equipped with such an instrument. The first true integralfield spectrographs used optical fiber bundles, but there are other techniques two-dimensional spectroscopic observations can use besides fibers: microlenses and micromirrors or a mixture of the above. The idea of using lens-arrays reaches back as far as the 1960s even though the methods have been optimized. Image slicers where mirrors are arranged to deconstructs the image at the focal plane to later create the slit of the spectrograph with the slices laid out end to end.
In summary there are three main techniques in integralfield spectroscopy (Allington-Smith & Content, 1998):

Lenslet arrays where the input image is formed at the input surface of a microlens array (MLA). The small images of the telescope pupil form a dot and are distributed by the spectrograph. The MLA can be tilted so that spectra spread out and don't overlay. Spectral resolution and throughput can be optimized, but the spectrum's length is very small.

Fiber bundles where the image is formed at the entrance to a bundle of fibers. Spectra do not have any wavelength shifts between them, but there are gaps visible between the fiber cores.

Image slicers where the image is cut into thin horizontal sections, which are sent in different directions. A second mirror reformats the slices to form the slit of the spectrograph. Image slicers are difficult to fabricate, but Focal Ratio Degradation can be avoided completely which can be a problem in the above mentioned techniques.

3.2 Instrumentation

3.2.1 VIMOS

VIMOS is the Visible Multi-Object Spectrograph for the Very Large Telescoope (VLT) of the European Southern Observatory (ESO). It was installed on the third 8.2 m - unit (UT) of the VLT on Paranal, Chile and is thus the largest IFS built on an 8m class telescope so far. Each UT is equipped with a Cassegrain and two Nasmyth foci as well as a Coud*é* focus station for interferometry. VIMOS operates on UT3s Nasmyth B focus (a circle with $22'$ on the sky corresponding to a large linear scale of almost 1 m) and observes in wavelengths ranging from $0.37 - 1\,\mu$m. Because it was designed to carry out surveys, VIMOS is able to sample a large field of $54'' \times 54''$ (in low resolution) with 6400 optical fibers coupled to microlenses simultaneously. The optical path is split into four channels to allow the large sky coverage. These four quadrants (each $7' \times 8'$, arranged in a 2×2 field with a $2'$ wide gap between them) each act as a classical focal reducer imaging spectrograph with a collimator, a parallel beam where the dispersive element is inserted and a camera that focuses the beam onto a 2048×4096 EEV CCD where each pixel measures $15 \times 15\,\mu m^2$. They are operated in parallel, which means that

it is not possible to use different settings (like modes or grisms) on each of the quadrants.
The instrument can operate in three different modes: imaging (IMG), multi-slit spectroscopy (MOS) and integralfield spectroscopy (IFS). The IMG mode uses broadband filters UBVRIz. MOS and IFU modes share the four optical channels and can be used with a variety of filters and grisms (See Table 3.1).
The optical path in IFU mode can be described as follows: the focal plane (divided into the four channels) is equipped with the IFU fiber-head, the fiber bundles, and the IFU masks. The focal plane is flattened by a field lens at the instruments entrance to guarantee flat multislit masks. Folding mirrors and flexure compensators are inserted into the collimator to fold the beam and to reduce the size of the instrument. The image stability is guaranteed by the flexure compensation mechanism, which limits the effect of flexure to an image motion of less than ± 2 pixels on the CCD. Because of the thinned, back-illuminated CCDs used in VIMOS, fringing effects, which are visible especially above $8500\mathring{A}$, are removed. The beam section contains optical analyzers (filters and/or grisms), the camera and the exposure shutter lie in front of the CCD. The filter exchange units (FEU) host 10 filters permanently mounted, the grism exchange units (GEU) hosts six grisms at all times (see Fig. 3.1). The six grisms provide a range of spectral resolution from R $\sim$ 200 to 2500.

Table 3.1: Integralfield Unit: Grism characteristics

Grism	Spectral range	Spectral resolution	Dispersion ($\AA$/pixel)	Field of View	Spatial resolution (arcsec/fiber)	Spatial elements	Spectral elements (pixel)
LR blue	400-670 nm	220	5.3	$54'' \times 54''$ $27'' \times 27''$	0.67 0.33	6400 1600	600
LR red	590-915 nm	260	7.3	$54'' \times 54''$ $27'' \times 27''$	0.67 0.33	6400 1600	600
MR	490-1015	720	2.5	$27'' \times 27''$ $13'' \times 13''$	0.67 0.33	1600 1600	?
HR blue	415-620	2550	0.51	$27'' \times 27''$ $13'' \times 13''$	0.67 0.33	1600 1600	4096
HR organge	525-740	2650	0.6	$27'' \times 27''$ $13'' \times 13''$	0.67 0.33	1600 1600	4096
HR red	645-870	3100	0.6	$27'' \times 27''$ $13'' \times 13''$	0.67 0.33	1600 1600	4096

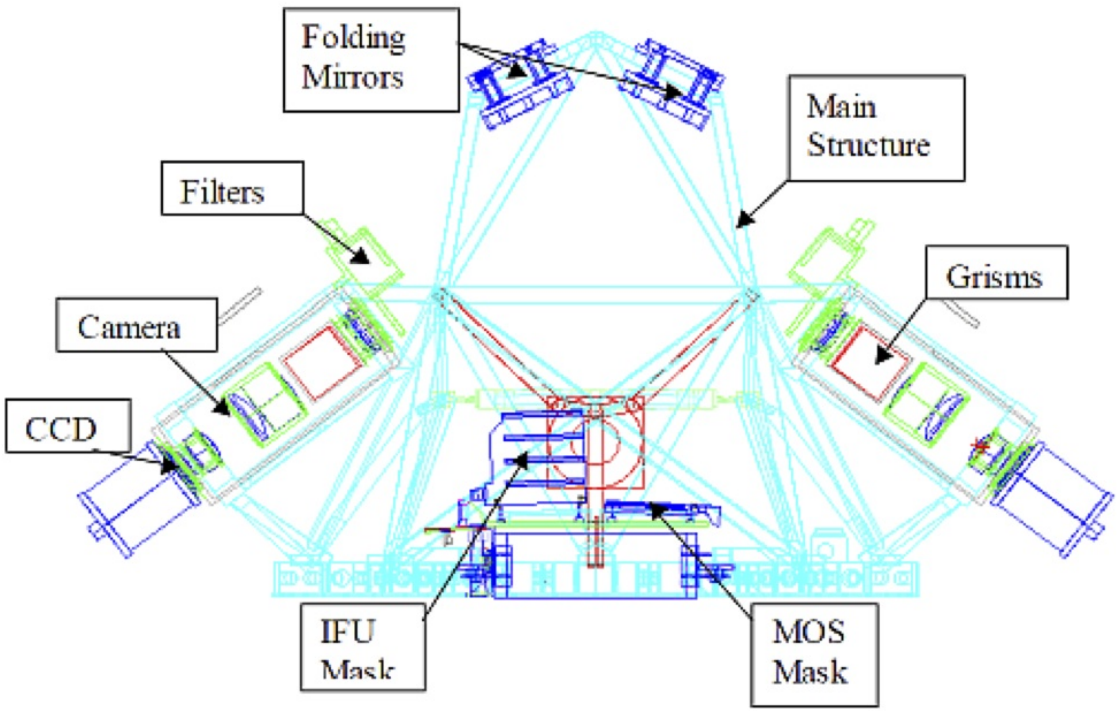

Figure 3.1: VIMOS Opto-Mechanical layout

The IFU head, located at one side of the instruments focal plane, collects the light. It consists of 6400 2D input micro-lenses (organized in an 80 x 80 array), each coupled to an optical fiber. The fiber-bundle connect the IFU head to the four IFU masks, special support structures, which are placed in the instrument focal plane during IFU mode act as the optical link between the micro-lens array and the VIMOS focal plane. The output of the fibers on the mask is re-arranged in a linear way to form pseudo-slits, that act as an entrance slit to the spectrograph. Each of the four masks is associated with a 1600 fiber-bundle. Each quadrant feeds a set of four pseudo-slits, for a total of 6400 fibers. These sub-bundels are again divided into five modules of 80 fibers each (see Fig. 3.2). This rather complicated configuration ensures the small field losses of 5 %.

The f/15 focal ratio is restored by the micro-lenses on the pseudo-slits.Their positions are fixed on the IFU masks and therefore also the geometry of the spectra on the four CCDs.The agreement of the positions of a fiber in the IFU head and the position of its spectrum on the detector is crucial for the reduction (Zanichelli

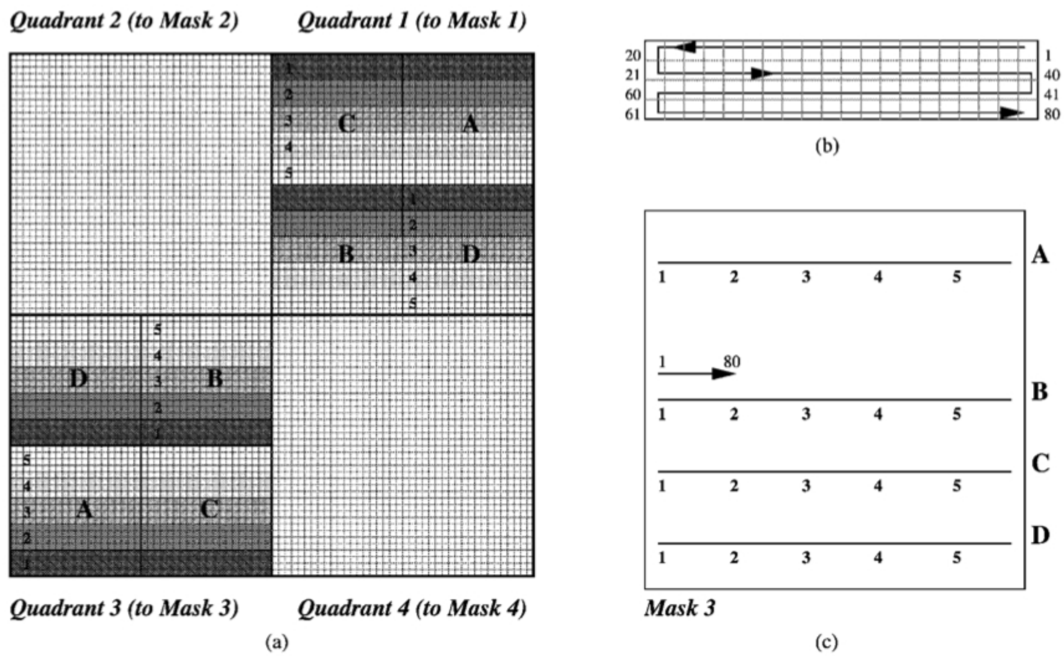

Figure 3.2: Layout of the IFU as taken from Zanichelli et al., 2005. (a) graphically shows the 6400 fibers arranged in 80×80 micro-lenses arrays for each quadrant of the IFU head. The four VIMOS sub-bundles of each quadrant, which feed the pseudo-slits are marked A, B, C, D for Quadrant 1 and 3. Each sub-bundle is divided into 5 modules of 80 fibers. (b) shows how the fibers are arranged along the fiber module which are then organized over the pseudo-slits as shown in (c).

et al., 2005; Scodeggio et al., 2005). A contiguous area of up to $54'' \times 54''$ in low resolution spectroscopy can be reproduced with the option of two spatial samplings (magnifications) thanks to a removable focal elongator: 0.33"/fiber or 0.67"/fiber. The use of intermediate and high spectral resolution grisms result in a smaller field of view where only 1/4th of the field is used. A masking-shutter (IFU shutter) is placed in front of the micro-lens array that is not in use. To determine the sky area available for IFU observations is therefore a result of the chosen spectral and spatial samplings. At low spectral resolution (R $\sim$ 200) an exposure produces 6400 horizontally stacked spectra (4×400 on each of the VIMOS CCDs). At high resolution (R $\sim$ 2500), the spectra comprise more pixels in the wavelength direction over the CCDs and only the central pseudo-slit on each mask (the central part of the FoV) can be used (Zanichelli et al., 2005). In LR spectroscopy, it is possible to use the IFU Shutter: if only a part of the FoV is interesting to the observer because of the objects limited size, it is possible to mask the outer parts of the IFU, just as in HR and MR modes.
The spectral resolution is determined by the combination grism and the fiber size (FWHM is about 3.2 pixels, corresponding to $0.67''$). The spacing between the fibers on the detector measures 5 pixels, which corresponds to $1''$ on the sky. The spectral characteristics for different combinations of grism and filter are given in table 3.1 (taken from the VIMOS User Manual). The four shutters are responsible for illuminating the CCD properly for exposure times as short as 1 sec. A QTH50 halogen lamp provides flatfields for the correction of pixel to pixel variations in IFU mode. They illuminate a calibration screen at the back of the Nasmyth shutter, as well as He, Ar and Ne arc lamps, to perform flat and arc calibration exposures.In IFU mode accuracy of the telescope pointing is $\sim3''$. The possibility of using dithering/jitter patterns where different pointings around a central position are added up to reconstruct a combined image holds several advantages: the diminishment of the sky contribution, cosmic rays, CCD fringing, and cosmic defects on the detectors. It furthermore allows very accurate flat fielding (for HR grisms three screen-flats are mandatory, for other cases the number is optional). In order to minimize effects like flatfield residuals and wavelength calibration offsets (due to instrumental flexures that occur if they are taken at a very different rotation angle to the science data), nighttime screen-flats and arc calibrations are mandatory for all IFU settings.
The orientation of the square geometry of the IFU on the sky can be understood as follows: the sides are oriented N-S and E-W where North is up and East to the

right when the rotation angle is zero.
ESO has currently two other VLT instruments operating in IFU mode: FLAMES/GIRAFFE mounted on UT2 and SINFONI on UT4 which is fed by an adaptive optics module. GIRAFFE is a medium to high-resolution optical spectrograph with two IFU modes: one mode with 15 IFUs of 20 × 20 micro-lenses each and a mode with a single 22 × 14 array of micro-lenses (Argus). Every IFU has a FoV of $3'' \times 2''$. Both the IFU and the Argus mode use a total of 300 object fibers, 15 sky fibers and 5 arc fibers. SINFONI is dedicated to near-infrared observations (it observes in the 1.1 – 2.45 μm range) with a 32-element image slicer to map 64 × 32 spaxels onto one pseudo-longslit.

4 The Data Reduction

4.1 Overview of reduction steps for IFU data

The general steps that need to be undertaken when reducing a set of data includes the basic reduction of the science frames provided by the observatory, the ESO archive (`http://archive.eso.org/cms/eso-data`) in my case. For this a set of calibration frames observed with the same instrument setting at or around the same night (depending on the type of calibration) is used. This insures that the calibraton is observed through similar atmospheric conditions with equal setups. The basic reduction performed for IFS calibration includes the following steps:

Bias subtraction Creation of a master bias and subtraction of the same

Flatfielding Creation of a master lampflat

Cosmic Ray cleaning Removal of Cosmic Rays saturating multiple pixels

Spectra Location Identification and Tracing of Spectra

Spectra Extraction

Wavelength Calibration

Sky Subtraction

Flux Calibration Standard Stars, reduced the same way as the science frame

Data cube correction Stacking of individual frames

The bias correction ensures that pixels that show a numerical offset, and slightly differ from one another, are corrected for. The differences can be explained as follows: The signal which is given out by the charge couple device detector consists of the photons from the object, converted due to the photoelectric effect into electrons which are further converted into digital signal. In addition, a dark current

which is the result of the thermal excitement and the fact that we observe in a heated environment, as well as the bias, the offset signal which is created during the read out of the information, are added onto the output and need to be removed. The bias frame is a zero-second exposure with the shutter closed. The bias frame is usually quite stable, can therefore be taken at the beginning or towards the end of the night (adding up to $\sim$200 ADUs), usually whole sequences of these exposures are stored and combined resulting in a master bias frame, finally subtracted from the science frames. For the VIMOS IFU data, a series of five bias frames were taken for each CCD (each quadrant), adding up to 20 bias frames for each observing night. The combination of the bias frames resulting in the master bias used the median, pixel by pixel, of the individual frames for each quadrant.
The dark current, the thermal excitation of electrons in the semiconductors, corrected for by the dark frames, are standard calibration frames in photometry. They correct for the thermal movement of the charge carrier compared to the photons into the camera. This is negligible for well cooled cameras and is almost identical to the bias. Modern astronomical cameras are cooled with liquid nitrogen, so that the noise from dark current is not significantly detected and can be relinquished for the VIMOS observations.
The flatfield calibration varies from photometry to spectroscopy. In photometry, this is the observation of an evenly illuminated area like the inside of the dome or the twilight sky. Ideally, all pixels are equal, but in reality, some pixels or whole rows of pixels are dead, show no signal. Uneven illumination of the field can result in darker edges, striae or dust doughnuts. To account for this, flatfield frames are taken, combined and subtracted. For the VIMOS IFU setup, a number of continuum lamp exposures are taken after the science frames, three for each quadrant of $\sim$10 sec each. The lamp frame exposures are therefore taken with the same setup as the science frames. These are later added up (stacked and combined) to create the master lampflats, again using the median of each pixel. These are subtracted individually for each quadrant of the CCD guaranteeing a smooth fiber profile in dispersion and cross dispersion direction.
Another important step is the correction for cosmics. Cosmic rays are highly energetic charged particles that constantly hit the CCD causing high signal artefacts. Usually the pipelines or reduction software uses an algorithm that rejects all outliers, obviously high signal above a certain threshold. This check is essential for the work with emission lines since emission lines on raw IFS data can easily be confused with CRs which are small, round, and sharp. The trick is to

remove enough cosmic rays but without removing real features. When working with multiple exposures of the same object, an image comparison technique can be applied, where the individual images are compared to a median of all images. Since this was not the case for the used sample, this method was not exerted.
The basic calibration frames should include a sufficient number of bias frames, flat-fields (lamp/dome, and/or twilight) as well as arc frames when dealing with spectroscopic data to ensure the wavelength calibration. In addition, dark frames, observations of a standard star for flux calibrations as well as a telluric standard for sky line subtractions and radial velocity standard sources for the determination of the zeropoint ZP when radial velocity measurements are the goal can be used for further calibrations. Twilight flats are taken to correct for fiber-fiber throughput differences.
Depending on the wavelength and observation mode, the sky can be a significant problem that needs to be considered. If removing the sky background emission is important for the science goal, a set of sky observations might be anticipated.
Most IFSs have a pipeline that helps the astronomer with the reduction of the often wearisome somewhat tedious reduction of hundreds of spectra. Although this is a great help and can not be praised enough, they are very often blackboxes and a thorough insight in the reduction steps is beneficial and often necessary to understand the data itself. Therefore - and because the reduction was a big part of this work - I will go into more detail generally speaking and for the reduction pipeline VIPGI that was written for the VIMOS instrument specifically. A number of sites, papers and books go into the reduction in more detail Westmoquette et al. (for more information visit e.g. 2009a).
The basic steps that include the fibre-fed IFS data reduction are: subtraction of the bias, removing the cosmic ray hits, detection of the spectra on the array of fibers (that combined make out the CCD). This is done by investigating a slice of the flat perpendicular to the dispersion direction which generally exhibits a higher signal to noise ratio, and finding the peaks and tracing the aperture along the dispersion direction. (For more information, see Westmoquette et al. (2009a) and ifs.wikidots.com, from which part of this was extracted). The spectra are then easily found on the other frames once identified on the flat field. The RSS – row stacked spectra – hold the extracted flat-fields, arcs and science spectra (see Fig. 4.1.)

The RSS image shows the extracted spectra from a single raw image stacked on top one another, now only one pixel wide instead of spreading over multiple

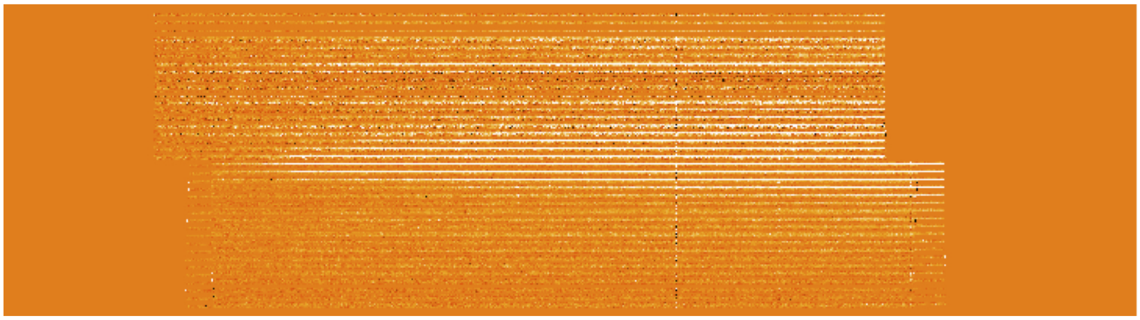

Figure 4.1: Raw stacked spectra (RSS) of the analyzed galaxy UGC 1935.

pixels in the non-dispersion axis. The arc spectra allows to correct for wavelength differences. To correct for fiber-to-fiber throughput differences (spatial and sometimes spectral), twilight frames are used, and subsequently the science and sky frames are divided by these throughput frames. Sky lines on the science frame can be used to correct these again. The sky spectrum needs to be subtracted from the science frame. A flux calibration with a standard star can be applied to the science spectra as well.
VIMOS IFU data calls for special care when dealing with reduction due to the complexity of the data as well as the instrument and the geometrical setup of the data which is automatically put together after the observation.

4.2 VIPGI

A fiber-fed spectrograph differs from a regular spectrograph in that way where the slit is not placed at the focal plane of the telescope, but optical fibers, placed at the focal plane on one end, produce a pseudo-slit on the other end instead. The light is channeled through fiber bundles coupled with arrays of lenses to resolve both spatial dimensions and wavelengths simultaneously. Even though fiber-fed imaging spectrographs are widely used in the scientific community, there are also other techniques to conduct the light from different locations in the sky to the spectrograph. Several instruments, each with slightly different implementation and representation of the spectra at the detectors are in use. This has led to numerous different reduction techniques and packages for each individual instrument (Sánchez, 2006). With these new spectrographs, each producing up to tens of thousands of spectra per night, new reduction pipelines with rigorous data organizers and archives were needed so that the available files and data are not lost among thousands of similar files. On top of that, each instrument as a different data format. General-purpose astronomical software packages like IRAF or MIDAS are not suitable for these tasks and there are no standard software tools for 3D instruments. The European community has reacted and introduced an analyzing tool Euro3D that deals with data from different instruments, but this applies to already reduced data. The heterogeneous collection of instrument-specific data formats and software tools is still a problem. The lack of standards makes it difficult to compare the outputs and the parameters and procedures differ greatly from one pipeline to the next. While this is a problem well known, it has not been solved.

The data for this work has been obtained with VLTs VIMOS instrument, which offers the semi-automated reduction pipeline VIPGI, the Vimos Interactive Pipeline and Graphical Interface (Scodeggio et al., 2005). Among the present day spectrographs, VIMOS is perhaps the most challenging to create a processing tool for (Garilli et al., 2004). Since its an instrument dedicated for surveys, the multiplexing capabilities have been pushed to the maximum and the astronomer has to deal with up to 6400 spectra per exposure.

The development for VIPGI started in 2003 as the result of a contract between the ESO and the VIRMOS consortium to guarantee the independence of already existing software environments and to suit the needs certain peculiarities of the instrument required. The user can furthermore modify the package by adding user defined data reduction, analysis and inspection plugins. The number of calibration and corrections that have to be applied to the spectroscopic data evoked the need to organize the data in logical structures and to insert results in a database. VIPGI was first established for MOS data, but has been extended to the use of IFU data. The driving motor behind the data processing software was the need to reduce the VIMOS VLT Deep Survey (VVDS) data. Today VIPGI is able to handle all available VIMOS data in every mode and instrument configuration. The tasks are grouped in a number of reduction recipes where reduction steps that are normally executed in the same sequence were grouped together into one recipe (e.g. bias subtraction, flat-field correction etc.). This also enables the astronomer to check and adapt the intermediate data-reduction steps. Before the conduction of each recipe, one can modify the input parameters to customize the procedure to the specific needs. Also available are plotting tools to view and analyze the one- and two-dimensional extracted spectra.

The need to organize the large volume of data and to browse the data at any time resulted in the adding of recipes written in the Phython language to the subset of C recipes that automate the task of reducing the data. Python is becoming more and more standard for these kinds of tasks. Evidence for this is PyRAF, the Python based IRAF interface, which has been released not too long ago. VIPGI is composed of ~151,000 lines of C code and 16,000 lines of Python code (Scodeggio et al., 2005).
The reduction pipeline relies on already existing instrument models - one for each quadrant -, which contain the analytical characterizations for the instrument calibration that are used for the spectra extraction. The models comprise the optical distortion model (ODM), the curvature model (CM) and the inverse dispersion solution (IDS), which are all added to the code as polynomial relations. They are used as first guesses which are improved by and by. The ODM links the objects position on the focal plane to the corresponding pixel position on the CCD frame. The curvature models task is to identify the geometrical shape of each spectrum on the CCD. It does so by tracing the spectra along the dispersion direction. The inverse dispersion solution eventually provides the mapping between the position in pixels on the CCD and the wavelength coordinates. The more detailed description, the local model provides information of every fiber, whereas the sturdier global model characterizes a whole CCD frame at once. It is therefore the starting point for each recipe. This global model, obtained by the instrument scientists with special calibration masks, is further refined first to get the local models and later by fitting its parameters to the real data (Scodeggio et al., 2005). Every step in the reduction has to be carried out for each quadrant independently and only in the end, in the data cube, all information is combined.
The important steps for IFU data reduction are the location of the spectra on the CCD, the wavelength calibration with lamp frames and cosmic ray cleaning, cross-talk contamination, sky subtraction, relative transmission correction, and the flux calibration with standard stars. Figure 4.2 shows an overview of various steps of the data reduction.

The instrument model parameters together with the information of IFU fiber end positions stored in calibration tables generate the first guess for the position of the fiber spectrum on the CCD. The checking and adjusting of these first guesses, which are read from the primary header of the FITS file, are important for both spectra location and wavelength calibration. Therefore in several steps the fidelity of these first guesses is gradually improved. This visual crosscheck

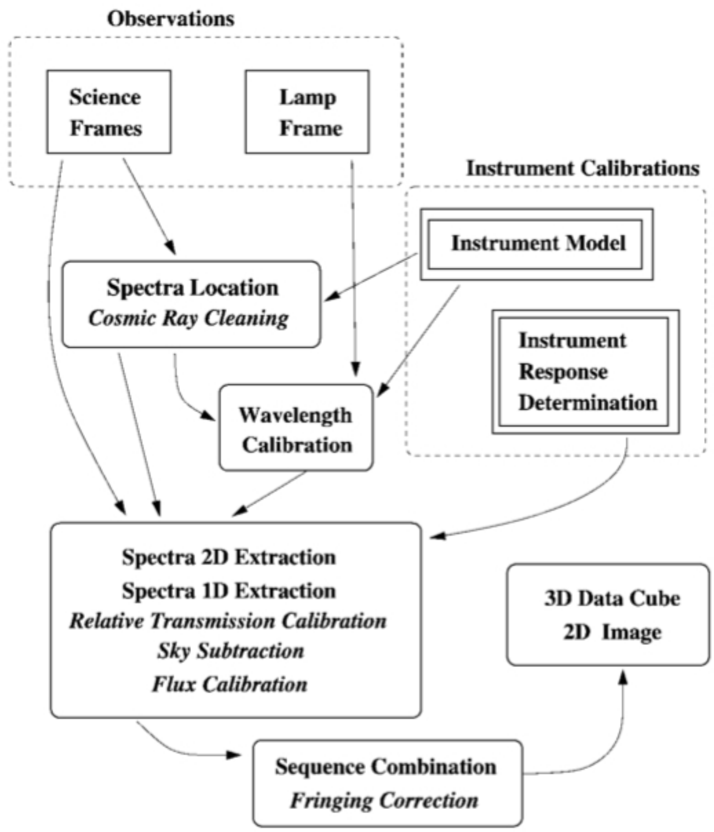

Figure 4.2: Block diagram of the data reduction for IFU data as taken from Zanichelli, 2005. Optional steps are marked italic in grey.

is done manually for each quadrant and is supposed to refine the tracing done automatically where the location of the spectra is found by comparing the intensity at each row along the column (Sánchez, 2006). First, the lamp lines catalog has to be inspected. This is done interactively with the help of a visualization tool like ds9. The catalogue is attached to the data during unpacking depending on the lamps used. The information which lamp was used during the exposure VIPGI reads from the arc observations header. Also standard line catalogues can be used, differing only for different resolutions. The overlay of lines (green) is placed on top of the image, matching the centers of the lamp lines (see Fig. 4.3).

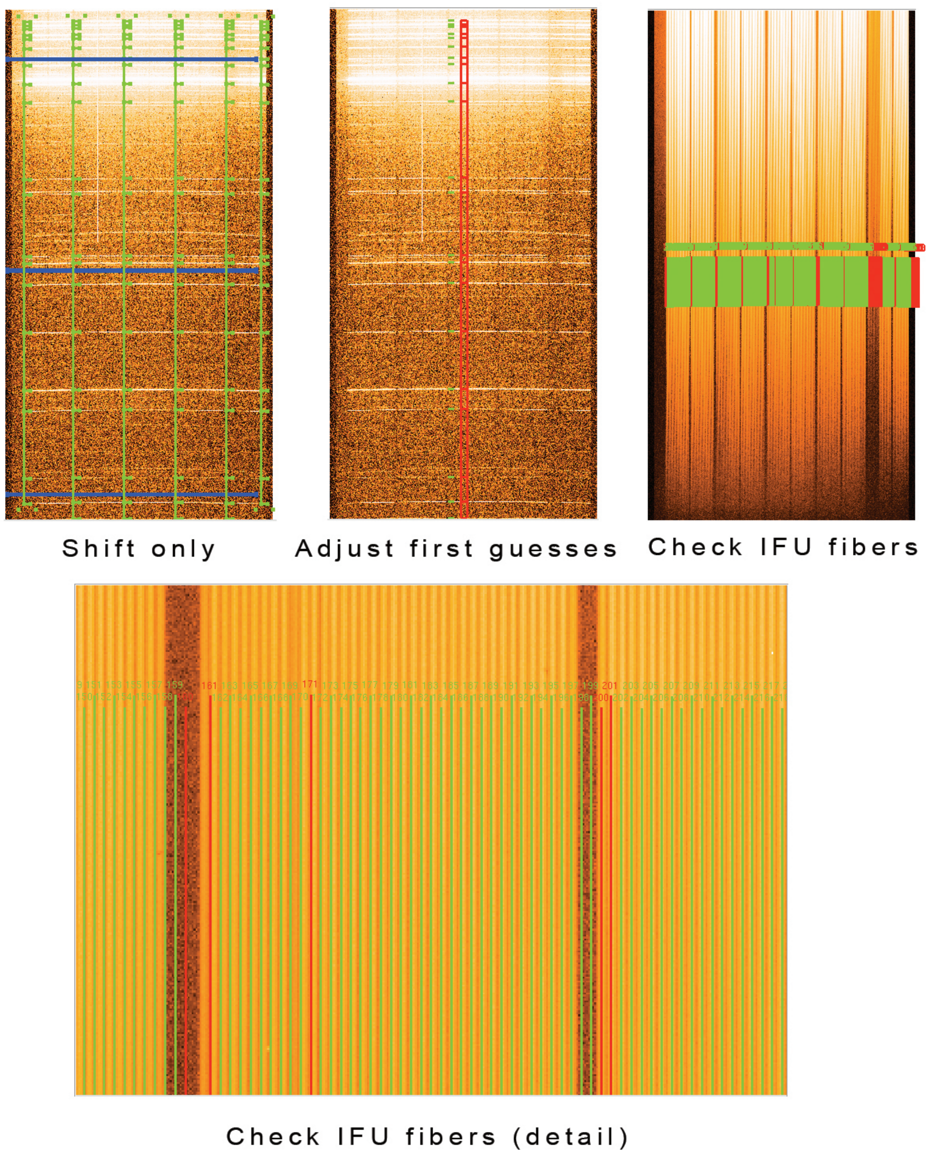

Figure 4.3: Examples for shifting of the green lines of the computed first guesses to fit the spectra (top left) and adjusting the lines with the lamp spectra (top middle). The fibers need to be checked manually and dead or weak fibers marked (top right and bottom).

Saturated lines can be removed and a new, more appropriate line catalogue for this quadrant is produced. Next the shifts of the first guesses have to be adjusted. The lamp image with a computed flat field or science image is shown in ds9. It is almost always necessary to move the green lines to match the position of the arc lines and to verify the position of the gap between the modules. The ∼10 signal free pixels between modules are visible on the screen (see top left image in Fig. 4.3). The next step is to choose the lines used in the program. Again the lamp image will be displayed superimposed with green lines computed from the flat or science image and the user can delete lines not needed for a first adjustment. About 6 lines that well represent the image (not to faint, not to bright, well spaced) should be left for further investigation. To complete the adjustment again the lamp image will be displayed with some regions overlaid. The chosen superimposed green lines have to be moved to the center of the real arc lines. The refinement is recomputed and a new first guess for the dispersion solution is evaluated. Lastly the IFU fibers have to be checked. By inspecting the fibers carefully, dead fibers or lost spectra due to low contrasts between the pixels can be identified and marked as broken. The transition of the fibers can get very low with time. Also the fibers can be partially covered by the IFU shutter in high-resolution mode. All fibers showing a lower transition level should be flagged as dead as they will cause problems later on in the reduction if not done so. For my exposures, certain regularities were visible: By checking the geometry of the array and fiber modules it became obvious that the margins of the plane comprising the four quadrants had to be marked as dead. The first two fibers on the left-most and right-most positions could not be used. Over a considerable time span a whole region of fibers was dead, up to 80 fibers in a row. The reasons why this first step of locating the spectra is so critical are mechanical flexures and spectra distribution on the detectors. The flexure is responsible for image motion of the order of $\sim \pm 2$ pixels.

The steps just discussed are time consuming, boring and difficult, but necessary for good results. Often when problems occurred during later stages of the reduction, it was necessary to go back and readjust these first guesses and subsequently redo the following procedures.

Creating the master bias is a matter of a few clicks, where selected and unpacked bias-frames are combined in the reduction recipe. Every recipe can be edited before execution and therefore adjusted to everyones needs. For the bias frames it is important to know that VIPGI creates the spectroscopic master bias in the MOS

subdirectory and puts a symbolic link in the IFU sub-directory.
The master flat is computed with the *Locate Spectra*-recipe which traces the spectra on the CCD. It is more useful to create a master flat this way than to use the real flat field exposure, which turns out to make fringing correction very bad. The real flat field is only to be used with some Filter/Grism combinations for correction of pixel-to-pixel sensitivity variations and mapping the fringe pattern which is a typical characteristic for the VIMOS CCD. The output file, the so-called *Extraction table* is, just as the input files, in the form of FITS files. It contains information of the spectras locations, derived from a halogen lamp flat field. The used parameters for the creation of the master flat are the following:

- Size in pixels of the binning step for IFU tracing: 50
- Use the global fit distrosion model for IFU fiber tracing: NO
- Bad pixel correction on master flat: YES
- Create a mock master flat: YES

The different reduction mid-products are appended as extensions to the files to reduce the overall number of files. To obtain the master flat, the program searches around the – from the first guesses expected – locations of the spectra to find their borders at the grism central wavelength for each slit. The user-friendly graphical interface makes it possible to check most steps performed and to edit the parameter files before launching the recipes. Therefore it is possible to check the reliability of how well the spectra were traced on the CCD with the help of the visualization tool ds9. If each spectrum lies on a straight line on the fiber, the next steps can be performed: wavelength calibrations. The creation of the master lamp frame is best performed with lamp calibrations taken during the night with the night calibration template. If they are not available, sky lines can be used too. The used parameters for the wavelength calibration read as following:

- Size of search window around expected line positions: 20
- Bad pixel correction on arc lamp image: YES

The recipe to obtain the master lamp is done by the program with the input of the master flat frame to find the single spectra on the CCD and the first guesses in the header to extract an area around the presumed position of each line in the line catalogue. It fits every peak that is expected to be an arc line with a 3rd degree polynomium and stores this as a master lamp file. Spectra are usually located within one pixel from the expected position. Again it is possible to check this visually: the superimposed arc lines from the wavelength calibration shout fit the raw lamp frame. It is also possible to analyze the lambda calibration slit per slit and manually exclude some lines to refine the RMS. The mean RMS of the wavelength calibration should be around 1/7th of a pixel. The next step, the preliminary reduction is the last that both MOS and IFU data have in common. It subtracts the bias frame, clips the pre- and over-scan and attaches the extraction table to all scientific frames.

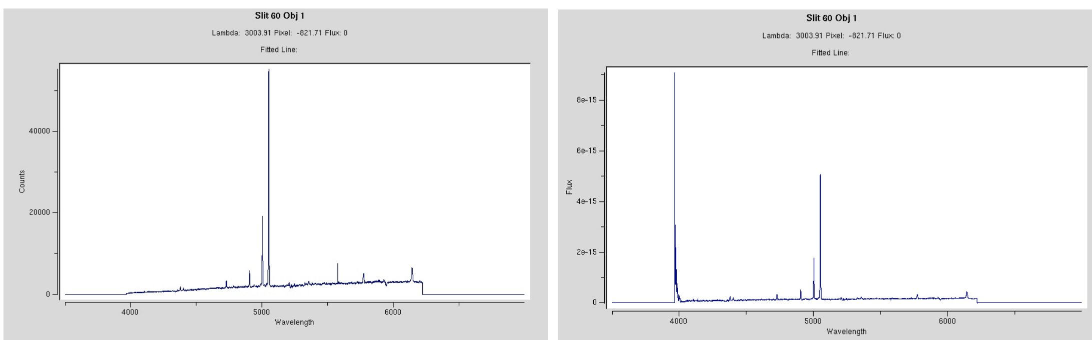

Figure 4.4: Comparison of spectra of slit 60, left: before calibration, right: after calibration

Before 2D spectra are extracted, the reduction pipeline includes cosmic ray cleaning in its recipes. Cosmic rays can alter spectral intensities and thus have to be filtered out. To ensure that this is possible also with a single exposure (where the observation can't be cross-checked with another frame of the same field and Cosmics are picked out), an algorithm has been included in the pipeline. It is based on the theory that spectra show a smooth behavior in their intensities along the wavelength direction. Cosmic rays are distinguished by their steep and abrupt changes whereas emission lines or sky lines show a smooth intensity gradient. Every intensity gradient of each IFU spectrum traced along the CCD is analyzed. The rms and local mean values are computed inside a window and at the sign of a cosmic ray, clipped and re-computed after an additional check. The cosmic ray hits removal method is tested to be efficient and ∼90 % are removed (Zanichelli et al., 2005).

For the spectrophotometry calibration, observations of standard stars are needed. It is wise to use exposures of stars taken during the same night as the science exposures. The same grism/filter combination is needed to ensure good results and one standard file per quadrant needs to be reduced. Standard stars are automatically identified by the program and classified as standards. Files of standards are to be treated the same way as science files up until preliminary reduction. When computing spectrophotometric calibration, first 1D extracted spectra should be retrieved by changing the parameter of the recipe. It is necessary to go through the 1D spectra of each slit of the resulting BFCR-corrected file to identify the lines where the star spectra are visible. Then the recipe is to be run again, this time with the information added where the star is visible. For this it is required to fill in the lines containing the best signals from the star. The program then extracts the line, sums them together and computes the sensitivity function, which is then used for further refinements, converted in $\mathrm{erg\,cm^{-2}\,sec^{-1}\mathring{A}^{-1}}$. This is the ratio between the sum of extracted spectra and the standard star spectrum. This way all the spectra containing flux from the standard star are summed together. Even though it is tedious to go through the whole reduction process again and then look at the plots of each single spectra going through the spectra slit by slit, the spectrophotometric calibration is an important part of achieving the best results for the data cube. With VIPGI, it is possible to check the extracted spectra from biased and flat-fielded frames by using the *Display Image* tool. Both the extracted 2D image with the extension *EXR2D*, containing the corrected BFC files, as well as 1D image (*EXR1D*, a summation over the spatial direction of the 2D spectrum (Horne, 1986; Zanichelli et al., 2005), can be studied. Skylines appear as round lights aligned in the Y direction (see Fig. 4.5).

Finally with the Reduce Single Observation recipe, fiber relative transmission is corrected, sky subtraction performed, and flux calibration with the results of the standard star tables applied. The reason why one has to correct for relative transmission is that fibers have different transmission efficiencies, which change the intensities of the spectra. This can be compared to the pixel to pixel sensitivity variations that require flatfielding. The fine relative transmission correction, one of the parameter options of this recipe is based on the sky line flux determination. It is assumed that the flux of sky lines are constant in all fibers within one observation and that there are no spatial variations within the FOV. The program integrates a custom chosen sky line (e.g. the lambda used in the given data with blue grisms is 5577 Å, a broadened skyline well known) over N points

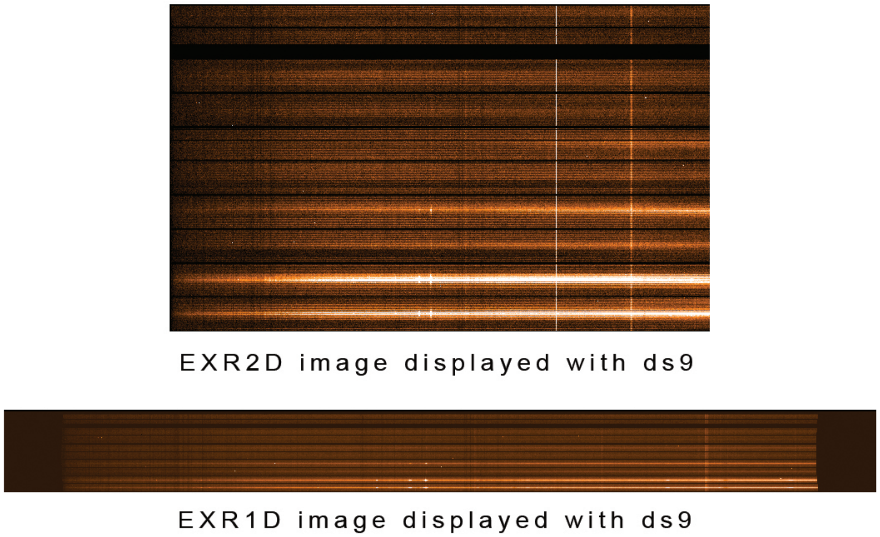

Figure 4.5: Checking Mrk 607's extracted spectra (BFCEx files) with VIPGI's *Display Image* tool.

and computes a correction factor. A second-order polynomial fit is calculated around the sky line to get the best approximation of the continuum underlying the sky line. The resulting flux under the sky line is considered to be the same for all fibers. This process is performed on the science data themselves. The continuum may or may not be subtracted, that is left optional, but it is recommended to do so. If the subtraction is performed, the gap around the skyline shouldn't exceed 3-5 pixels but big enough for statistics. After correction for fiber relative transmission, spectra are grouped and the integrated flux over a large wavelength range is computed. All fibers having a flux value within mode +/- threshold are defined to be on the sky alone. They are combined and the resulting sky spectrum is subtracted from the fibers of the given group. Further checks can be done to improve the rms by additionally excluding dead fibers etc. VIMOS IFU is not designed to have fibers that are known to fall on the sky, in a manner of speaking, sky dedicated fibers. In slit spectroscopy, you have regions with pure sky emission and regions with object signal, not so in IFU. Here spectra are the superposition of sky background and object contribution or solely sky background. Thats why this choosing and combining of spectra, which are likely to contain pure sky signal is necessary.

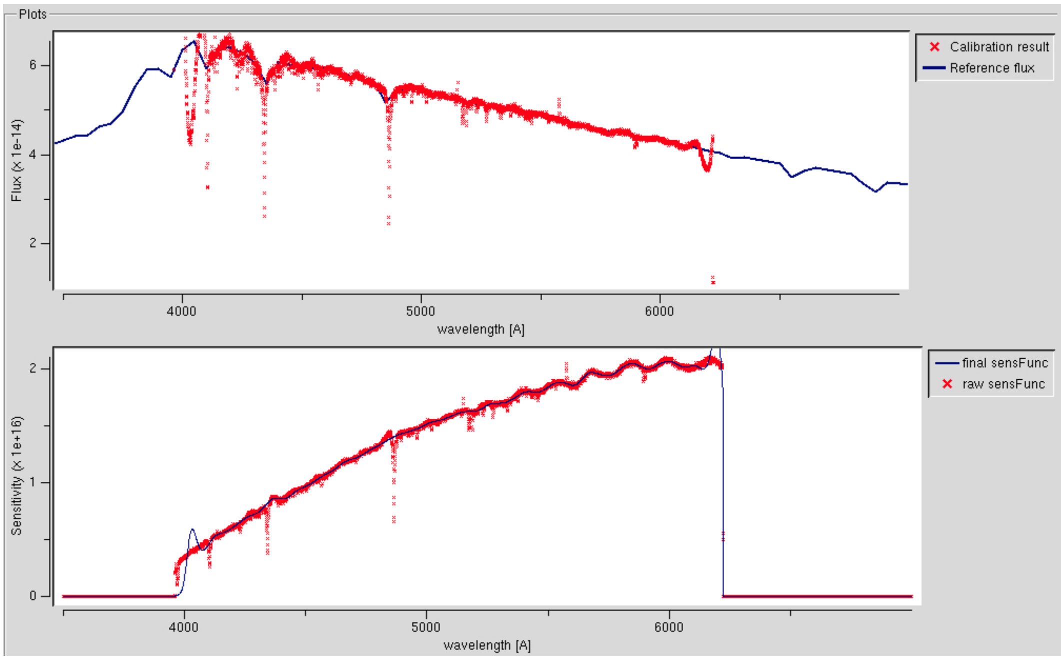

Figure 4.6: Checking of spectrophotometric calibration, provided by VIPGI

Finally, to obtain the data cube, all the jittered sequences made on a pointing have to be combined to reduce a sequence of IFU observations. All four quadrants have to be reduced in the explained way to form a file called _seq.fits which contains the data cube. This is done in the *all quadrants* sheet where selected files can be combined. The resulting file contains: in the primary image, the data, organized one spectrum per row; an IFU table, which gives for each row the corresponding location on the IFU head; and an OBJ table. The output of the procedure is therefore simply a FITS image containing all the stacked 1D spectra where each spectrum is written in a row of the output image (Zanichelli et al., 2005). This end result of the VIPGI pipeline acts as the starting point for analyzation tools or customized codes that further answer scientific questions. The cube can also be rebuild as a 2D image for scientific analysis and further manipulations can be performed.
To summarize, the extraction procedure of VIMOS IFU spectra consists of tracing spectra on the CCDs, applying wavelength calibration and extracting 2D and then 1D spectra.
A word on Crosstalk: Since VIMOS IFU was built with a large field of view with

so many spectra lying along 2058 CCD pixels, one fiber projects on five pixels. This leads to crosstalk, a kind of contamination among the spectra. The correction for this problem must be measured beforehand in the lab from fiber modules as a combination of three Gaussian functions, one modeling the core of the fiber, and the other two modeling the wings. In testing this correction it turns out that only ~5% of the flux of a fiber contaminates the neighboring fibers, about the same as the error introduced with the correction. That's why for IFU data reduction no crosstalk correction was implemented.

Zanichelli et al. (2005) have estimated the overall absolute flux accuracy to be of the order of 15 %, with the main uncertainties being the cross talk contribution (~5 %), the relative transmission correction (between 5 and 10 %) and sky subtraction (a few %).

The interested reader and user of VIPGI will be inclined to read the VIPGI Manual, provided by Garilli, Scodeggio (INAF-IASF, Milano), Zanichelli (IRA-INAF, Bolognia) et al. with the framework of the VIRMOS consortium and the VVDS project, which served as the base for this introduction to the reduction pipeline.

5 Data Analysis and Results

It has been adequately explained in the previous sections that integralfield spectroscopy holds a complex but extensive way of analyzing extragalactic data. Interpretation can be drawn from the information that each spaxel holds. The three dimensional data cube allows a simultaneous look and therefore analysis of the whole field of view. Nonetheless, information drawn from photometry can complement the spectroscopic information in order to gain further insight into the morphology. By analyzing emission lines and their profiles, dynamical and kinematical properties of active galactic nuclei can be inferred. The lines' profiles and velocities over a larger area range in ionization potential, indicating large-scale kinematical properties (Alloin et al., 1983).

5.1 The data set and quality of data

The used datasets were taken with VIMOS IFU in 2004 in high resolution mode. The galaxy UGC 1935 was observed on November 1 2004 consisting of science raw exposures of the object as well as a number of calibration frames (see Table 5.1 for reference). Data for the reference galaxy Mrk 607 were taken on October 18, 2004 and November 1 2004 with the same set up.
At the time, the borders of the IFU quadrants exhibited a number of dead pixels which needed to be sorted out manually in order to be rejected so as not to be used during the pipeline reduction step *check IFU data*. The used data did not show large fiber position shifts which would have made a reduction with the VIPGI pipeline impossible. The reduction was therefore performed with the VIPGI pipeline (see Sect. 4.2), offered by the VIRMOS consortium.
All modern instruments function with CCDs. Modern CCDs are much more sensitive than classical photographic plates offering a higher linear range. The traditional chemical photographic plates on the other hand exhibit a higher full-well capacity. This particular CCD read 2148 pixels along the x- and 4096 pixels along the y-axis at this point, with an image readout time of 44.986 with about

the same as image transfer time, and a readout noise of $\sim 3.7e^{-}$ per output. In fact, the CCDs are vignetted by some hardware and the illuminated area in spectroscopic mode is only about 1970×2300 pixels. Finally, the gain - the conversion factor from electrons to ADUs - is 2.00.

Table 5.1: Observing log. The exposure time equals the total integration time. The reduction was conducted with VIPGI.

Date yyyy-mm-dd	UT at start	object type	mode	airmass $\langle z \rangle$ at start	EXPTIME $\langle sec \rangle$	Quadrant
2004-11-01	04:17:24.606	object	IFU	1.78	800.00	4
2004-11-01	04:17:24.566	object	IFU	1.78	800.00	3
2004-11-01	04:17:24.605	object	IFU	1.78	800.00	1
2004-11-01	04:17:24.565	object	IFU	1.78	800.00	2
2004-11-01	04:35:08.584	flat	IFU	1.00	60.00	3
2004-11-01	04:35:08.595	flat	IFU	1.00	60.00	4
2004-11-01	04:35:08.594	flat	IFU	1.00	60.00	1
2004-11-01	04:35:08.583	flat	IFU	1.00	60.00	2
2004-11-01	04:41:08.534	wave, lamp	IFU	1.00	9.00	3
2004-11-01	04:41:08.542	wave, lamp	IFU	1.00	9.00	4
2004-11-01	04:41:08.533	wave, lamp	IFU	1.00	9.00	2
2004-11-01	04:41:08.541	wave, lamp	IFU	1.00	9.00	1
2004-11-01	09:55:56.117	bias	IMAGE	-	0.061	4
2004-11-01	09:50:45.314	bias	IMAGE	-	0.061	1
2004-11-01	09:53:15.551	bias	IMAGE	-	0.061	4
2004-11-01	09:56:48.112	bias	IMAGE	-	0.061	4
2004-11-01	09:56:48.116	bias	IMAGE	-	0.061	3
2004-11-01	09:51:22.868	bias	IMAGE	-	0.061	2
2004-11-01	09:52:00.435	bias	IMAGE	-	0.061	3
2004-11-01	09:55:04.351	bias	IMAGE	-	0.061	1
2004-11-01	09:51:22.879	bias	IMAGE	-	0.061	4
2004-11-01	09:53:15.540	bias	IMAGE	-	0.061	2
2004-11-01	09:52:37.995	bias	IMAGE	-	0.061	1
2004-11-01	09:51:22.878	bias	IMAGE	-	0.061	1
2004-11-01	09:54:12.595	bias	IMAGE	-	0.061	1
2004-11-01	09:53:15.541	bias	IMAGE	-	0.061	3

Table 5.1: Observing log (continued).

Date yyyy-mm-dd	UT at start	object type	mode	airmass ⟨z⟩ at start	EXPTIME ⟨sec⟩	Quadrant
2004-11-01	09:53:15.550	bias	IMAGE	-	0.061	1
2004-11-01	09:55:56.116	bias	IMAGE	-	0.061	1
2004-11-01	09:50:45.315	bias	IMAGE	-	0.061	4
2004-11-01	09:52:37.988	bias	IMAGE	-	0.061	3
2004-11-01	09:55:04.354	bias	IMAGE	-	0.061	3
2004-11-01	09:54:12.588	bias	IMAGE	-	0.061	3
2004-11-01	09:52:00.434	bias	IMAGE	-	0.061	2
2004-11-01	09:57:39.892	bias	IMAGE	-	0.061	3
2004-11-01	09:51:22.869	bias	IMAGE	-	0.061	3
2004-11-01	09:55:56.098	bias	IMAGE	-	0.061	2
2004-11-01	09:57:39.856	bias	IMAGE	-	0.061	1
2004-11-01	09:56:48.111	bias	IMAGE	-	0.061	1
2004-11-01	09:56:48.115	bias	IMAGE	-	0.061	2
2004-11-01	09:50:45.317	bias	IMAGE	-	0.061	3
2004-11-01	09:52:00.432	bias	IMAGE	-	0.061	1
2004-11-01	09:55:04.352	bias	IMAGE	-	0.061	4
2004-11-01	09:50:45.316	bias	IMAGE	-	0.061	2
2004-11-01	09:54:12.587	bias	IMAGE	-	0.061	2
2004-11-01	09:57:39.891	bias	IMAGE	-	0.061	2
2004-11-01	09:52:00.433	bias	IMAGE	-	0.061	2
2004-11-01	09:55:04.353	bias	IMAGE	-	0.061	2
2004-11-01	09:52:37.987	bias	IMAGE	-	0.061	2
2004-11-01	09:55:56.099	bias	IMAGE	-	0.061	3
2004-11-01	09:54:12.596	bias	IMAGE	-	0.061	4
2004-11-01	09:57:39.857	bias	IMAGE	-	0.061	4
2004-11-01	09:52:37.996	bias	IMAGE	-	0.061	4
2004-11-01	08:31:05.587	STD	IFU	1.012	123.00	1
2004-11-01	08:31:05.588	STD	IFU	1.012	123.00	4
2004-11-01	08:31:05.589	STD	IFU	1.012	123.00	2
2004-11-01	08:31:05.590	STD	IFU	1.012	123.00	3
2004-11-01	08:34:14.686	STD	IFU	1.013	123.00	1
2004-11-01	08:34:14.687	STD	IFU	1.013	123.00	4
2004-11-01	08:34:14.679	STD	IFU	1.013	123.00	2

Table 5.1: Observing log (continued).

Date yyyy-mm-dd	UT at start	object type	mode	airmass ⟨z⟩ at start	EXPTIME ⟨sec⟩	Quadrant
2004-11-01	08:34:14.680	STD	IFU	1.013	123.00	3
2004-11-01	08:37:20.686	STD	IFU	1.015	123.00	4
2004-11-01	08:37:20.685	STD	IFU	1.015	123.00	1
2004-11-01	08:37:20.681	STD	IFU	1.015	123.00	3
2004-11-01	08:37:20.680	STD	IFU	1.015	123.00	2
2004-11-01	08:40:27.862	STD	IFU	1.017	123.00	3
2004-11-01	08:40:27.861	STD	IFU	1.017	123.00	2
2004-11-01	08:37:27.865	STD	IFU	1.017	123.00	4
2004-11-01	08:37:20.864	STD	IFU	1.017	123.00	1

5.1.1 UGC 1935

The Seyfert 1.5 galaxy UGC 1935 (NGC 0931 or Mrk 1040) is a mag=14.46 nearby galaxy at z=0.0166, located at RA 02h28m14.5s and DEC +31d18m42s. It is part of a group (Garcia, 1993). LEDA 212995 is the galaxy's close companion and has already been observed in several photometric and spectroscopic setups, including U and I band photometry to look for interaction signatures between them. The analysis of the observations show a strong, point-like center of the main galaxy, common for Seyfert galaxies as well as an irregular structure of the companion (Popović et al., 2005) and star formation signatures in the stellar disk of UGC 1935. Although no tidal tails are observed between the galaxies, a connection and interaction is very likely and this result has been published by Colbert et al. (1996) and more recently by Kuo et al. (2008) who observed a set of 23 galaxies in H I, which is the most sensitive and enduring tracer known of tidal interactions. In Ward & Wilson (1978)'s letter from 1978, the galaxy was already discussed as an interacting Seyfert galaxy. The galaxy itself is highly inclined while its companion lies $\sim 19''$ ($\sim$7 kpc) to the north. Both show a similar redshift, but the companion is much smaller and dimmer than the Seyfert galaxy. The velocities of the two are so close, indicating interaction as well: LEDA 212995 has a velocity of 4797 km s^{-1} whereas UGC 1935's velocity reads 4992 km s^{-1}.

As seen in Fig. 5.1, fairly prominent spiral arms extend to both the north-

Figure 5.1: UGC 1935 (NGC 931, Mrk 1040) with companion LEDA 212995. The galaxy lies about 51 Mpc away and spans about 12.9′. North is left and East is down in this image. Data courtesy: SDSS

eastern and south-eastern direction, either hinting towards distortions in the form of dragged out tidal arms due to the companion or – more likely, since they are symmetrical – they are simply spiral arms extended further out.
The nucleus of the galaxy is included in the XIth list of galaxies with ultraviolet continua as Mrk 1040 (Markarian et al., 1977). Amram et al. (1992) discuss UGC 1935's asymmetrical optical velocity field which they ascribe to a large scale and a massive bar. The companion was analyzed with slit spectroscopy by Ward & Wilson (1978) and shows strong but narrower emission lines than UGC 1935 itself, suggesting that they are due to the interaction with UGC 1935. Since the double spectral profiles of the areas where the companion overlaps the main galaxy is dominated by the companion's signatures, it is reasonable to believe, that the companion is located closer to the observer than UGC 1935. Results from Kuo et al. (2008)'s H I investigations are shown in Fig. 5.2

The galaxy furthermore shows a complex spiral arm structure that are asymmetric in that sense, that H II regions to the east extend much further than to the west. This asymmetry is another indication for an interaction with the companion.
Fig. 5.3 shows the orientation and setup of the four quadrants of the VIMOS IFU as an overlay onto an image of the galaxy UGC 1935.

Table 5.2 gives general characteristics of the galaxy taken from the rotation curve. Values from literature were taken from NED.

Table 5.2: Characteristic values for UGC 1935

Type	Redshift z	Mean Metric Distance [Mpc]	Position Angle [Degrees]	Velocity of the nucleus	Scale [pc arcsec^{-1}]
SAbc	0.016652	51.533	73	4992 km s^{-1}	339

UGC 1935 is also classified as a narrow line Seyfert 1 galaxy (NLS1). This type of galaxy shows permitted lines of their broad line regions smaller than usual ($< 2000\,\mathrm{kms}^{-1}$), but still broader than the forbidden lines. Osterbrock & Pogge (1985) first classified this type of AGN. The emission ratios indicate the presence of a high-density region, like in a broad line region. UGC 1935's FWHM was measured to be $\sim 183\,\mathrm{kms}^{-1}$. One idea is that there is a connection between the viewing angle and the type of AGN concerning NLS1's, similar to the distinction between Sy 1s and Sy 2s (Fischer et al., 2011). Another (current) model suggests that NLS1's have massive black holes with lower masses ($\leqslant 10^7 M_\odot$) radiating

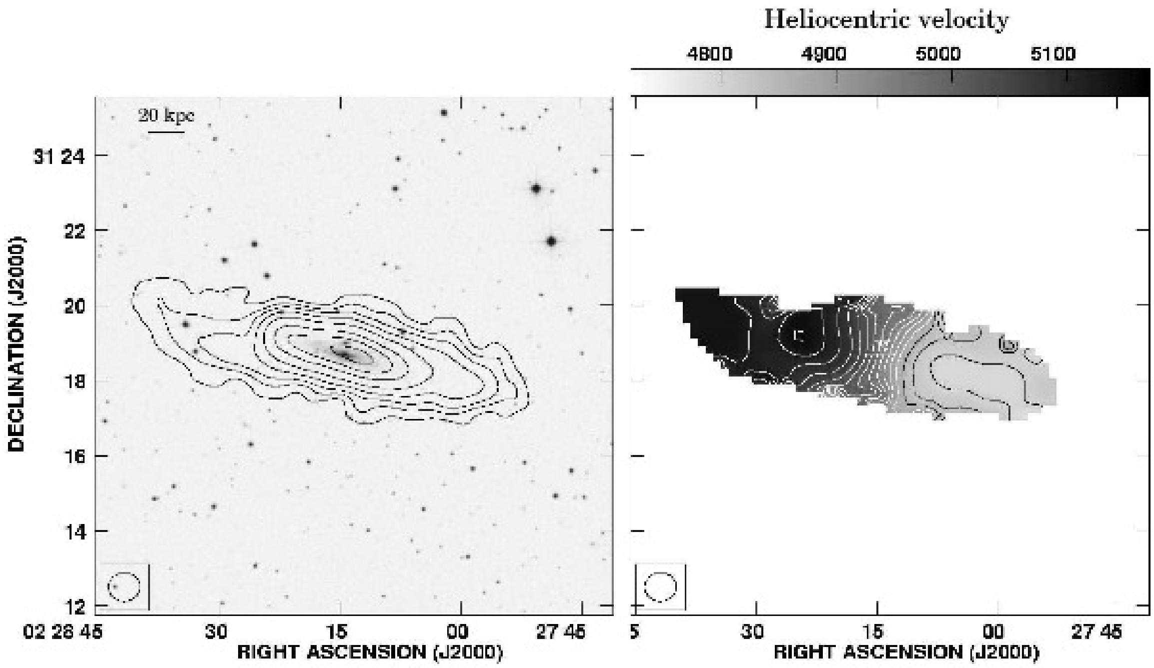

Figure 5.2: Contours of integrated H I intensity (zeroth moment) overlaid on the DSS2 image (left, contours are plotted at $1, 5, 10, 20, 40, 80, 120, 160 \times 30\,\mathrm{mJy\,beam}^{-1}$) and map of intensity-weighted H I mean velocity (first moment; right). Velocities are indicated by the scale wedge, and contours plotted at intervals of 25 km/s. Images taken from Kuo et al. (2008).

close to their Eddington limits (Pounds et al., 1995; Mathur et al., 2001). Here, the narrower widths are due to clouds rotating around the BH. Crenshaw et al. (2003) describe that the steep soft X-ray continuum in these objects is the high-energy tail of the "big blue bump", which is said to be emission from the accretion disk peaking in the extreme (see Sec. 5.5). This high energy comes from the high accretion rates and hot thin disks in NLS1's (see also Fig. 5.19). Drawing the connection to the distinction cirteria between Sy 1s and Sy 2s once again, raises the question whether NLS1s could simply be viewed more "pole-on"than normal BLS1s (Ulvestad et al., 1995).

Fischer et al. (2011) propose a pole-on orientation to be rather common on

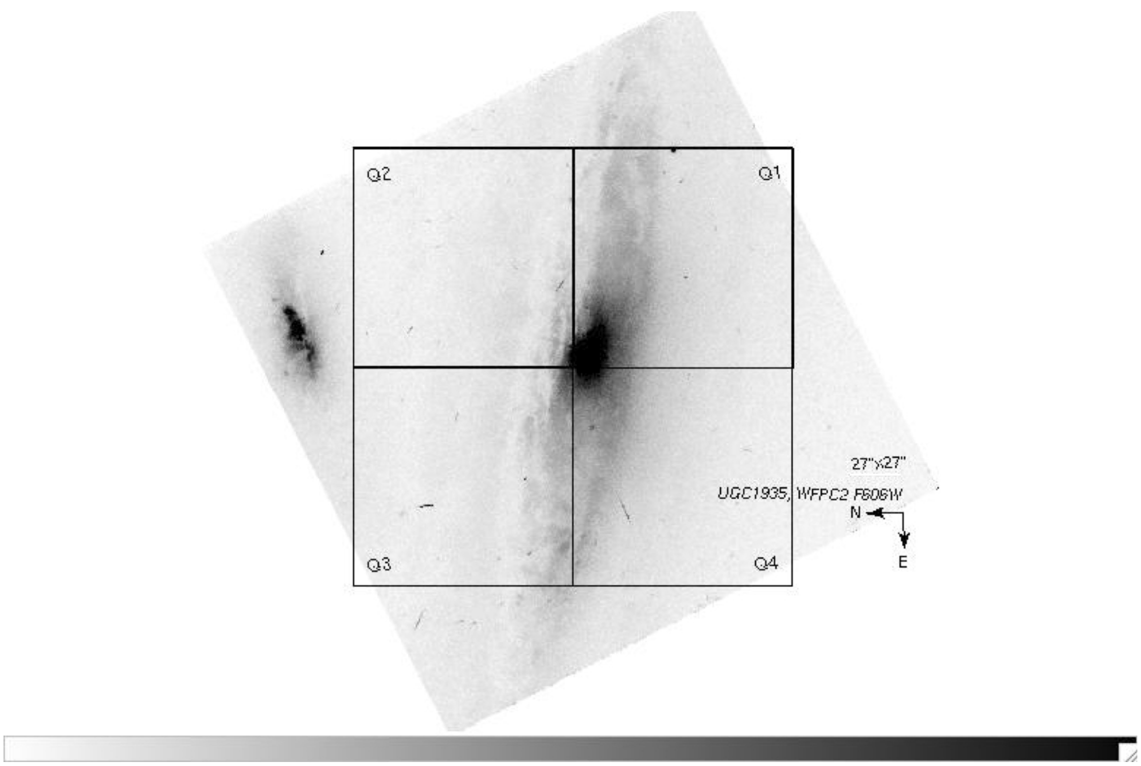

Figure 5.3: UGC 1935 with an overlay of the four quadrants of VIMOS IFU. The total FOV is $27'' \times 27''$.

NLS1's, based on the analysis of several of these galaxies. This assumption can be underlined by UGC 1935's highly blueshifted velocities near the nucleus (see Chapter 5).

Asymmetries found by Amram et al. (1992) using $H\alpha$ lines observed with a Fabry-Perot interferometer are most likely a consequence of the interaction between the two. UGC 1935 exhibits an extended disc and a buldge of $<$3 kpc. Both the active nucleus as well as the stellar disk are interesting to study. When investigating the connection between the global behavior and the active nucleus, both the velocity information as well as the ionization information can be studied. The galaxy's companion LEDA 212995 shows emission lines indicating a star-forming region (Popović et al., 2004).
Exploring the data cube itself allows assessment of the quality of the data and a more extensive analysis of the full spectral range would reveal information of both continuum processes like blackbody surface temperature, as well as non-thermal and quantum processes like absorption and emission lines from electron transitions in heated atoms of various elements – throughout the entire field of view.
An indication for how the emission line intensities of an AGN behave in the example of the present galaxy can be evoked through looking at the spectra at different locations of the galaxy. Figure 5.4 shows a few examples of spectra generated with a customized IDL tool written by Robert Sharp (presently instrument Scientist at the Australian National University).

Even though the nuclear emission of the AGN stems from a core region of the size of a point source and should therefore only be detected in the central pixel, atmospheric seeing effects smear out the emission. The broad components of the emission arise from this central region. In the case of the Sy 1.5 galaxy UGC 1935, one can see how $H\beta$ is broader than seen in the comparison galaxy, the Sy 2 galaxy Mrk 607 (see Fig. 5.14). It has been shown that one can use the information at the wavelength of broadened lines (namely $H\alpha$ and $H\beta$) for a determination of the point spread function (PSF) (Jahnke et al., 2004). The PSF is the function that is used to describe the spatial distribution of a point source on the detector. To study the host galaxy of the AGN in its vicinity, the contribution of the AGN needs to be removed. This can only be done using PSF templates that are subsequently subtracted from the galaxy image.
A closer look at the $H\beta$ and [OIII] lines, as seen in figure 5.5, shows *wings* and *blue shoulders* in the [OIII] line hinting towards winds or jets of the galaxy itself. Features can also be seen in the broad line of the $H\beta$ emission but because of

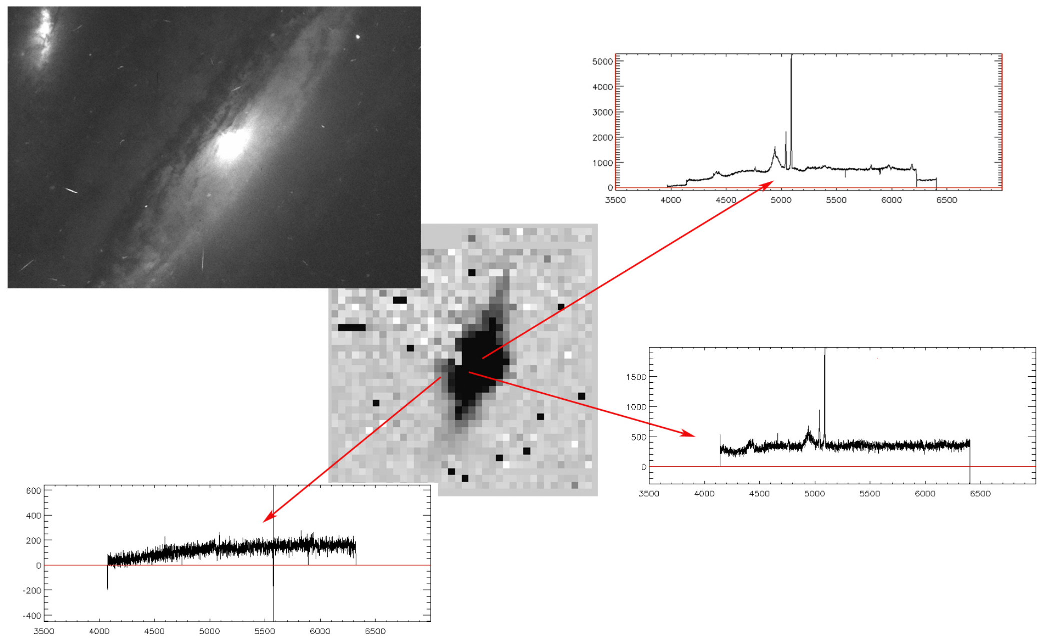

Figure 5.4: Left:UGC 1935, middle and right: spaxel information from different parts of the galaxy, the more defined spectra shows the location of the AGN.

the overlay of broad and narrow components here, it is more difficult to filter the different features. This will make a simple Gaussian analysis not as accurate as multiple fits would. The following analysis based on simple Gaussian models alone should therefore be understood as a first attempt rather than an accurate analysis.

In NLS1's like UGC 1935, the narrow permitted lines show a significantly larger contribution in flux compared to classical Seyfert 1s. The NLR flux in $H\beta$ equals 50 % of the total line flux, as mentioned in Rodríguez-Ardila et al. (2000). They further investigate that values of $[OIII]/H\beta$ are lower than those found in normal Sy 1s.

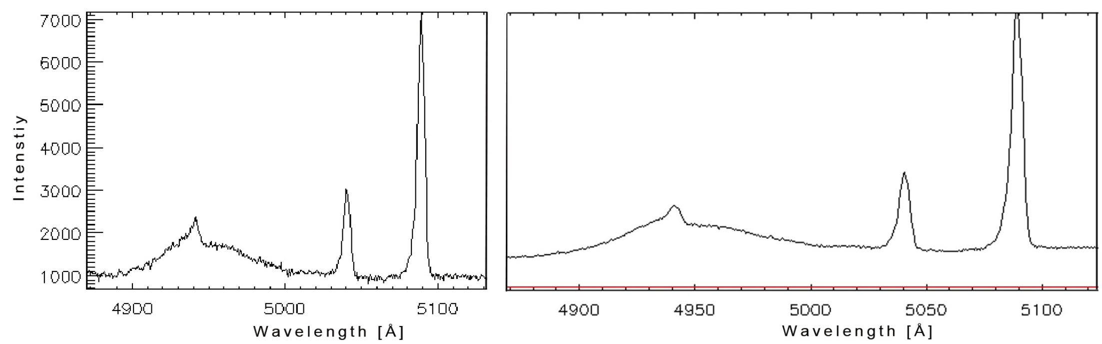

Figure 5.5: A zoom of the spectrum of UGC 1935 in the central region of the galaxy. To better visualize the *blue shoulders*, a composit of several spaxels is presented in the right panel; VIMOS data reduced with VIPGI and spectra produced by customized IDL tool (courtesy: Robert Sharp).

5.2 Emission line diagnostics

The simplest solution for abundance ratios is the "strong-line method", which uses strong, observable emission lines whose value tracks an abundance ratio (Henry & Worthey, 1999). Following Pagel et al. (1979)'s reasoning, in ionized regions

$$\frac{[OIII]}{[OII]} \propto (\epsilon^2 n N_L)^{1/3} \tag{5.2.1}$$

holds, if the stellar spectral distribution is fixed; n is the electron density, ϵ a filling factor and N_L the production rate of photons beyond the Lyman limit. One way to do this is the $R_{23} \equiv (O[III]\lambda\lambda 4959, 5007 + \text{[OII]}\lambda 3727)/\text{H}\beta\,\lambda 4861)$ method, introduced by Pagel et al. (1979) with which the knowledge of the electron temperatures becomes obsolete. This method relates the sum of the intensities of [OIII] and [OII] to the total oxygen abundance O/H. The VIMOS blue grism set-up does not give information of the [OII] line, therefore the total oxygen abundance O/H is directly presented to the reader. Oxygen is produced by stars with $M > 8M_\odot$ only.
The BPT diagram (see sec. 1.2.6) asks for four lines, two ratios, one on each axis. Because the ratio of lines [NII] and Hα are not accessible through this dataset, analysis must be constricted to the two measurable lines [OIII] (both lines of the

doublet were visible and strong, but in the following, the [OIII]λ5007 line was used) and Hβ. The following *first-approach assumption* allows an analysis for the Seyfert 1 galaxy with respect to metallicities nonetheless. Fig. 5.6 describes the metallicity as a simplified curve in the BPT diagram with allocated areas that can be ascribed to regions within a galaxy. If now only information of [OIII] and Hβ are available, and the curve therefore *collapses* onto the y-axis, one can still make valuable predictions.

The emission line map of the galaxy's oxygen abundance was created by fitting the individual spectra of the cube with Gaussian profiles. The lines were approximated with single Gaussian profiles where each line is fitted independently for every spaxel of the data cube (see Fig. 5.7). This first approach does not take more complicated effects into account such as line splitting and asymmetries of the emissions. These effects have been looked at individually to give hints to outflows where blue/red shoulders of emission lines give kinematic information to these outflows. To obtain a more detailed analysis, a full deconvolution of the data cubes, informed by kinematic models would be necessary and will not be performed here (see also Westmoquette et al. (2009b)).

Fig. 5.7 shows that even though narrow lines are fitted just fine with this single Gaussian first-approach, the fit for the broad component yields a first estimation only. Significant errors in the BLR shouldn't be left unmentioned: The effect of this simplification can be understood as an enhancement of the drop in the O/H gradient (Fig. 5.9). For the further analysis fluxes were measured; the detailed kinematics of the split line is not part of this work and asks for at least two or – better – several Gauss fits. Therefore a number of drawbacks need to be mentioned when dealing with this first analysis of the IFU data: so far no additional account has been taken to subtract the underlying stellar component which gives rise to absorptions. For this Balmer lines higher than $H\beta$ are needed. This results in an underestimate of the flux in $H\beta$ and in areas with higher stellar contribution, the $[OIII]/H\beta$ ratios will therefore be slightly overestimated (see also Sharp & Bland-Hawthorn (2010) for this). More so, the instrumental set up of the VIMOS archive data was HR blue, making only a limited analysis of emission lines possible. The wavelength range for the given grism, 4150 – 6200Å comprises several interesting emission lines that can be seen in Table 5.3.

This table lists both absorption and emission lines. The strong emission lines from this list that are commonly seen in AGNs like UGC 1935 are the Hβ and [OIII] line while Hδ and Hγ are weaker emission lines. To give more adequate

Table 5.3: Some important lines that fall within the wavelength range of the VIMOS IFU HR blue grism setup

Element	Central Wavelength ([$\AA$])	Excitation of Emission lines (Collision/Recombination)
Hδ	4101.7	R
Ca I, g band	4226.7	
Fe I	4271.7	
G band	4300.4	
H I	4340	R
Fe I	4329.7	
He II	4338.6	
Hγ	4340.5	
[OIII]	4363.2	C
Fe I	4383.5	
He I	4471.5	R
He II	4685.7	R
Hβ	4861.3	R
Fe I	4920.5	
[OIII]	4958.9	C
[OIII]	5006.8	C
Mg I blend	5175.4	
[N II]	5199	C
Ca+Fe (E band)	5269.0	
[FeVII]	5721.0	
He I	5875.6	R
Na blend	5892.5	
He II	5977.0	
[FeVII]	6087.0	

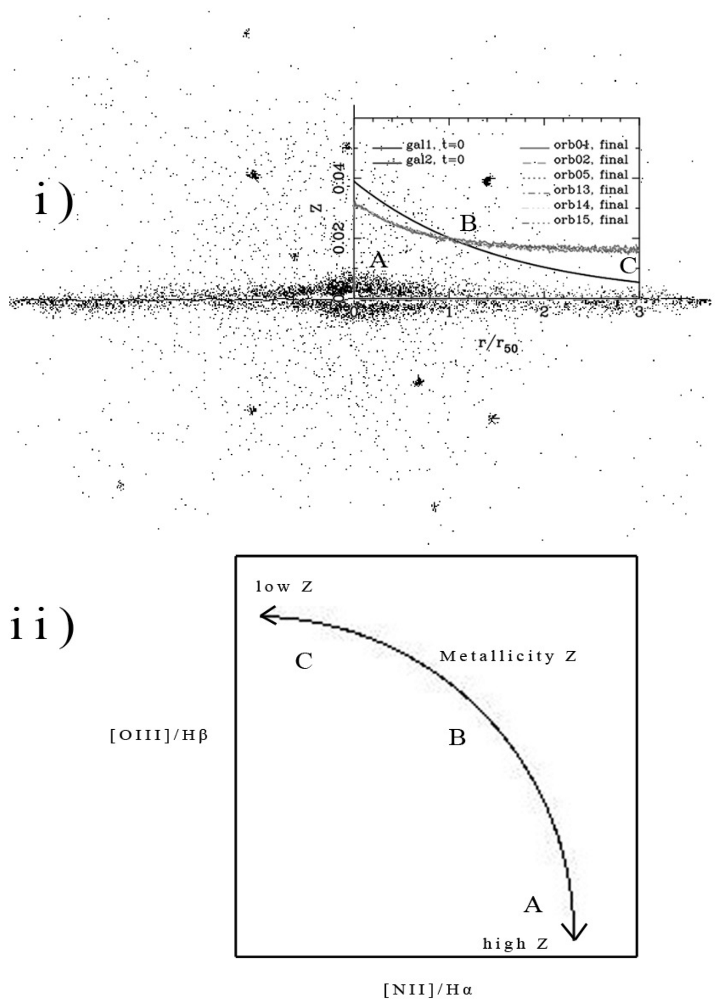

Figure 5.6: i) shows the schematics of a galaxy with a graph overlaid by Di Matteo et al. (2009) showing the rising metallicity gradient in a major merger. Metallicity is shown vs. the distance from the galaxy center. A, B and C mark the regions in the galaxy (inner, half-way, outer regions) that can be seen in the panel below. ii) shows the simplified BPT diagram with a curve indicating metallicity Z and locations of regions A, B, C.

information including the red end of the spectra, an additional observation run with the HR red grism would have been needed. This limited wavelength coverage,

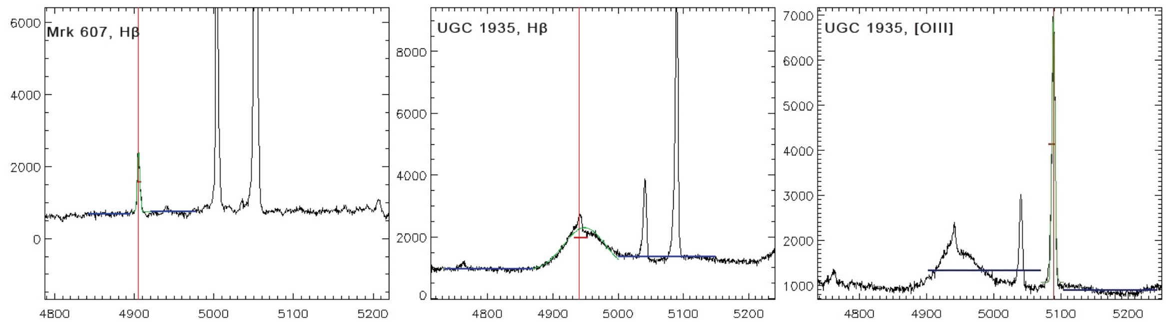

Figure 5.7: Examples of the calculation of single Gauss curves (green lines) for: narrow Hβ emission line of Sy 2 galaxy Mrk 607 (left), broad Hβ line for Sy 1 UGC 1935 (middle) and [OIII] line for UGC 1935 (right). Used tool written by Robert Sharp.

confining the emission lines to the prominent Hβ and [OIII] doublet as well as Hγ, the iron-bump and a bit of Hδ, hinders a proper extraction of the stellar continuum. This leads to an underestimate of the flux of the Hβ emission resulting in a slight overestimation of the presented [OIII]/Hβ ratios in regions where stellar continuum is expected to be higher, i.e. the outer regions of the galaxy.
Emission line fittings were performed using a custom IDL program developed by Robert Sharp. The instrumental set up of HR blue grisms restricts the analysis to the two emission lines Hβ and the [OIII] λ λ4959, 5007 doublet. The shape of the Gaussian fits can be described by the general formula

$$f(x) = A_0\, exp\left(-\frac{1}{2}\left(\frac{x - A_1}{A_2}\right)^2\right) \tag{5.2.2}$$

and more specifically for the case of emission line fitting

$$f(\lambda, \sigma, f_0, \lambda_0) = \frac{f_0}{\sqrt{2\pi\sigma}}\, exp\left(-\frac{1}{2}\left(\frac{\lambda - \lambda_0}{\sigma}\right)^2\right) \tag{5.2.3}$$

with σ for dispersion, f_0 for the total flux integrated and λ_0 for the rest frame wavelength while λ is the measured wavelength. The line is doppler shifted due to the redshift of the galaxy. Assuming the above mentioned formulas for the wavelength shift and the doppler velocity, $\Delta\lambda = (\lambda - \lambda_0)$ and $v = c\Delta\lambda/\lambda_0$ respectively, equation 5.2.3 can be written for the velocity as

$$f(v, \sigma, f_0, \lambda_0) = \frac{f_0}{\sqrt{2\pi}\sigma} exp\left(-\frac{1}{2}\left(\frac{v\lambda_0}{c\sigma}\right)^2\right). \quad (5.2.4)$$

Further more, due to quantum mechanical effects, a ratio between the [OIII] doublet from the ionized oxygen atoms of 1:3 is set as a constraint (Storey & Zeippen, 2000), together with the assumption that they show the same velocity and dispersion.
The mapping of the whole galaxy's abundance patterns provides a snapshot of the abundance picture the way it is currently looking, whereas in comparison the abundances of stars show which state the star was in while it was formed (Henry & Worthey, 1999).
The abundances discussed here were taken directly from the galaxy, there was no attempt to homogenize them by recalculating the abundances in a consistent way. The inconsistencies and uncertainties arising from observational and reduction drawbacks as well as simple modelings are greater than the different techniques to yield abundance ratios, but this first presentation can give patterns and ideas to see the big picture. The relative strength of the used lines and the adopted threshold $[OIII]/H\beta > 3$ (Ho et al., 1997) helps separating AGN ionized regions from LINERs and SF regions. If the above ratio is larger than 3, high ionized sources are indicated (Kuźmicz, 2009). Very high ratios indicate ionization from non-stellar radiation.
The obtained measurements from the line ratios for UGC 1935 are mapped in Fig. 5.9. They show both the nuclear regions as well as the ENLR and are below the theoretical threshold of Ho et al. (1997) for the majority of the spaxels (spacial pixels) in the central region, confirming results for a typical narrow line Seyfert galaxy type 1. In the vicinity of the central spaxels though, a strong ionization region rises the value of the ratio to above 3. The map portrays an increase in oxygen abundances with a sudden and steep drop in the center. Part of the drastic drop can most probably be ascribed to the simple Gauss fits which results in underestimations of measurements in the center. Due to this fact, the "hole "in the middle of the galaxy is more dramatic than expected.
The drop in the central region could indicate an inflow of material but could also

have other dynamical or morphological reasons. The ring-like structure around the nucleus almost looks like a physical barrier. The ionizing region in Seyfert galaxies is the AGN in the center, a higher value would be expected. UGC 1935 has been classified as a H II-type galaxy before by Veilleux & Osterbrock (1987) according to its location in the BPT diagram. This makes it obvious, that classifications of this sort are often more difficult and object to variations and subjective analysis. The galaxy has been classified as a Sy 1 galaxy more often than never but shows here that both values are true, depending on where the measurements were taken. The map can be read as follows: darker areas show lower ratios, typically indicating regions dominating star formation, lighter areas indicate AGN ionized regions.

Previous observations of the galaxy's Hα information show most of the H II regions to be found in the spiral arms with two Hα condensations along the major axis between the spiral arms at a distance of 15$''$ from the nucleus (Amram et al., 1992), coinsiding with the maxima of rotation velocity. Coincidental, two minima are found symmetrically at 26$''$ from the center. A high Hα emission is found in the area of the companion indicating high SFR due to the interaction of the two galaxies. This has already been pointed out by Ward & Wilson (1978).

The temperature-sensitive line ratio [OIII]4363/5007 can be used as a basis for empirical abundance determinations in some cases, but the errors are quite large (Pagel et al., 1979). The typical accuracy that are here achieved through measurements of strong lines is of the order of $\pm 10\,\%$. Again a number of uncertainties makes this task difficult: the chemical composition and the various geometrical factors, the clumpiness and density effecting the ionization. The removal of the underlying integrated stellar component that is still left after the reduction process is not straightforward and only really important if the lines are weak while the absorption line spectrum is strong (Veilleux & Osterbrock, 1987). Both is not the case with the given spectra. The cooling is fixed by the oxygen abundance. Furthermore, the galaxy shows a diffuse extraplanar emission (Robitaille et al., 2007).

5.2.1 Velocity Map

With these drawbacks it is still possible to use the properties of the [OIII]λ5007 line to generate simple 2D velocity maps ultimately yielding rotation curves. This was done with UGC 1935 with iterative Gaussian fits (see section 5.2 for reference) and a constant continuum fit of each spaxel. Figure 5.10 shows the velocity map of UGC 1935 with the crosses indicating spaxels from which information was

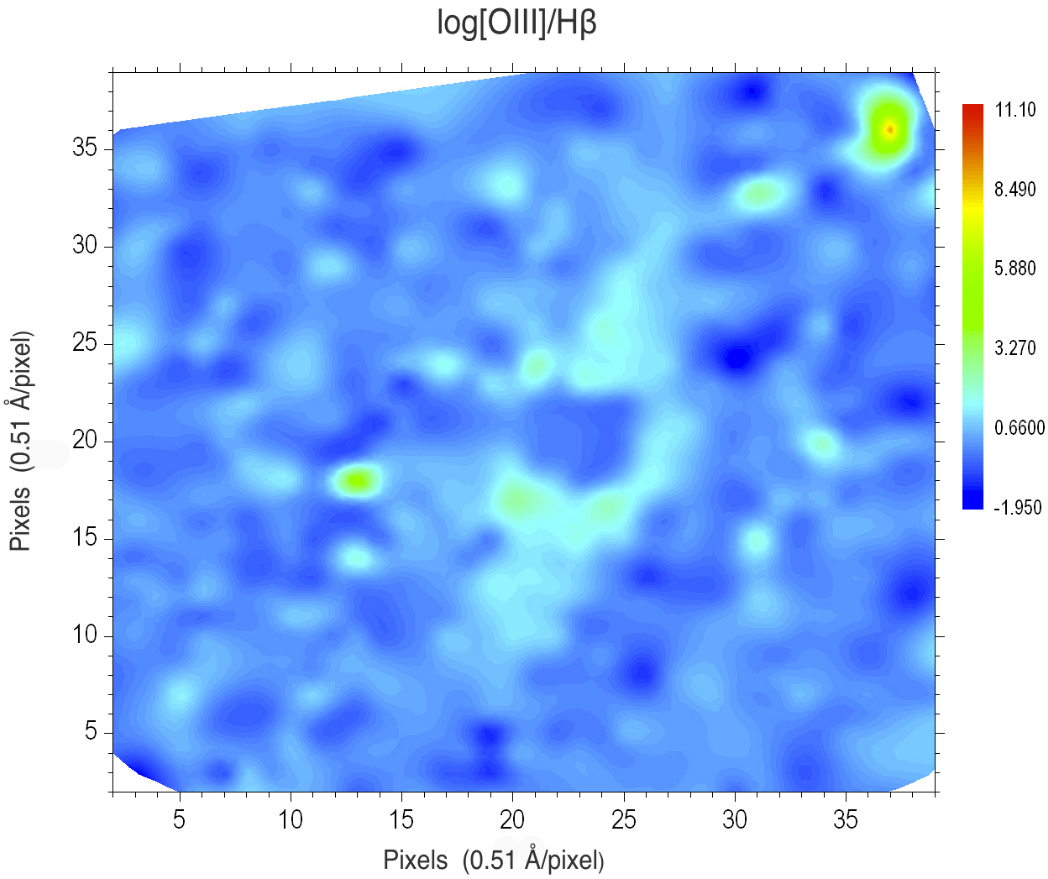

Figure 5.8: Map of log [OIII]/Hβ. The spot in the upper right corner is an artefact.

taken to compute the rotation curve. In this way a 1D long slit spectrum was simulated.
A closer inspection of the velocity map as well as an analysis of the (B-R) color distribution (Afanas'ev & Fridman, 1993) and a comparison with the optical images exhibiting dust lanes in the disk, show that the companion is closer to the observer. In addition, the northeast side of UGC 1935 seems to be farther away.

The velocity field is quite unremarkable with an average velocity shift. The rota-

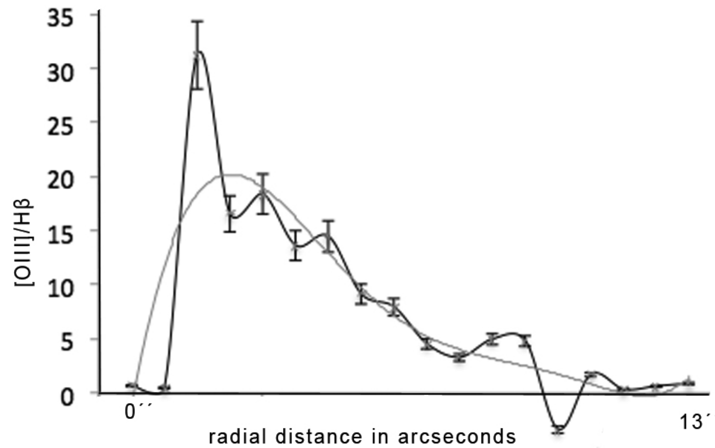

Figure 5.9: Graph of the averaged radial values of [OIII]/Hβ along the major axis of UGC 1935 (see Fig. 5.10 for reference) shown in arcseconds. The polynomial curve is shown in light grey.

tion is visible and crosses mark the spaxels from which information was extracted to produce the rotation curve in Fig. 5.11. The galaxy's rotation curve shows a small dip in the central region, either hinting towards an out- or inflow, a counter rotating curve, or a bar. One explanation, also consistent with the described theory, would be infalling material creating the observed features with an outflow from the central AGN. Both gas accretion and winds change the metallicity. They also change the gas fraction, lowering the galaxy's effective yield (Dalcanton, 2007). Furthermore, Dalcanton (2007) also states that metall-enriched outflows are mechanisms reducing the effective yield especially in gas-rich systems. An outflow in galaxies would lower the metallicity in the center though, a fact that should be considered when talking about metallicities of galaxies. This is especially true for low mass dwarf irregulars, that have lower metallicities to begin with according to the mass-metallicity relationship among galaxies. The wind that is very likely to be observed in UGC 1935 would infer the galaxy losing mass in the inner region, either explaining the lower observed metallicities completely or enhancing the effect the accretion shows.
It is therefore reasonable to propose that a combination of two effects is very likely to produce the observed lower central metallicities (see also 5.6 for details):

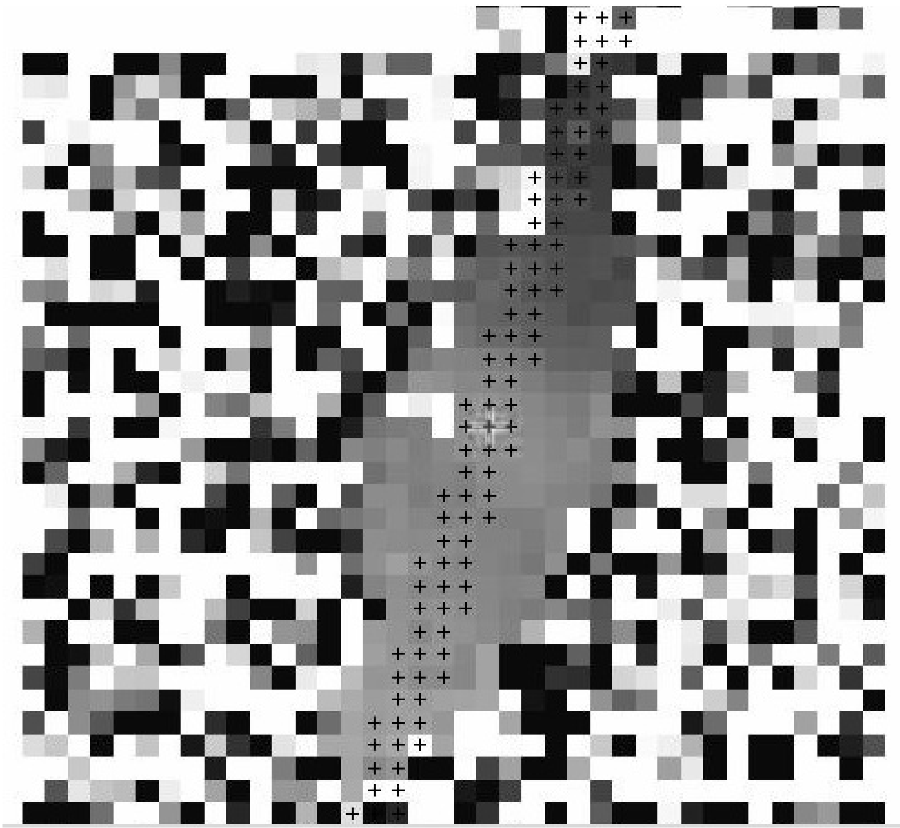

Figure 5.10: 2D Velocity map of the $27'' \times 27''$ field of UGC 1935 computed with [OIII] information, with an overlay of information taken for the radial velocity curve. Darker shades indicate redshifted areas rotating away from us, lighter areas indicate blueshifted regions. VIMOS data reduced with VIPGI and spectra produced by customized IDL tool (courtesy: Robert Sharp)

1. Infall of metal poor gas into the central region to be accreted by the black hole reduces the metallicity in the center

2. Outflows of material reduces the metallicity by driving out metal enriched gas from the system.

The idea of a counterrotating core is one already investigated by Afanas'ev & Fridman (1993) and shall be inspected in more detail in the following. The rotation

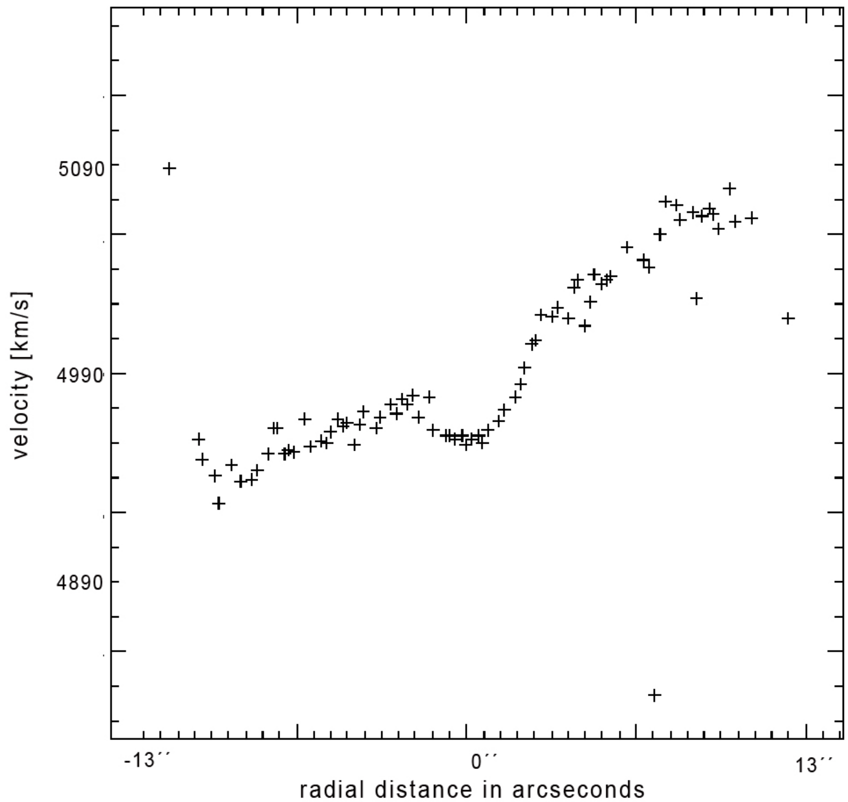

Figure 5.11: Rotation curve taken from the velocity map of UGC 1935 computed with [OIII] information, with an overlay of information taken for the rotation curve. VIMOS data reduced with VIPGI and spectra produced by customized IDL tool (courtesy: Robert Sharp)

curve shows a quite unusual shape also exhibiting velocity jumps of $> 100\,\mathrm{km\,s^{-1}}$, which in itself is nothing unusual. Afanasev (1981) first found a local minimum at $\sim 8.5\,\mathrm{kpc}$ from the center in the radial-velocity distribution along the major axis. The steeper drop that was found by Amram et al. (1992) cannot be confirmed here in that dramatic way it was first described. Already Afanas'ev & Fridman (1993) acknowledge that this drop, averaged over azimuth, is not as prominent as was first found 12 years prior to that publication. It seems the differences in rotation curves depending on the directions the curves were created, indicate local gas motions

superimposed onto the regular circular motions. Already found by Afanas'ev & Fridman (1993), the asymmetries in the galaxy show radial velocity jumps in tangential velocities. They ascribe the observed velocity jump to tangential velocities at 8.5-12.5 kpc from the center. Regions of counterrotation are therefore a valid option to be considered.
The last possibility to be considered is the existence of a bar. Amram et al. (1992) described a minibar oriented perpendicular to the line of nodes, the reason for the reverse rotation in the center, involving clumps of material, which indeed is visible in the H II distribution in $H\alpha$ images 5.12.

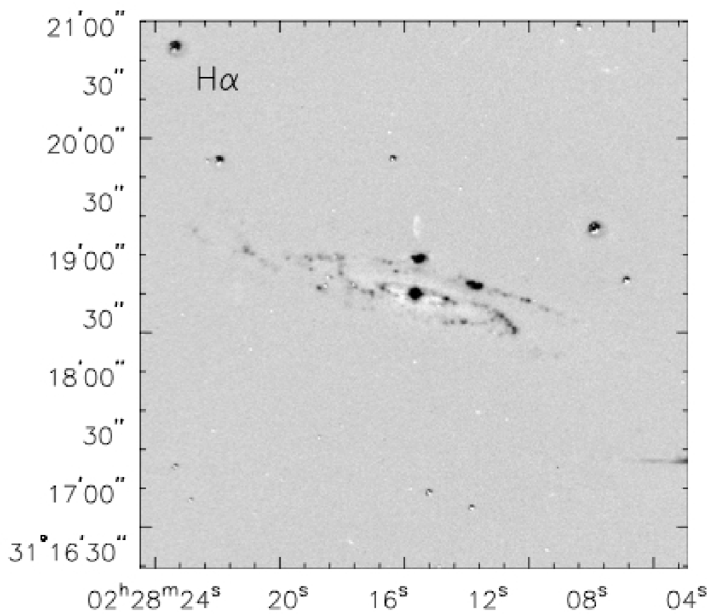

Figure 5.12: $H\alpha$ map of UGC 1935, taken from Robitaille et al. (2007)

Furthermore, Afanas'ev & Fridman (1993) argue the presence of two regions of positive and negative residual radial velocities. These are arranged symmetrically about the center, indicating "the presence of regions of reversal of the tangential velocity component inside the spiral arms in the galactic disk". This proposed anticyclonic rotation with peculiar velocitites of about $\pm 80\,\mathrm{km\,s^{-1}}$ are indeed very likely judging from the given data. They further describe vortices lying between

trailing spiral arms with the gas surface density being lowest at the centers of the anticyclones. These anticyclones are created by the dynamics in the gaseous disk as a result of gradient instabilities. (See Afanas'ev & Fridman (1993) for more details.)
In the $H\alpha$ images (Fig. 5.12), two condensations are found which coincide with the maxima that are visible in the rotation curve (more so in the published rotation curves of Afanas'ev & Fridman (1993)). They are at a distance of 15$''$ along the major axis. The companion shines brightly in $H\alpha$ as well, indicating active star formation. The measured velocity turns out to be $4993 \pm 10\,\mathrm{km\,s^{-1}}$.
The rotation curve of the companion (Fig. 5.13) is taken from Amram et al. (1992). The curve constantly rises which is common for dwarf galaxies of that kind where the halo component dominates (Amram et al., 1992).

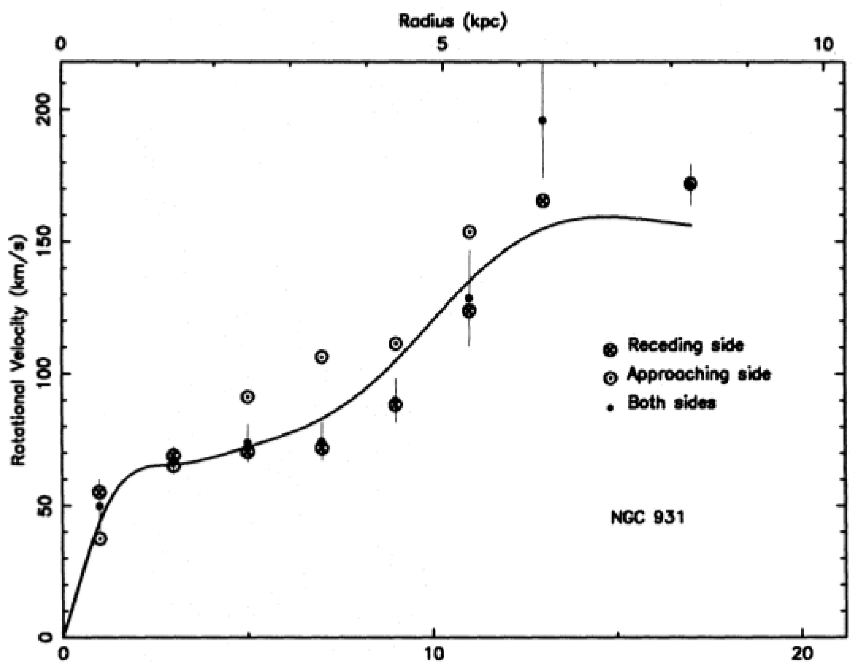

Figure 5.13: Radial velocity curve of the companion of UGC 1935, taken from Amram et al. (1992). $V_S = 5100kms{-}1$, position angle of major axis = 117 , inclination of the galaxy = 59.

Amram et al. (1992) suggest the existence of a long bar located in UGC 1935, ~20 kpc in length. Furthermore, perturbations of the velocity field that were explained therein suggest the bar to be fairly massive. Though it needs to be added that no signatures of a bar can be observed in images of the galaxy which might as well be due to the high inclination of the galaxy or the absorption of surrounding dusty material.

5.3 Mrk 607

In contrast to UGC 1935, Mrk 607 (NGC 1320) is a type Sy 2 galaxy, in which the ionizing source is hidden from view due to the obscuring dusty torus. The galaxy's coordinates are RA=03h24m48.7s, DEC=-03d02m32s at a redshift of z=0.008883 (see table 5.4). It is located in a pair with NGC 1321 which is 17 kpc away.

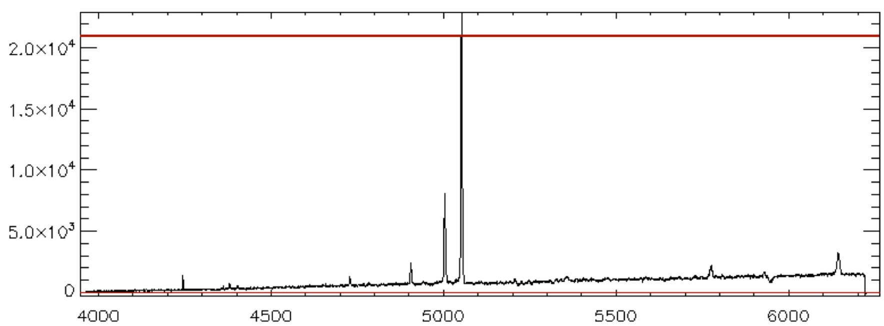

Figure 5.14: Spectrum of the Sy 2 galaxy Mrk 607, VIMOS data reduced with VIPGI and spectra produced by customized IDL tool (courtesy: Robert Sharp)

Table 5.4: Characteristic values for Mrk 607

Type	Redshift z	Mean Metric Distance [Mpc]	Position Angle [Degrees]	Velocity of the nucleus	Scale [pc arcsec^{-1}]
Sa:edge-on	0.008883	36.21	135	2663 km s^{-1}	176

As expected, the nuclear emission of this Sy 2 galaxy is much lower than measured in UGC 1935 (a central [OIII] flux of ∼199 in the Sy 2 galaxy compared to ∼68156 in the Sy 1 galaxy). This is due to the thick dust layer that hides the nuclear central region of the galaxy.

The measured $[OIII]/H\beta$ values for the center of the galaxy averages as 13.8 (with a typical value for Seyfert 2 galaxies of ~ 10). Considering that the determination value for Seyfert 2s is $[OIII]\lambda5007/H\beta > 3$, Mrk 607 is clearly a type Sy 2 galaxy where the gas is highly ionized through the AGN. No decreasing gradient was measured: With $log[OIII]\lambda5007/H\beta = 0.94$ in the outskirts and rising to $log[OIII]\lambda5007/H\beta = 1.14$ in the center (see Fig. 5.17 for a gradient of [OIII]/Hβ). This (slight) increase results in the anticipated assumption that no actual interaction of Mrk 607 with a dwarf galaxy that can be visually detected, is happening. Even though this might be true and can be corroborated by visual inspections and morphological and kinematical reasoning, conclusions concerning the AGN and therefore the ionizing nuclear source cannot be made in Compton-thick galaxies where the column density exceeds $N_H < 10^{24}\,\mathrm{cm}^{-2}$ (Fraquelli et al., 2003)(see sections 5.3 and 5.5 for more on this problem).

As seen in the [OIII] image in Fig. 5.15, ionized gas is observed as an extended emission from the central parsecs of the galaxy out to about 2 kpc distance. This feature is also seen in Hβ images, but not as prominent. As a result the gradient (Fig. 5.17) exhibits a second rise, at the edge of the galaxy. This feature has been observed in narrow-band images before (Mulchaey et al., 1996) and sometimes exhibits cone-shaped morphologies (Storchi-Bergmann et al., 1992). This extended ionized gas is now called the extended narrow-line region (ENLR). The inner part, the NLR shows kinematic signatures of interactions, either with the plasma emitting in the radio regime or with accretion disc winds that would be present in galaxies with outflows (Crenshaw et al., 2000). The gas of the ENLR rotates with similar or same velocities as within the galaxy and could therefore be ionized by the AGN (Peterson, 1997) with photoionization seemingly being the main mechanism responsible for this emission (Morse et al., 1996).

Fraquelli et al. (2003) have found the [OIII] surface luminosity distribution more centrally peaked than the luminosities of $[OII]\lambda3727$ and Hα. The excitation is therefore higher closer to the nucleus while the ionization parameter seen by the gas decreases with radius. This is amplified by possible H II regions in the disc. They furthermore calculated the mass of the NLR of Mrk 607 to be $56 \times 10^3 M_\odot$, of a total mass of $639 \times 10^3 M_\odot$.

Mrk 607 (NGC 1320) and the second galaxy of the pair, NGC 1321, show similar radial velocities: 2663 $\mathrm{km\,s^{-1}}$ and 2848 $\mathrm{km\,s^{-1}}$ respectively. An interaction in the future is therefore expected and ongoing star formation in this area is very likely. Nevertheless, no decrease in $[OIII]\lambda5007/H\beta$ can be measured. The conclusion

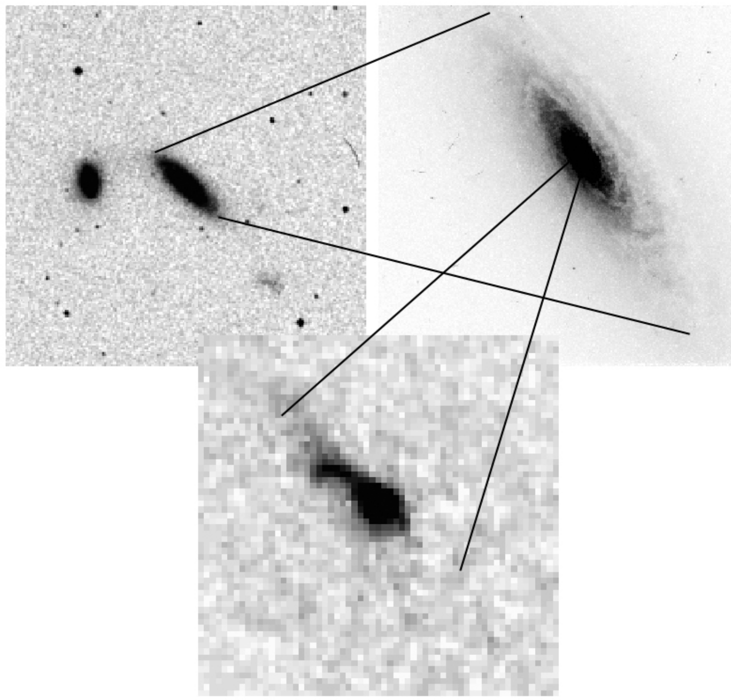

Figure 5.15: Composite of images from Mrk 607. Upper left: an image taken with the UKSchmidt telescope at 4680$\AA$, at an image size of 6.0x6.0 arcmin the second galaxy of the pair, NGC 1321, is visible. Upper right: a HST image at 6030$\AA$, with 0.6x0.6 arcmin. The lower panel shows an image from the HST WFPC2 camera taken at [OIII], 5007$\AA$. The image size is 0.1x0.1 arcmin.

that comes to mind is that the pair has not experienced real interaction yet.
A logical interpretation of the lack of decrease is, that because of the obscured central regions in Sy 2 galaxies, an analysis of the central region is simply not possible or yields faulty measurements. The information taken from [OIII]/Hβ first and foremost provides information of the radiation field and without better knowledge of the ongoings in the BLR as well as complete information of the other two lines used for the BPT diagram ([NII] and Hα), no further assumptions can

be made at this point concerning the nucleus and BLR. Infrared observations help reduce dust features, but the obscured AGN will be buried, even in observations at energies up to 10 keV. Only when the AGN is observed along teh ENLR line of sight, most of the hard X-rays emerge unobscured and observations can be compared to Sy 1 galaxies (Fraquelli et al., 2003). For further complications concerning Sy 2 galaxies, and estimations of X-ray luminosities, see 5.5. Nevertheless, the presented data fosters the idea of an obscuring torus in Seyfert 2 galaxies, although the question still remains how thick this torus is. This particular galaxy further shows interesting, extended feature of the ionized gas that stretches over $\pm 6''$ of the galaxy (see also extracted spectra of Mrk 607 in the right panels of Fig. 5.18).
A comparison of the two types of galaxies as surface plots (Fig. 5.16) clearly shows the difference in $log[OIII]/H\beta$: In the Sy 1 galaxy a ring around the central region is clearly visible – although boosted by the simplification of the simple Gauss fit – and the theory of looking directly into the active nucleus in this type of galaxy is confirmed. The nucleus of the Sy 2 galaxy presents itself hidden to the observer of the optical range. A further analysis is therefore not possible. The intensely colored regions in the images stem from noise that is falsely picked up as emission or absorption by the measuring algorithm. They are not part of the strongly emitting central regions of the galaxies.

5.4 Spectroscopic characterization as a comparison of Sy 1 and Sy 2

In order to look at the spectra extracted from the reduced datacubes, a set of spectra is taken from different parts of the galaxies for each object (see fig. 5.18). These two objects are representative of the discussed peculiarities of the two different types of Seyfert galaxies. The spectra of UGC 1935 shows rather strong emission from the optical Fe II bump compared to the spectra of the Sy 2 galaxy Mrk 607 as well as strong and prominent [OIII] doublet lines and a very broad $H\beta$ line. The broad emission lines originate from the broad line region surrounding the center. In the lower panels where emission from outer regions is depicted, the $H\beta$ line of the Sy 1 galaxy loses it's importance. As expected, Mrk 607 shows a narrow, smaller $H\beta$ emission and very strong [OIII]$\lambda\lambda 4960, 5007$ emission lines. $H\gamma$ is only visible in the Sy 1 galaxy on the left. The ENLR of the Sy 2 galaxy

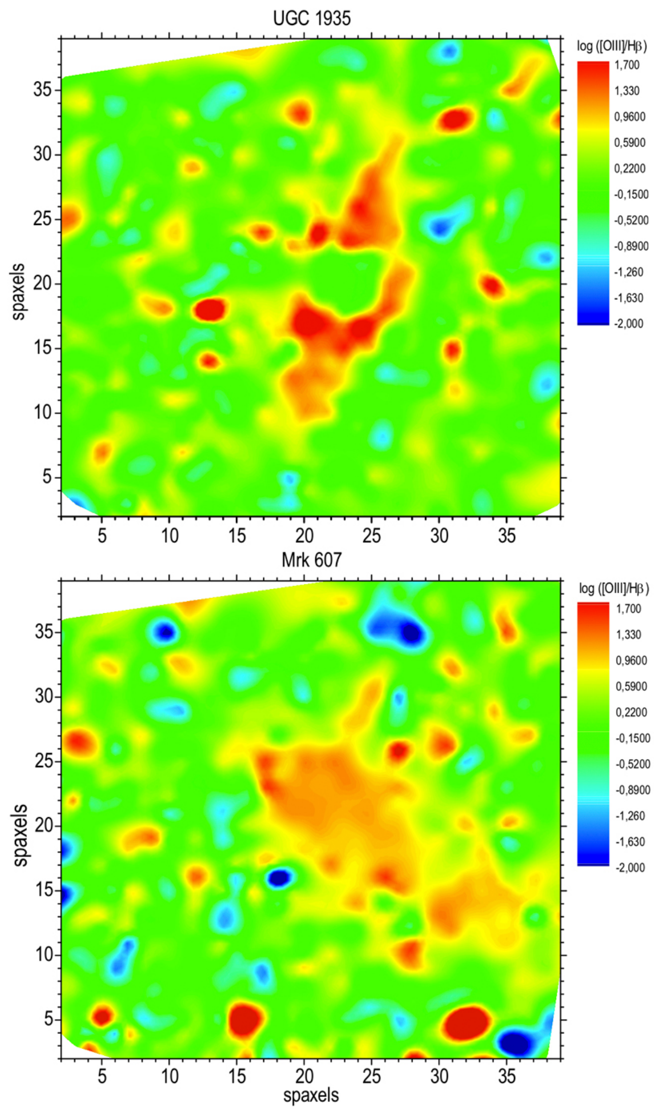

Figure 5.16: Comparison of surface plots of the two types of galaxies, up: Sy 1 UGC 1935, down: Sy 2 Mrk 607. Very bright spots are due to miss-measurements of noise of the measuring algorithm.

can be inspected on the right. The lines are stronger compared to the Sy 1 galaxy, even at greater distances from the nucleus.

The intensities of the [OIII] emission lines of both types of galaxies are more stable

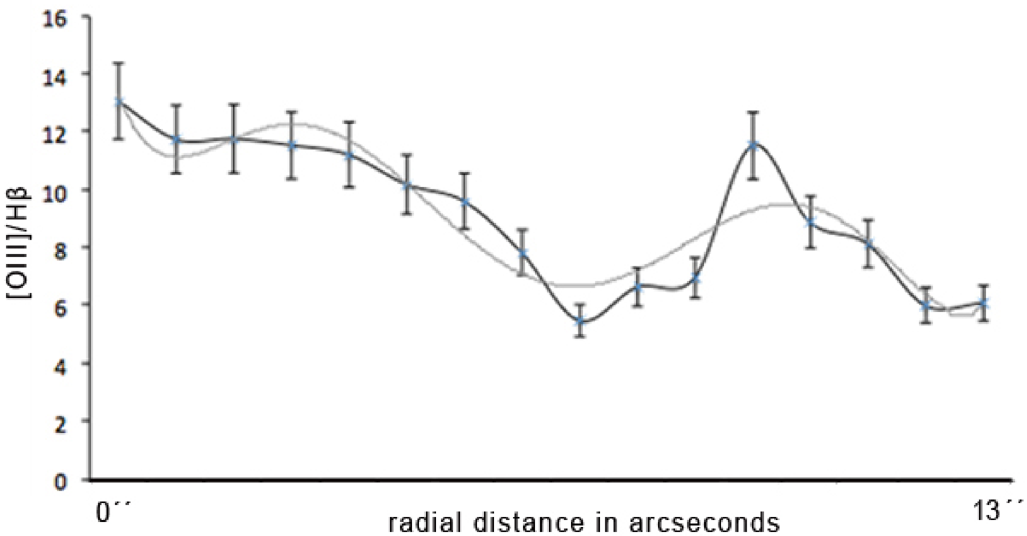

Figure 5.17: Graph of the averaged radial values of [OIII]/Hβ along the major axis of Mrk 607 shown in arcseconds. A polynomial is presented in light grey. The second rise indicates the peak of the ENLR common for Sy 2s. Because of the hidden BLR no adequate information can be drawn from the central regions.

compared to Hβ lines. This can be seen throughout the galaxies and the decrease is not as rapid as in the $H\beta$ lines. The [OIII] emission therefore arises from all areas, the innermost region to an extended emission line region (EELR), which is common in objects with weak FeII and strong [OIII] emission. The origin of these extended line regions is not clear yet, possibly ram pressure stripping can be made responsible (Yoshida et al., 2004).

The profiles change drastically. Furthermore, a broad blue-shifted component, a "blue wing "is present in both measured emission lines, the [OIII] and – obviously more noticeable – in the $H\beta$ line profiles. This feature is not only visible in the galactic center, but is extended, suggesting that the broadening could be due to other meanings than the simple rotating disk which is usually not that large, but maybe rather clouds or filaments.

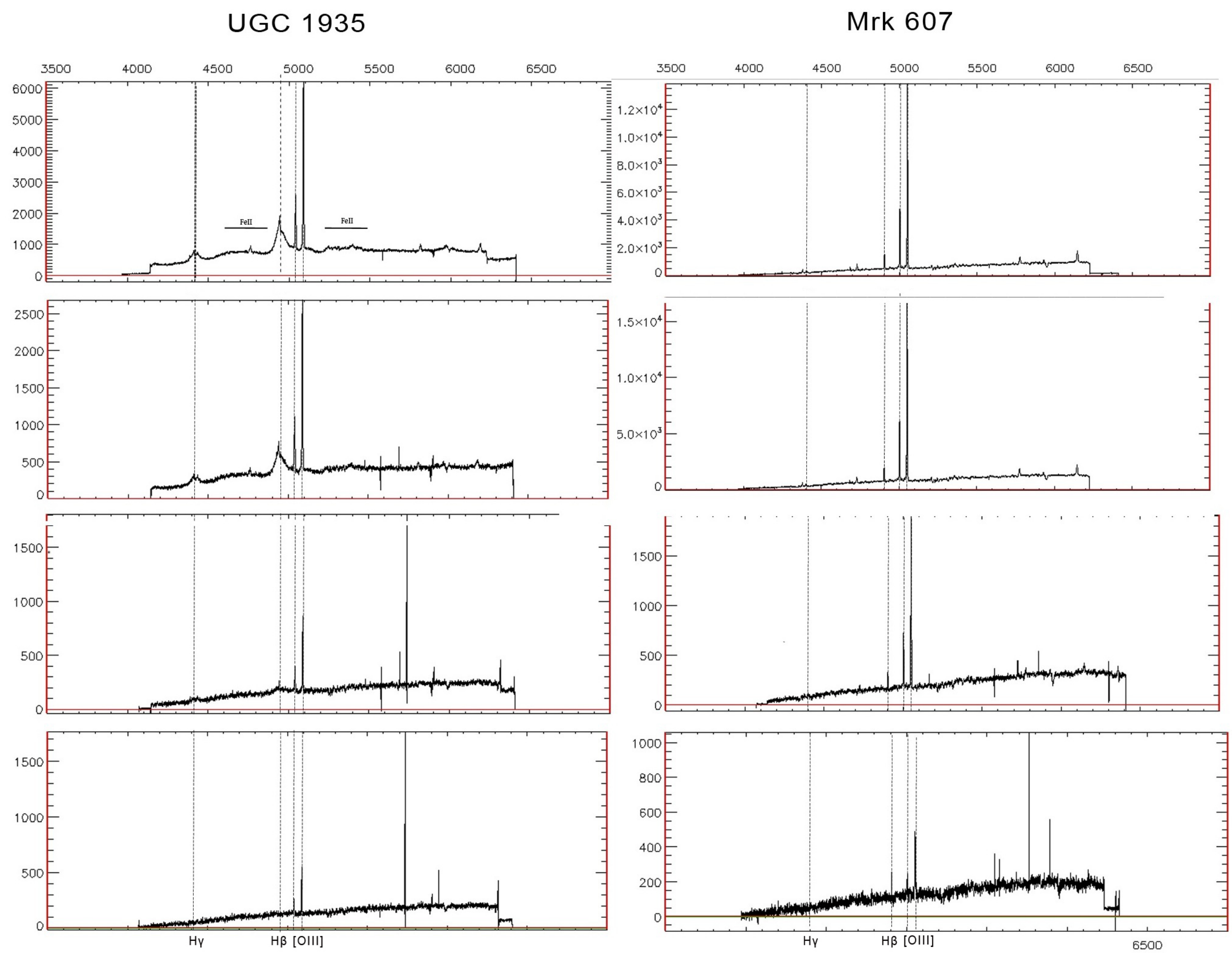

Figure 5.18: Extracted spectra from the original datacube of UGC 1935 (left) and Mrk 607 (right). The spectra location increase outwards from center to vicinity from top to bottom. Prominent emission lines are labeled by dashed lines. CCD artefacts and telluric absorption can be seen as well.

5.5 Information from Photometry

The spectral energy distribution of UGC 1935 (taken from NED, the NASA/IPAC Extragalactic Database, Fig. 5.19) is characteristic for an active galaxy of type 1. The flat distribution indicates that there is much more emission at higher energies, X-ray wavelengths and in the UV.

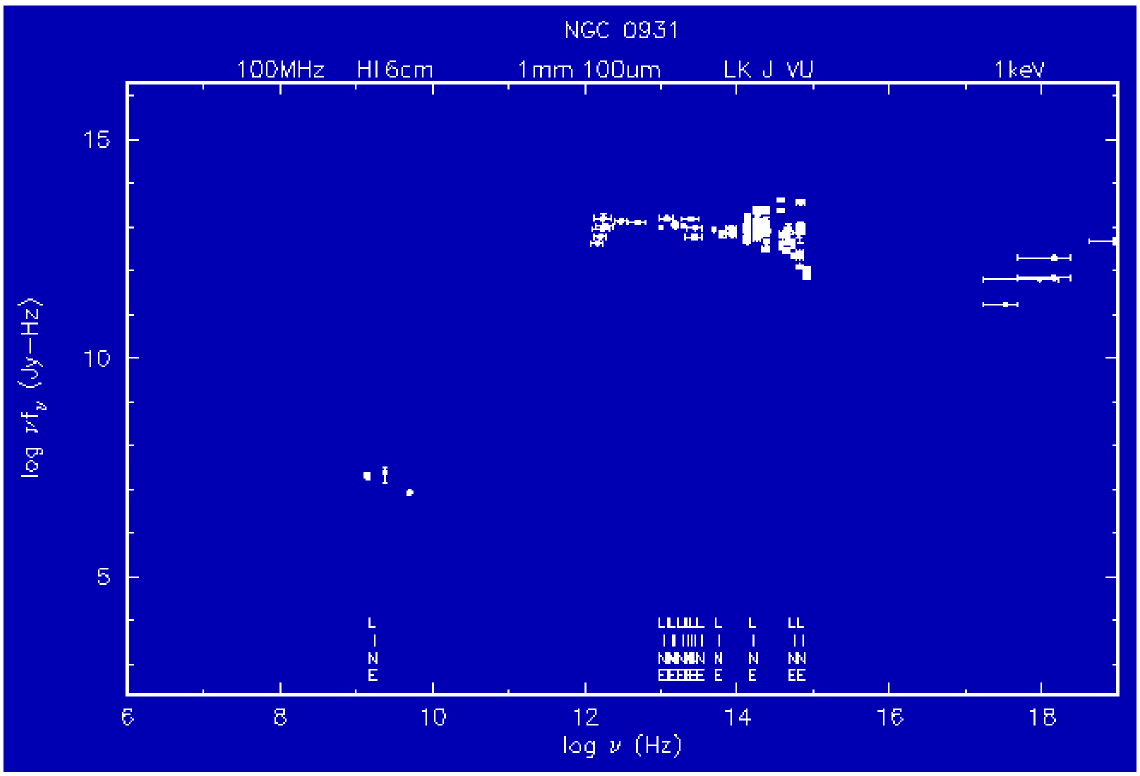

Figure 5.19: Spectral Energy Distribution of UGC 1935, taken from the NASA/IPAC Extragalactic Database.

The infrared and UV regions are remarkably similar in different AGNs. The mean radio-soft X-ray spectral energy distribution seen in Fig. 5.19 shows the standard features of an AGN SED: generally speaking, AGN emit similar energy at most parts of the electromagnetic spectrum, except for radio loud quasars. The measurements were taken with a number of instruments for the NED research, concentrating on the areas in the Johnson filter system in the visible and near-infrared, U, B, V, R, I, H, K, L as well as 2MASS data. The UV Bump is clearly

visible at UGC 1935, followed by a characteristic gap and the X components with greater errors. The bump is proceeded by an inflection, indicating a minimum in the energy output. This inflection also demonstrates the peak of starlight disposal in the host galaxy. For UGC 1935, this host galaxy contribution approximately equals the emission of the AGN. This is the reason for the relatively flat SED that can be seen here. The UV bump or “big blue bump”(BBB) is particularly important because this area of UV emission is the source of most ionizing photons. If the spectra of UGC 1935 had gone further into lower wavelength ranges, a clear change in continuum slope would have been noticeable. (See Zheng et al. (1997) for more information about this.)
The big blue bump, prominent at $14.5 \leq \log \nu(\mathrm{Hz}) \leq 16.5$ (Elvis et al., 1994) in high-luminosity AGNs, is less clear in Mrk 607 because observations are not possible at these wavelengths (see Fig. 5.20).

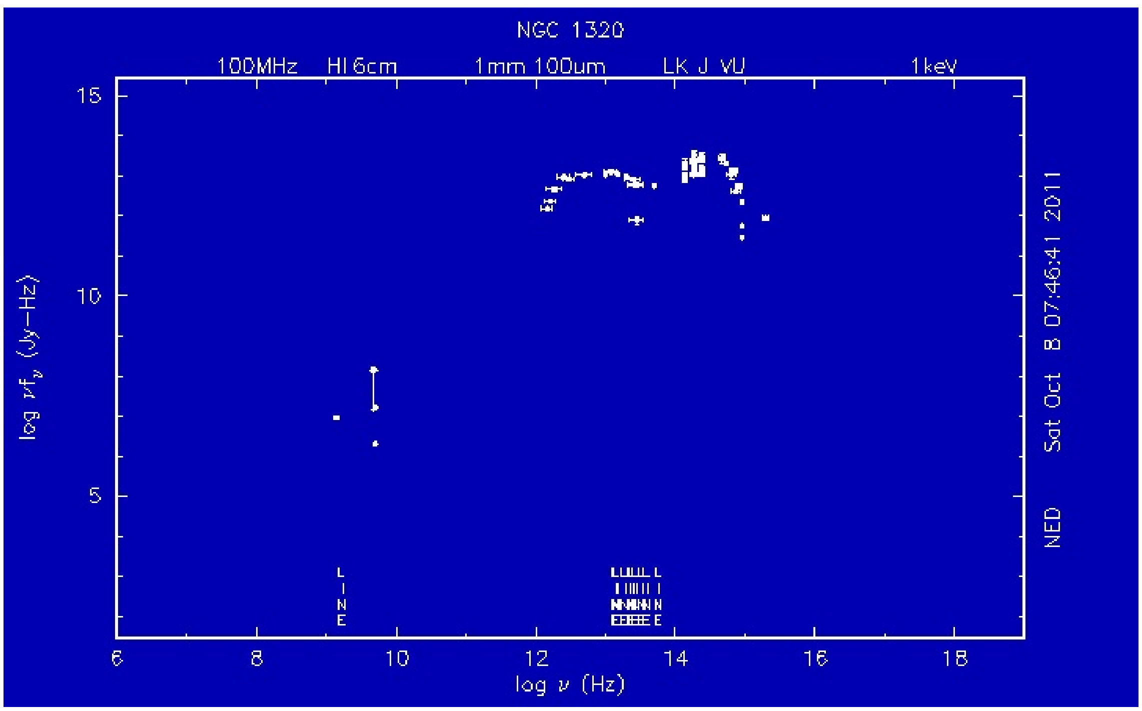

Figure 5.20: Spectral Energy Distribution of Mrk 607, taken from the NASA/IPAC Extragalactic Database.

In Seyfert 2s, much of the high energy flux gets absorbed either by the material

of the dusty torus described by the unified model scenario, or other gas in these galaxies (Fraquelli et al., 2003). The part of the SED in X-rays should therefore not emerge unless the column densities are very low. Higher frequency datapoints are therefore absent in 5.20. Predictions of the X-ray values are possible when the AGN is modeled as a power law and its contribution absorbed by the Galactic column density only. In cases for lower column densities, the AGN is directly detected at high energies. In this case, Fraquelli et al. (2003) find that the spectral extrapolation from the optical and UV provide a good estimation. In Compton-thick galaxies with higher column densities like Mrk 607, the buried AGN is not directly measured and the luminosities are caused by the scattered component and not related to the total output of the central engine. They calculate a predicted luminosity in intrinsic X-ray emission of 43.96 erg s^{-1} for Mrk 607.
The origin of the big blue bump in AGN is still under debate. A likely explanation that would fit into the models that have been done so far, is that the emission stems from the optically thick, geometrically thin accretion disk (Wilkes, 1999). That the accretion disk itself is a strong contributor to the energy output is not surprising since it is powered by the central SmBH. Nevertheless, not all questions are answered and predictions from models concerning different types of emission and absorption cannot yet be confirmed with observations. In lower luminosity galaxies like the Seyfert galaxy UGC 1935 portrayed here, this is the reason why the IR bumps appears to be so weak. The near-IR bump generally peaks at $\sim 25-60\,\mu$m, but is not very prominent here (see Fig. 5.19). The typical cutoff lies at about $100\,\mu$m and 1 mm, where a sharp drop to much lower observation points is noticeable. This drop off is believed to underline the theory of thermal emission from cool dust dominating the FIR region of the SED. Non-thermal synchrotron emission cannot produce slopes that are $\alpha_{\rm FIR} > 2.5$, while the measured cut-offs this value almost double. Radio quiet quasars, like the Seyfert galaxy UGC 1935 are object bright in the FIR and low in redshift (Wilkes, 1999).
The observed UV, optical and IR luminosity is the result of the reprocessing of accretion energies radiated as X-rays and γ-rays. These effects can be seen in the X-ray spectrum of Sy 1s ($\sim 0.1 - 100\,$keV), which can be well reproduced by a power-law form with a slope $\alpha_x \sim 1-2$ and $F_\nu \propto \nu^{-\alpha_{\rm x}}$)(Wilkes, 1999; Reynolds, 1997). This is suggested to be photoionized material in the center of the object, due to its high ionization state. For the radio quiet galaxy UGC 1935, the galactic line-of-sight absorption ($7.07 \times 10^{20}\,{\rm cm}^{-2}$; (Elvis et al., 1989)), is so great that exact measurements of the complex soft emission is unclear (Reynolds, 1997).

Narrow Line Seyfert 1's like UGC 1935 are classified due to their properties of their spectra. The SED of a NLSy1 shows a strong, hot BBB and a steep soft X-ray slope. Both the slope in soft X-ray as well as a more prominent BBB cannot be confirmed here

5.6 Discussion

Integralfield spectroscopy is without doubt the future of spectroscopy, replacing long slit spectroscopy where longer and more difficult setups are needed. Nevertheless should other possibilities to obtain information about emission in certain lines be taken into account at this place. Instrumentation is still scarce compared to simple photometric setups, which gives rise to a simple comparison between gaining excess to emission line information through IFS and photometry. If certain parameters and requirements are fulfilled, photometry can be used for investigation of emission line information.

Thanks to modern instrumentation, element abundances at all redshifts can now be measured using both emission and absorption lines. Quasars and AGNs are far away and therefore ideal to probe abundances in the early universe. Derivation of abundances from emission lines using AGN turns out to be rather difficult though due to the broadening of lines. The width of the lines complicates the measurement and the high electron density in the BLR as well as the large optical depths make analysis delicate (Shields, 2000) and more sophisticated tools are needed.

Nonetheless, a first indication to the abundance ratios can be given with the less sensitive relative abundances of C, N, and O to the uncertainty in the electron temperature as stated in Shields (1976). He further writes, that the N/O and N/C ratios can be used as an indicator of the overall metallicity, given the secondary nature of nitrogen production. Due to the nature of the blue grism that was used for these observations, it was not possible to extract intensities for the nitrogen line. Shields (1976) found high N/C in two QSOs and suggested similar results to be found in nearby normal galactic nuclei and active nuclei. Investigations of abundances lead to the assumption that the gradient in O/H lead to a similar gradient in N/O since nitrogen is mostly a secondary product (Talbot & Arnett, 1974).

With all the drawbacks mentioned above, temperature fluctuations along the line-of-sight, first described by Peimbert (1967), should not be left out to mention. When an abundance ratio is based upon a forbidden/permitted line ratio such as the $[OIII]\lambda5007/H\beta$ ratio, the measured overestimation of the electron temperature causes an underestimate in the end. Abundances from permitted/permitted ratios are therefore systematically higher.

As already graphically shown by Köppen & Edmunds (1999), infalling material from low-metallicity areas dilutes the galaxy's ISM with fresh gas from the outskirts. The metallicity drops if the rate is higher than the star formation rate which would enrich the ISM and no effect would be seen. The effective yield of a galaxy depicts the difference between the measured metallicity of a galaxy compared to what would be expected if the galaxy had evolved as a closed-box model, i.e. without in- or outflows. It is needless to say that this does not happen in reality and especially not in the case of a mass and gas-rich system that is in interaction with a companion galaxy like the one studied here. As adequately explained, the galaxy is constantly undergoing chemical and kinematical evolution. Since the production of oxygen is dominated by winds and SN, promt return of oxygen can be assumed (Dalcanton, 2007). The effective yield

$$y_{\text{eff}} \equiv \frac{Z_{\text{gas}}}{ln(1/f_{\text{gas}})} \tag{5.6.1}$$

is therefore only constant for a galaxy in a closed-box system. According to Dalcanton (2007), if any gas has entered or left the galaxy, as would be the case in a merger like the one observed, the effective yield will drop as the metallcity and gas fraction, Z_{gas} and f_{gas} will change.

Following Dalcanton (2007)'s reasoning, when trying to understand whether outflows or infalls suggested by the spectra analysis, are possible, gas flows must have reduced the effective yield. It shall be noted that the effective yield is in fact independent of how much gas is in the system:

$$y_{\text{eff}} \approx \frac{M_{\text{Z}}}{M_{\text{stars}}} \tag{5.6.2}$$

Therefore, accretion of new, metal-poor gas does not change the effective yield of the gas-rich galaxy by much, which means the galaxy would evolve as if measured for a closed box model. In this theoretical model, the decrease in metallicty of the system also increases the gas richness and the relationship between Z_{gas} and f_{gas} should stay the same, just as in a closed-box system. Metal-rich outflows on the other hand will have an impact on this ratio and will therefore change the effective yield. This is due to the fact that the effective yield is linear with the mass of metals in the gas phase. Considering the very likely gas outflow from the system UGC 1935 and the impact on the galaxy's effective yield, it is useful to define the mass of gas lost due to outflow as ΔM_{gas} and the mass of metals lost as ΔM_{Z}. The metallicty of the outflow is then

$$Z_{\text{outflow}} = \frac{\Delta M_{\mathrm{Z}}}{\Delta M_{\text{gas}}}. \tag{5.6.3}$$

The outflow metallicity is parametrized by (Dalcanton, 2007) as a multiple x of the gas phase metallicity at the time of outflow:

$$x \equiv \frac{Z_{\text{outflow}}}{Z_{\text{gas}}} \tag{5.6.4}$$

This value can be constrained observationally through abundance analysis of X-ray spectroscopy of the hot gas, or, theoretically, through the mass fraction of the wind. The description of x for a realistic AGN-driven outflow, as well as a SN wind, can be divided into "unenriched outflows"and "enriched outflows", the latter being more relevant for the AGN winds discussed here. The wind is dominated by freshly produced metals and is very likely to be periodic, just as gas accretion too. Therefore, the chemical evolution of the galaxy is very likely a series of periods of closed-box evolution followed by outflows and accretions (Marlowe et al., 1995). This suggests that the effective yields will change too. The true nucleosynthetic yield during the closed-box evolution holds for on-going star formation (Köppen & Hensler, 2005). Gas rich-spirals are likely to have had metal-enriched winds in their past resulting reductions of their effective yield. To summerize, metal-enriched outflows like the one likely to be happening in UGC1935, seem to be the only mechanisms capable of reducing the effective yield by a significant amount (see again Dalcanton (2007) for details).
Since it is unknown wether the outflows of AGNs are produced by the active nucleus of the galaxy alone or by star formation activity, a more comprehensive study of the galaxy is needed. Large scale outflows seem to be common amongst Seyfert galaxies (Robitaille et al., 2007). Galaxies that show higher star formation rates and warmer dust are more prone to show outflows. Star formation in turn is a common side effect of interacting galaxies like the one studied here.

The galaxy investigated in [OIII] shows a different ionizing contribution than $H\alpha$ for instance, showing stellar radiation. [OIII] presents a hard power-law as an excitation mechanism. A comparison with narrowband emission maps in [OIII] by Robitaille et al. (2007) confirms the results that the nucleus of UGC 1935 is a strong [OIII] emitter. They also describe a possible ring-like structure of radius 20″ (6.5 kpc) in $H\alpha$.
The main question thus remains, is the interaction between UGC 1935 and it's companion triggering the AGN activity? And if so, why then are AGN observed in numerous galaxies without pairs?While integralfield spectroscopy makes it possible to follow trends within this one galaxy and infer from the given data possible scenarios, it is without doubt important to have a look at the statistics concerning a greater number of galaxies. Keel et al. (1985) found an excess of Seyfert nuclei while investigating galaxy pairs. But it is very likely that more parameters than just being paired galaxies need to be taken into account. Maybe the triggering of an active nucleus only happens in a certain stage of encounter, e.g. after first pericenter. Some studies suggest that type 1 and type 2 Seyfert galaxies need to be treaded independently (Laurikainen & Salo, 1995), which, given the study of both types, I can enforce. Maybe the schematics in explaining the difference with varying viewing angles is not the right one, but instead, different environments lead to different results. Unfortunately, statistical approaches of investigating whether AGN are indeed the result of interactions are less frugal than desired as stressed by some (e.g. Heckman, 1990). Which brings us back to investigating individual galaxies in more detail, also to have a chance in physically understanding the process of *how* this would happen. For the given individual Sy 1 galaxy, both morphology and kinematics show evidence for interaction and additionally, for infalling material which can be very likely responsible for triggering or fuelling the active nucleus. The galaxy's dynamics and tidal features give a sense of motion within the galaxy and the rotation curve gives small regions of peculiar motions. Since the active nucleus is hidden from view in Sy 2 galaxies like Mrk 607 studied here, only information from narrow line and extended narrow line regions can be analyzed. It has been explained that predictions about metallicities through emission lines in the central regions are at least delicate, more likely less significant and concealed to us. The given observations used for this study of Seyfert galaxies does not allow further predictions concerning this galaxy.

Conclusion & Summary

Only a few Seyfert galaxies have been studied in [OIII] in the past (e.g. Pogge, 1988; Veilleux et al., 1999; Yoshida et al., 2004; Veilleux et al., 2003). The present observations of the type 1.5 Seyfert galaxy UGC 1935 (Mrk 1040) and type 2 Seyfert galaxy Mrk 607 reveal spectra of several important emission lines. The integralfield spectrograph VIMOS that was used for this purpose, renders possible a three dimensional look not only along a specific axis but all across the covered region enabling the study of outflows, infalls and velocities.
The aim of this work was to clearly understand the ongoings and advantages of 3D spectroscopy and apply these insights to collect arguments for an inwards decreasing metallicity gradient in interacting active galaxies. Several possible consequences of this infalling material, that would ultimately fuel the central SmBH have been looked at: out- and infalls, bars and rotating cores.
Differences of Sy 1 (UGC 1935) and Sy 2 (Mrk 607) galaxies have been presented with the help of spectroscopic means. The resulting conclusion from the two studied galaxies shows that UGC 1935, where an interaction has been confirmed before (Kuo et al., 2008), exhibits a decrease in the O/H gradient towards central areas. The second studied galaxy, Mrk 607 does not show this phenomenon but illustrates an increasing gradient as expected from a normal galaxy. Mrk 607, even though part of a group of galaxies, does not yet seem to be involved in interactions. Seyfert 2 galaxies hold an additional complexity because of the dusty torus obscuring the AGN. This theory of the unified model was confirmed here and predictions involving emission lines can only be made in the NLR and ENLR. Emission from Sy 2 galaxies therefore give information of the radiation field rather than the ionizing source. The question how such an analysis can be made possible in a Sy 2 galaxy still remains. Since the dust torus obscures the AGN and therefore does not allow a direct few into the BLR, important information that cannot be collected directly otherwise gets lost. Observational data like the ones presented here, are not sufficient to address many questions concerning metallicities in the center of this type. Nevertheless a look into the radiation field of this galaxy was presented and an analysis – with the means given by optical data –

performed.
To gain further and a more comprehensive portrait of AGNs in general, observations in other wavelength ranges, especially the IR, overcoming some problems of reddening that can be attributed to dust, as well as higher energy regimes, are necessary. On the way to fully understand the different types of AGNs, and the accretion of their material into the center, spectroscopical and photometrical observations in all wavelength ranges and a large sample of galaxies for statistical means are needed.
The addressed issues are the starting point to a longer investigation of galaxy environments and the role of the AGN in interactions and group environments. The advantages of 3D spectroscopy in this observational field of study have been clearly explained and will now have to be used to a greater extend. The combination of spectroscopic and photometrical means to study star formation and AGN activity as a function of morphological type, stellar mass and environmental density will help to find answers to some of astrophysics most intriguing questions.

Bibliography

Afanasev, V. L. 1981, Soviet Astronomy Letters, 7, 215

Afanas'ev, V. L. & Fridman, A. M. 1993, Astronomy Letters, 19, 319

Afflerbach, A., Churchwell, E., & Werner, M. W. 1997, ApJ, 478, 190

Aller, L. H. 1942, ApJ, 95, 52

Allington-Smith, J. 2006, NewAR, 50, 244

Allington-Smith, J. 2007, in Science Perspectives for 3D Spectroscopy, ed. M. Kissler-Patig, J. R. Walsh, & M. M. Roth, 3–540

Allington-Smith, J. & Content, R. 1998, PASP, 110, 1216

Alloin, D., Collin-Souffrin, S., Joly, M., & Vigroux, L. 1979, A&A, 78, 200

Alloin, D., Pelat, D., Boksenberg, A., & Sargent, W. L. W. 1983, ApJ, 275, 493

Amram, P., Marcelin, M., Bonnarel, F., et al. 1992, A&A, 263, 69

Antonucci, R. R. J. & Miller, J. S. 1985, ApJ, 297, 621

Arp, H. 1966, ApJS, 14, 1

Arp, H. C. & Madore, B. F. 1975, The Observatory, 95, 212

Arribas, S., Carter, D., Cavaller, L., et al. 1998, in Presented at the Society of Photo-Optical Instrumentation Engineers (SPIE) Conference, Vol. 3355, Society of Photo-Optical Instrumentation Engineers (SPIE) Conference Series, ed. S. D'Odorico, 821–827

Arribas, S., Mediavilla, E., & Rasilla, J. L. 1991, ApJ, 369, 260

Audouze, J. & Tinsley, B. M. 1976, ARA&A, 14, 43

Bacon, R. 1995, in Astronomical Society of the Pacific Conference Series, Vol. 71, IAU Colloq. 149: Tridimensional Optical Spectroscopic Methods in Astrophysics, ed. G. Comte & M. Marcelin, 239–+

Bacon, R., Copin, Y., Monnet, G., et al. 2001, MNRAS, 326, 23

Baldwin, J. A., Phillips, M. M., & Terlevich, R. 1981, PASP, 93, 5

Barnes, J. E. & Hernquist, L. 1996, ApJ, 471, 115

Basu, D. 1994, Ap&SS, 222, 91

Becker, R. H., White, R. L., & Helfand, D. J. 1995, ApJ, 450, 559

Bennett, A. S. 1962, MmRAS, 68, 163

Blandford, R. D., Netzer, H., Woltjer, L., Courvoisier, T., & Mayor, M., eds. 1990, Active Galactic Nuclei

Brandt, W. N., Alexander, D. M., Bauer, F. E., & Hornschemeier, A. E. 2002, Royal Society of London Philosophical Transactions Series A, 360, 2057

Canalizo, G. & Stockton, A. 2001, ApJ, 555, 719

Cappelluti, N., Brusa, M., Hasinger, G., et al. 2009, A&A, 497, 635

Colbert, E. J. M., Baum, S. A., Gallimore, J. F., et al. 1996, ApJS, 105, 75

Colless, M., Dalton, G., Maddox, S., et al. 2001, MNRAS, 328, 1039

Copetti, M. V. F., Dottori, H. A., & Pastoriza, M. G. 1986, , 12, 137

Crenshaw, D. M., Kraemer, S. B., & Gabel, J. R. 2003, AJ, 126, 1690

Crenshaw, D. M., Kraemer, S. B., Hutchings, J. B., et al. 2000, AJ, 120, 1731

Croom, S., Boyle, B., Shanks, T., et al. 2004, in Multiwavelength AGN Surveys, ed. R. Mújica & R. Maiolino, 57–62

Dalcanton, J. J. 2007, ApJ, 658, 941

Di Matteo, P., Pipino, A., Lehnert, M. D., Combes, F., & Semelin, B. 2009, A&A, 499, 427

Dutil, Y. & Roy, J.-R. 1999, ApJ, 516, 62

Edge, D. O., Shakeshaft, J. R., McAdam, W. B., Baldwin, J. E., & Archer, S. 1959, MmRAS, 68, 37

Edmunds, M. G. 1990, MNRAS, 246, 678

Elvis, M., Lockman, F. J., & Fassnacht, C. 1994, ApJS, 95, 413

Elvis, M., Wilkes, B. J., & Lockman, F. J. 1989, AJ, 97, 777

Emsellem, E. 2007, in Science Perspectives for 3D Spectroscopy, ed. M. Kissler-Patig, J. R. Walsh, & M. M. Roth, 83–+

Ferland, G. J. & Osterbrock, D. E. 1986, ApJ, 300, 658

Fiore, F. 2004, in Multiwavelength AGN Surveys, ed. R. Mújica & R. Maiolino, 11–16

Fischer, T., Crenshaw, M. D., Kraemer, S. B., & Schmitt, H. R. 2011, in Narrow-Line Seyfert 1 Galaxies and their Place in the Universe

Fraquelli, H. A., Storchi-Bergmann, T., & Levenson, N. A. 2003, MNRAS, 341, 449

Garcia, A. M. 1993, A&AS, 100, 47

Garilli, B., Franzetti, P., Paioro, L., Scodeggio, M., & Zanichelli, A. 2004, ArXiv Astrophysics e-prints

Garnett, D. R. 1998, in Astronomical Society of the Pacific Conference Series, Vol. 147, Abundance Profiles: Diagnostic Tools for Galaxy History, ed. D. Friedli, M. Edmunds, C. Robert, & L. Drissen, 78–+

Garnett, D. R. & Shields, G. A. 1987, ApJ, 317, 82

Gregory, P. C., Scott, W. K., Douglas, K., & Condon, J. J. 1996, ApJS, 103, 427

Griffiths, R. E., Knudson, A., & Miyaji, T. 2004, in Multiwavelength AGN Surveys, ed. R. Mújica & R. Maiolino, 29–32

Heckman, T. M. 1980, A&A, 87, 152

Heckman, T. M. 1990, in NASA Conference Publication, Vol. 3098, NASA Conference Publication, ed. J. W. Sulentic, W. C. Keel, & C. M. Telesco, 359–382

Henry, R. B. C., Balkowski, C., Cayatte, V., Edmunds, M. G., & Pagel, B. E. J. 1996, MNRAS, 283, 635

Henry, R. B. C. & Worthey, G. 1999, PASP, 111, 919

Hickson, P., Kindl, E., & Auman, J. R. 1989, ApJS, 70, 687

Ho, L. C., Filippenko, A. V., & Sargent, W. L. W. 1993, ApJ, 417, 63

Ho, L. C., Filippenko, A. V., & Sargent, W. L. W. 1997, ApJS, 112, 315

Holmberg, E. 1941, ApJ, 94, 385

Horne, K. 1986, PASP, 98, 609

Ivezić, Ž., Siverd, R. J., Steinhardt, W., et al. 2004, in Multiwavelength AGN Surveys, ed. R. Mújica & R. Maiolino, 53–56

Jackson, C. A. & Wall, J. V. 1999, MNRAS, 304, 160

Jahnke, K., Wisotzki, L., Sánchez, S. F., et al. 2004, Astronomische Nachrichten, 325, 128

Jogee, S., Barazza, F. D., Rix, H., et al. 2004, ApJ, 615, L105

Jones, M. H. & Lambourne, R. J. A. 2004, An Introduction to Galaxies and Cosmology, ed. Jones, M. H. & Lambourne, R. J. A.

Keel, W. C., Kennicutt, Jr., R. C., Hummel, E., & van der Hulst, J. M. 1985, AJ, 90, 708

Kennicutt, Jr., R. C. & Kent, S. M. 1983, AJ, 88, 1094

Kewley, L. J., Geller, M. J., & Barton, E. J. 2006a, AJ, 131, 2004

Kewley, L. J., Groves, B., Kauffmann, G., & Heckman, T. 2006b, MNRAS, 372, 961

Khachikian, E. Y. & Weedman, D. W. 1974, ApJ, 192, 581

Köppen, J. & Edmunds, M. G. 1999, MNRAS, 306, 317

Köppen, J. & Hensler, G. 2005, A&A, 434, 531

Krolik, J. H. 1999, Active galactic nuclei : from the central black hole to the galactic environment, ed. Krolik, J. H.

Kuo, C.-Y., Lim, J., Tang, Y.-W., & Ho, P. T. P. 2008, ApJ, 679, 1047

Kuźmicz, Jamrozy, M. A. 2009, in Young Scientists 16th Proceedings, ed. V. Y. Choliy & G. Ivashchenko, 46–48

Larson, R. B. 1972, Nature, 236, 7

Laurikainen, E. & Salo, H. 1995, A&A, 293, 683

Le Fèvre, O., Vettolani, G., Garilli, B., et al. 2005, in SF2A-2005: Semaine de l'Astrophysique Francaise, ed. F. Casoli, T. Contini, J. M. Hameury, & L. Pagani, 19–+

Lequeux, J., Maucherat-Joubert, M., Deharveng, J. M., & Kunth, D. 1981, A&A, 103, 305

Lequeux, J., Peimbert, M., Rayo, J. F., Serrano, A., & Torres-Peimbert, S. 1979, A&A, 80, 155

Maciejewski, W. & Binney, J. 2001, MNRAS, 323, 831

Markarian, B. E., Lipovetskii, V. A., & Stepanian, D. A. 1977, Astrofizika, 13, 397

Marlowe, A. T., Heckman, T. M., Wyse, R. F. G., & Schommer, R. 1995, ApJ, 438, 563

Márquez, I. & Masegosa, J. 2008, in Revista Mexicana de Astronomia y Astrofisica Conference Series, Vol. 32, Revista Mexicana de Astronomia y Astrofisica Conference Series, 150–154

Márquez, I., Masegosa, J., Moles, M., et al. 2003, Ap&SS, 284, 711

Martin, P. & Roy, J.-R. 1994, ApJ, 424, 599

Mathur, S., Kuraszkiewicz, J., & Czerny, B. 2001, , 6, 321

Matthews, T. A. & Sandage, A. R. 1963, ApJ, 138, 30

McCall, M. L. 1982, PhD thesis, THE UNIVERSITY OF TEXAS AT AUSTIN.

McGaugh, S. S. 1991, ApJ, 380, 140

McGaugh, S. S. 1994, ApJ, 426, 135

Mihos, J. C. & Hernquist, L. 1996, ApJ, 464, 641

Morse, J. A., Raymond, J. C., & Wilson, A. S. 1996, PASP, 108, 426

Mújica, R. & Maiolino, R., eds. 2004, Multiwavelength AGN Surveys

Mulchaey, J. S., Wilson, A. S., & Tsvetanov, Z. 1996, ApJ, 467, 197

Narayan, R. 2005, Ap&SS, 300, 177

Netzer, H. 2006, in Lecture Notes in Physics, Berlin Springer Verlag, Vol. 693, Physics of Active Galactic Nuclei at all Scales, ed. D. Alloin, 1–+

Norman, C. & Silk, J. 1983, ApJ, 266, 502

Omont, A., Beelen, A., Bertoldi, F., Carilli, C. L., & Cox, P. 2004, in Multiwavelength AGN Surveys, ed. R. Mújica & R. Maiolino, 109–+

Osterbrock, D. E. & Ferland, G. J. 2006, Astrophysics of gaseous nebulae and active galactic nuclei, ed. Osterbrock, D. E. & Ferland, G. J.

Osterbrock, D. E. & Pogge, R. W. 1985, ApJ, 297, 166

Pagel, B. E. J., Edmunds, M. G., Blackwell, D. E., Chun, M. S., & Smith, G. 1979, MNRAS, 189, 95

Peimbert, M. 1967, ApJ, 150, 825

Peterson, B. M. 1997, An Introduction to Active Galactic Nuclei, ed. Peterson, B. M.

Pfleiderer, J. 1963, ZAp, 58, 12

Pilyugin, L. S., Mattsson, L., Vílchez, J. M., & Cedrés, B. 2009, MNRAS, 398, 485

Pilyugin, L. S. & Thuan, T. X. 2005, ApJ, 631, 231

Pogge, R. W. 1988, ApJ, 328, 519

Popović, L. Č., Mediavilla, E. G., Bon, E., Ilić, D., & Richter, G. 2004, Astronomische Nachrichten, 325, 376

Popović, L. C., Stavrev, K. Y., Tsvetkova, K., et al. 2005, Aerospace Research in Bulgaria, 20, 126

Pounds, K. A., Done, C., & Osborne, J. P. 1995, MNRAS, 277, L5

Reynolds, C. S. 1997, MNRAS, 286, 513

Richards, G. T., Hall, P. B., Strauss, M. A., et al. 2004, in Multiwavelength AGN Surveys, ed. R. Mújica & R. Maiolino, 46–52

Robitaille, T. P., Rossa, J., Bomans, D. J., & van der Marel, R. P. 2007, A&A, 464, 541

Rodríguez-Ardila, A., Binette, L., Pastoriza, M. G., & Donzelli, C. J. 2000, in Revista Mexicana de Astronomia y Astrofisica Conference Series, Vol. 9, Revista Mexicana de Astronomia y Astrofisica Conference Series, ed. S. J. Arthur, N. S. Brickhouse, & J. Franco, 319–323

Rosati, P. & Chandra Deep Field South Team. 2001, in Bulletin of the American Astronomical Society, Vol. 33, American Astronomical Society Meeting Abstracts, 140.03–+

Rupke, D., Kewley, L., & Barnes, J. 2010a, in Astronomical Society of the Pacific Conference Series, Vol. 423, Galaxy Wars: Stellar Populations and Star Formation in Interacting Galaxies, ed. B. Smith, J. Higdon, S. Higdon, & N. Bastian, 355–+

Rupke, D. S., Veilleux, S., & Sanders, D. B. 2005, ApJ, 632, 751

Rupke, D. S. N., Kewley, L. J., & Barnes, J. E. 2010b, ApJ, 710, L156

Sánchez, S. F. 2006, Astronomische Nachrichten, 327, 850

Sánchez, S. F., Christensen, L., Becker, T., et al. 2004, Astronomische Nachrichten, 325, 112

Sánchez, S. F. & González-Serrano, J. I. 2003, A&A, 406, 435

Sandage, A. & Tammann, G. A. 1981, A revised Shapley-Ames Catalog of bright galaxies, ed. Sandage, A. & Tammann, G. A.

Schmidt, M. & Green, R. F. 1983, ApJ, 269, 352

Scodeggio, M., Franzetti, P., Garilli, B., et al. 2005, PASP, 117, 1284

Searle, L. 1971, ApJ, 168, 327

Seyfert, C. K. 1943, Contributions from the Mount Wilson Observatory / Carnegie Institution of Washington, 671, 1

Sharp, R. G. & Bland-Hawthorn, J. 2010, ApJ, 711, 818

Shaver, P. A., McGee, R. X., Newton, L. M., Danks, A. C., & Pottasch, S. R. 1983, MNRAS, 204, 53

Shields, G. A. 1976, ApJ, 204, 330

Shields, G. A. 2000, in Ionized Gaseous Nebulae

Shields, G. A. & Searle, L. 1978, ApJ, 222, 821

Shull, J. M. & McKee, C. F. 1979, ApJ, 227, 131

Skillman, E. D., Kennicutt, Jr., R. C., Shields, G. A., & Zaritsky, D. 1996, ApJ, 462, 147

Slipher, V. M. 1917, Lowell Observatory Bulletin, 3, 59

Smirnova, A. A., Moiseev, A. V., & Afanasiev, V. L. 2006, Astronomy Letters, 32, 520

Storchi-Bergmann, T., Calzetti, D., & Kinney, A. L. 1994, ApJ, 429, 572

Storchi-Bergmann, T., Wilson, A. S., & Baldwin, J. A. 1992, ApJ, 396, 45

Storey, P. J. & Zeippen, C. J. 2000, MNRAS, 312, 813

Talbot, J., J. R. & Arnett, D. W. 1974, ApJ, 190, 605

Toomre, A. & Toomre, J. 1972, ApJ, 178, 623

Ulvestad, J. S., Antonucci, R. R. J., & Goodrich, R. W. 1995, AJ, 109, 81

van den Bergh, S. 1962, AJ, 67, 486

Vanden Berk, D. E., Richards, G. T., Bauer, A., et al. 2001, AJ, 122, 549

Vanderriest, C. 1998, in Astronomical Society of the Pacific Conference Series, Vol. 152, Fiber Optics in Astronomy III, ed. S. Arribas, E. Mediavilla, & F. Watson, 123–+

Veilleux, S., Bland-Hawthorn, J., Cecil, G., Tully, R. B., & Miller, S. T. 1999, ApJ, 520, 111

Veilleux, S. & Osterbrock, D. E. 1987, ApJS, 63, 295

Veilleux, S., Shopbell, P. L., Rupke, D. S., Bland-Hawthorn, J., & Cecil, G. 2003, AJ, 126, 2185

Veron-Cetty, M. P. 1984, A&AS, 58, 665

Vila-Costas, M. B. & Edmunds, M. G. 1992, MNRAS, 259, 121

Vilchez, J. M. & Esteban, C. 1996, MNRAS, 280, 720

Villar-Martín, M., Humphrey, A., Martínez-Sansigre, A., et al. 2008, MNRAS, 390, 218

Vorontsov-Velyaminov, B. A. 1959, in Atlas and catalog of interacting galaxies (1959), 0–+

Ward, M. J. & Wilson, A. S. 1978, A&A, 70, L79

Westmoquette, M. S., Exter, K. M., Christensen, L., et al. 2009a, ArXiv e-prints

Westmoquette, M. S., Smith, L. J., Gallagher, III, J. S., et al. 2009b, ApJ, 696, 192

Wilkes, B. 1999, in Astronomical Society of the Pacific Conference Series, Vol. 162, Quasars and Cosmology, ed. G. Ferland & J. Baldwin, 15–+

York, D. G., Adelman, J., Anderson, Jr., J. E., et al. 2000, AJ, 120, 1579

Yoshida, M., Ohyama, Y., Iye, M., et al. 2004, AJ, 127, 3653

Zanichelli, A., Garilli, B., Scodeggio, M., et al. 2005, PASP, 117, 1271

Zaritsky, D., Kennicutt, Jr., R. C., & Huchra, J. P. 1994, ApJ, 420, 87

Zhang, K., Wang, T., Dong, X., & Lu, H. 2008, ApJ, 685, L109

Zheng, W., Kriss, G. A., Telfer, R. C., Grimes, J. P., & Davidsen, A. F. 1997, ApJ, 475, 469

Danksagung/Acknowledgement

I know that I owe a lot to a lot of people and even though I do hope that I have been able to communicate my deepest thanks and appreciation throughout the years, it is my wish to address a few people in particular:

Meinen Eltern, die mich Zielstrebigkeit und Durchhaltevermöegen gelehrt haben, und mir die Freiheit gegeben haben zu tun, was meinen Leidenschaften entspricht, gilt mein größter Respekt und Dank. Außer vielleicht einer gezuckten Augenbraue habe ich Nichts an Ablehnung oder Zweifel erlebt, als ich meine ungewöhnliche Entscheidung, Astronomie und Malerei studieren zu wollen (nach Abschluss einer Tourismusschule), vorgetragen habe.

Ich kann mich nicht erinnern, zu irgendeinem Zeitpunkt keine Untstützung von meiner Familie (und damit meine ich auch die erweiterte Familie die über Nachnamen hinausgeht) und meinen wunderbaren Freunden der Stunde 0 bekommen zu haben. Mir ist bewusst, wie ungewöhnlich das ist und wieviel Glück ich habe, diese Art von Vertrauen entgegen gebracht zu bekommen.

Am Anfang des Studiums war ich mehr als verloren und kann mich noch allzu gut erinnern, wie verwirrend und frustrierend all diese griechischen Buchstaben auf der Tafel waren. Und ich weiß ohne Zweifel, dass ich ohne Hilfe meiner großartigen Studienkollegen, die zu engen Freunden geworden sind, gescheitert wäre. Ich hoffe ich kann euch zurück geben, was ihr mir gebt.

Auch als Kunstschaffende habe ich für mein Experiment, Kunst mit Wissenschaft zu verbinden viel Zuspruch, Unterstützung und Freunde gefunden.

Professionally, I owe thanks to my supervisor Werner Zeilinger for his support, especially concerning my constant wish to go abroad and experience new things; Joss Hawthorn who knows how to get across passion when it comes to astronomy and the opportunity that he gave me by working at Sydney; Sarah Brough who introduced me to the world of VIPGI and is a great person to know as well as Rob Sharp - I wish there was a guide to your code! Not only did I learn *a lot* while working at the AAO and USyd, I also made friends with amazing people. With all the talent that's accumulated there, I am completely speechless and humble.

6 Curriculum Vitae

Education

Master of Science in Astronomy, University of Vienna, 2011
Title of Thesis: Integralfield Spectroscopy of Galaxies: A Study of Interacting Seyferts

Master of Arts in Fine Arts, Painting, University of Applied Arts, 2010
Title of Thesis: Measuring Mistakes

Bachelor of Science in Astronomy, University of Vienna, 2007
Title of Thesis: Morphology and Dynamics of Interacting Galaxies; Black Holes in Galaxy Mergers and the Evolution of Quasars

Higher Educational School for Tourism and Economics, 2003

Grammar School: Kollegium Kalksburg, Vienna, 1998

Experience

ESO Chile short-term studentship *2011*
measuring SFR in a galaxy group at z$\sim$1with NIR NB photometry. Paper in preperation.

Presentation of first results of my Master thesis at the AG conference *2010*
"Integralfield Spectroscopy of interacting galaxies: Tracing Accretion Signatures with [OIII]/Hβ ratios"

Research scholarship *2009*
to work with Prof. J. Bland-Hawthorn at the University of Sydney, observational time at the AAT

Conferences & workshops

Zooming In, Cosmos at High Resolution, Bonn *September 2010*

ÖGAA Meeting, Graz *April 2010*

Venus Landing Site Entry Probe Workshop *2006, 2007*

Awards and Scholarships

ESO/DGDF funding for short term studentship at ESO Chile *2011*
For a 3 months studentship at ESO Santiago to work with Valentin Ivanov.

Prize for best Diploma *2010*
Awarded from the City of Vienna

Johanna Dohnal sponsorship award *2010*
For my efforts in connecting science with arts.

Research scholarship *2009*
For a 3 months research with Prof. Jonathan Bland-Hawthorn from the University of Sydney and the AAO, awarded from the University of Vienna

Joint Study Scholarship *2008*
For an Exchange Semester at the University of Sydney